REPORT DOCUMENTATION PAGE

Public reporting burden for this collection of information is estimated to average 1 hour per response, including the time for reviewing instructions, searching existing data sources, gathering and maintaining the data needed, and completing and reviewing the collection of information. Send comments regarding this burden estimate or any other aspect of this collection of information, including suggestions for reducing this burden, to Washington Headquarters Services, Directorate for Information Operations and Reports, 1215 Jefferson Davis Highway, Suite 1204, Arlington, VA 22202-4302, and to the Office of Management and Budget, Paperwork Reduction Project (0704-0188), Washington, DC 20503.

1. AGENCY USE ONLY *(Leave blank)*	2. REPORT DATE 9 Jan 97	3. REPORT TYPE AND DATES COVERED

4. TITLE AND SUBTITLE
The Role of Radiative Processess In The Tropical Intraseasonal Oscillation

5. FUNDING NUMBERS

6. AUTHOR(S)
Michael William Johnson

7. PERFORMING ORGANIZATION NAME(S) AND ADDRESS(ES)
University of Utah

8. PERFORMING ORGANIZATION REPORT NUMBER

96-35D

9. SPONSORING/MONITORING AGENCY NAME(S) AND ADDRESS(ES)
DEPARTMENT OF THE AIR FORCE
AFIT/CIA
2950 P STREET
WPAFB OH 45433-7765

10. SPONSORING/MONITORING AGENCY REPORT NUMBER

11. SUPPLEMENTARY NOTES

12a. DISTRIBUTION AVAILABILITY STATEMENT
Unlimited

12b. DISTRIBUTION CODE

13. ABSTRACT *(Maximum 200 words)*

19970116 012

DTIC QUALITY INSPECTED 2

14. SUBJECT TERMS

15. NUMBER OF PAGES
118

16. PRICE CODE

17. SECURITY CLASSIFICATION OF REPORT	18. SECURITY CLASSIFICATION OF THIS PAGE	19. SECURITY CLASSIFICATION OF ABSTRACT	20. LIMITATION OF ABSTRACT

THE ROLE OF RADIATIVE PROCESSES IN THE TROPICAL

INTRASEASONAL OSCILLATION

by

Michael William Johnson

A dissertation submitted to the faculty of
The University of Utah
in partial fulfillment of the requirements for the degree of

Doctor of Philosophy

Department of Meteorology

The University of Utah

December 1996

ABSTRACT

The tropical 30-60 day oscillation (intraseasonal oscillation - IO) is a topic of contemporary interest and a unified theory as to how it is created, why it behaves so erratically, and what is the mode of propagation does not exist. Theories and observational studies have emphasized the role of tropical convection in the Western Pacific Ocean with less attention paid to the role of radiative cooling in the area of the downward branch of the Walker circulation. This research focuses on that area (the tropical Eastern Pacific Ocean) where it is hypothesized that radiative cooling interacts with IO-circulations.

Analysis is made in terms of calculated radiative heating fields and Kelvin winds (used as a proxy for IO-circulations). Radiative heating is calculated for seventeen pressure levels (1000-100 mb) for a 6 ½ year period (1985 to mid-1991) at a 5-day frequency based on NCEP/NCAR gridded data and ISCCP/C1 clouds. Concurrently, normal mode projections of NCEP/NCAR gridded data are made to isolate the Kelvin mode response in the wind and height field. These calculated radiative heating and Kelvin winds are then spectrally filtered to isolate frequencies associated with the IO. Finally, a diagnostic analysis is made based on composited comparisons, lagged correlations, and a selected case study between filtered-Kelvin-winds and filtered-radiative-cooling.

The analysis reveal three primary conclusions. First, there is a significant relationship between IO-circulations and IO-scale radiative heating in the Eastern Pacific Ocean. Second, this relationship exhibits both a remote scale spanning the entire Pacific and a local scale unique to the Eastern Pacific. Third, the radiative heating signal precedes the upstream response in the Kelvin wind by 5 to 10 days.

CONTENTS

LIST OF FIGURES

ix

ACKNOWLEDGMENTS

I would like to express my sincere appreciation to Prof. Julia Nogués-Paegle, my committee advisor and respected instructor, for her guidance, tolerance, and support throughout this endeavor. I could not have finished without her help and encouragement. I am also grateful also to all the members of my supervisory committee, Dr. Kuo-Nan Liou, Dr. Jan Paegle, Dr. Szu-Cheng Ou, and Dr. James E. Hoke for their many helpful suggestions and comments throughout this research. I would especially like to thank Dr. Qiang Fu and Dr. Szu-Cheng Ou for their invaluable help and suggestions regarding radiative calculations. In addition, I would like to recognize the administrative support of Melia and Leslie, as well as computer bug fixes supplied by our computer guru, Lloyd. Finally, to my wife Becky, and two boys Andy and Ben: thank you for being patient with me these last few years. All of my motivation comes from you guys.

I would like to acknowledge the extensive use of the Grid Analysis and Display System (GrADS) to produce many of the figures in this manuscript and to analyze/manipulate the extensive datasets and calculations that led to those figures.

CHAPTER 1

INTRODUCTION

It was over two decades ago that Madden and Julian (1971) first hypothesized the origin of the intraseasonal oscillation (IO). Yet the nature of this oscillation remains a topic of contemporary interest (Nogués-Paegle et al. 1989; Ferranti et al. 1990; and Lau and Chang 1992) and a unified theory as to how it is created, why it behaves so erratically, and what is the mode of propagation does not exist. This is mostly due to the difficulty on sorting out the relative importance of various physical processes which may be invoked for its excitation and maintenance. Additionally, the processes involved in observed IO-tropical-extratropical teleconnection patterns are not fully understood (see for example Weickmann et al. 1985, and Berbery and Nogués-Paegle 1993). Intraseasonal oscillation signatures on outgoing longwave radiation (OLR) data show typical events with periods between 30-60 days having a maximum amplitude over Indonesia and eastward progression weakening over the cold waters of the Eastern Pacific Ocean. It is also common to observe eastward propagation of divergence fields in apparent association with the OLR convective burst. This strong convective signal has prompted development of theories which focus on excitation of the oscillation by tropical diabatic heating, thus emphasizing the convective regions of the Western Pacific Ocean. It is within this region that a broad longitudinal circulation sets up which is referred to as

the Walker circulation; see Fig. 1.1. The relationship of the IO with respect to the part of the Walker circulation outside of the convective region is not clear. In particular, the possible role that radiative cooling (within the sinking branch) has with the IO does not appear to have been previously explored.

Recent availability of improved climatological datasets makes it possible to investigate this aspect of the IO. Specifically, atmospheric data from the National Centers for Environmental Prediction [NCEP, formerly known as the National Meteorological Center (NMC)]/National Center for Atmospheric Research (NCAR) Reanalysis project are used. In addition, cloud properties from the International Satellite Cloud Climatology Project (ISCCP) are used as model inputs to calculate radiative and dynamic properties of the IO. Radiative cooling is calculated using an efficient and comprehensive radiative model of Fu and Liou (1992). Dynamic signatures contained within the wind and height reanalysis data are decomposed using normal mode analysis of a simple linearized equations model about a basic state at rest. Finally, in order to determine the role of radiative cooling in the Eastern Pacific Ocean, a correlative statistical analysis is performed. A statistically significant period of study is chosen based on concurrently available data. First, radiative calculations are made for a continuous period between January 1985 through June 1991. Next, normal mode calculations are made for the continuous period between January 1985 through December 1993.

Organization of this dissertation follows the radiative and dynamic aspects of the problem. Radiative analysis and results are described in Chapter 3, and normal mode analyses are presented in Chapter 4. The intent is for both of these chapters to be as self-

Walker Circulation
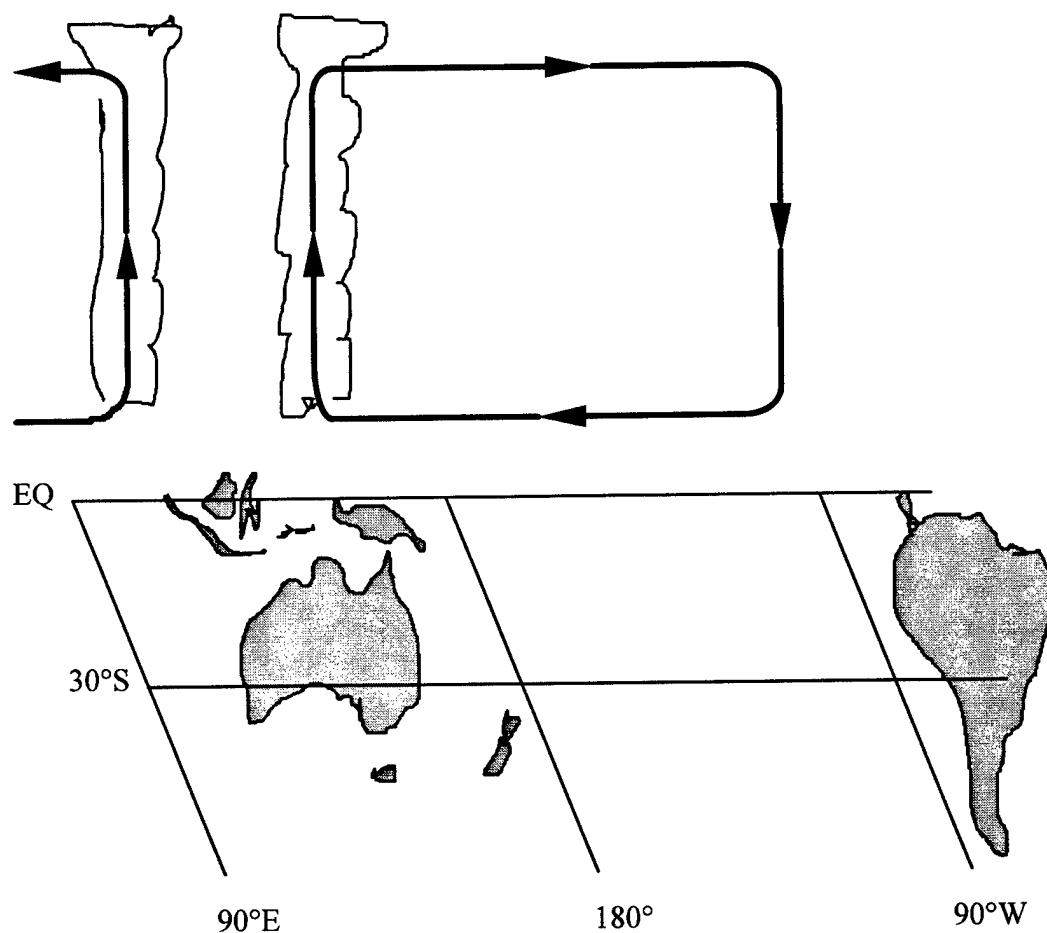
FIG. 1.1 Walker circulation. This circulation is characterized by upward motion in the convective regions of the Western Pacific Ocean, upper-level westerly flow over the Central Pacific Ocean, a sinking branch over the Eastern Pacific Ocean, and return flow at lower levels.

contained as possible. Chapter 2 provides the background material needed for cohesiveness and as motivation for the methods used, and Chapter 5 presents comparisons between results of Chapters 3 and 4. Finally, Chapter 6 contains a general discussion of findings as well as summary and conclusions.

CHAPTER 2

BACKGROUND

2.1 Intraseasonal Oscillation

The intraseasonal oscillation is a large-scale low-frequency tropical disturbance propagating eastward with a period on the order of 30 to 60 days. It was first reported by Madden and Julian (1971), and is also known as the Madden-Julian oscillation, the 30 to 60 day oscillation, or the 45 to 60 day oscillation. This section reviews a number of illuminating references regarding observations, theory, and unresolved questions concerning the intraseasonal oscillation.

Observations of the IO are made primarily from either OLR anomalies (intraseasonally filtered signals) or from upper-level divergent wind anomalies. The former method looks at convective source areas only while the latter can also detect the propagating IO in regions of little or no convection. Less significant signatures can also be detected in anomalies of low-level convergent wind and surface pressure. Propagation characteristics for 1987 IO events depicted by OLR observations are shown in Fig. 2.1. Note the high degree of variability from one event to another with the strongest ones propagating completely around the globe. In fact, the event that starts in January 1987 is shown to propagate twice around the globe over a period of 120 days. Also notice that negative anomalous OLR (as a proxy for convection) typically stalls out over the cold

FIG. 2. 1 Hovmöller diagram of average anomalous OLR for 1987. Anomalies are defined as the remaining signal after filtering out frequency variabilities smaller than 20 days or greater than 90 days. They are then averaged between 10°S and 10°N and those less than or equal to -5W m^{-2} are plotted with a contour interval of 5 W m^{-2}. Solid lines indicate the subjectively estimated position of the IO for a given date and longitude. Data were obtained from the Climate Prediction Center, NCEP/NOAA (courtesy of K.C. Mo) from NESDIS averages of individual satellite scans. Daily values represent averages from the twice-a-day original data interpolated to 2.5° grids described by Liebmann and Smith (1996).
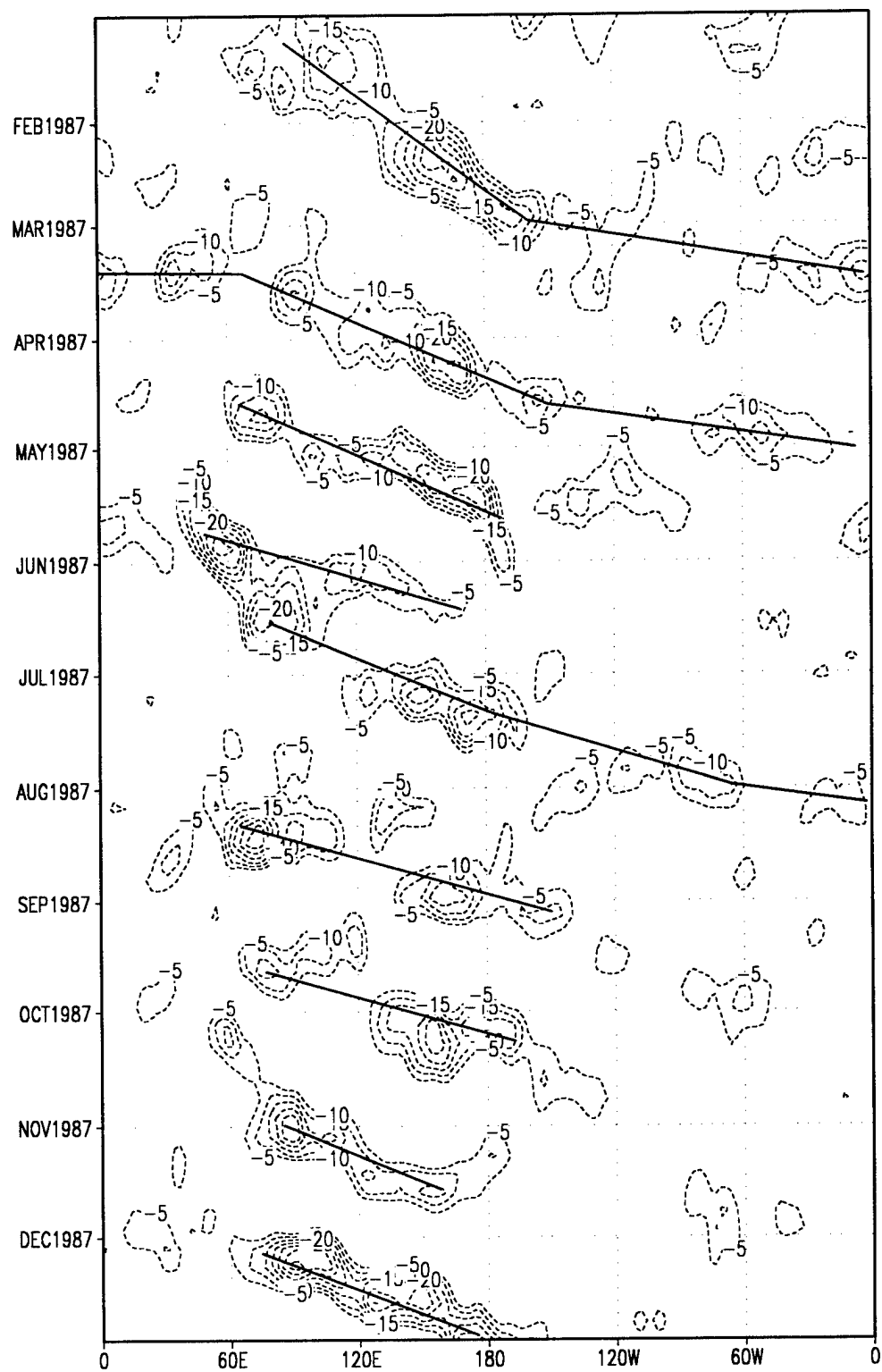
waters of the Central Pacific Ocean (equator, 180°W) and stronger cases appear to accelerate in that region as the convection weakens. A comprehensive observational description of the IO was given by Rui and Wang (1990) using filtered 5-day mean anomalies of long-term records of OLR and divergent winds. They characterized the longitudinal progression of moderate- and strong-strength composite cases within tropical latitudes (like those shown in Fig. 2.1) as follows. For the moderate-strength cases, the convective "source" region is first identifiable over Africa (30°E) and then moves slowly into the Indian Ocean and intensifies. The maximum negative anomalies occur during the transition over the Eastern Indian Ocean (90°E). Next, this region expands in area and weakens as it moves over the Indonesian Subcontinent and into the Western Pacific Ocean (150°E). From there, it weakens rapidly and is no longer distinguishable at the date line (180°W). Strong cases differ from moderate cases in two ways. First, for strong cases, the convective source region reamplifies over the Western Pacific Ocean after crossing the Indonesian Subcontinent and then weakens less rapidly as it progresses to the date line. Second, convective anomalies that reach the Central Pacific Ocean frequently emanate away from the tropics and towards North America and the South Eastern Pacific Ocean (this is not evident in the latitudinally averaged fields of Fig. 2.1). Figure 2.1 shows propagation speeds during 1987 ranging from 2° to 11° longitude per day.

Rui and Wang (1990) also found that the mean propagation speed varies somewhat from one event to another with an average speed of 4° longitude per day. In addition, for many of the strong cases there is a pronounced longitudinal speed variation. Normally, the disturbance at first proceeds slowly with phase speeds of less than 4° per day but then

increases to over 6° per day over the Central Pacific Ocean.

The origin and maintenance of the intraseasonal oscillation have remained somewhat of a mystery since its discovery. Most theories focus on oscillatory response to forcing within diabatic heating regions between 90°E-120°E; there are two prevalent scenarios given to the forcing. One hypothesis is that there is a fixed oscillating heat source (possibly related to the Asian monsoons) which induces standing tropical modes. However, this does not explain the apparent eastward progression of the heating source. For that reason, a second hypothesis is that additional forcing is provided through an internal heating mechanism such as conditional instability of the second kind (CISK).

Gill (1980) used a fixed heating source in a simple steady-state linearized shallow water model to simulate standing Kelvin- and Rossby-wave responses. He pointed out that an east-west Walker circulation results from this fixed diabatic heating source due to Kelvin wave propagation. Extensions of Gill's fixed forcing model to include a more general basic state and oscillatory forcing were made, for example, by Yamagata and Hayashi (1984) and Anderson and Stevens (1987) resulting in improved agreement with IO observations. In a further generalization of Gill's model, Lau and Peng (1987) allowed for a traveling heat source as well as selective amplification of Kelvin waves through a mobile-CISK mechanism. Their results predicted not only an eastward propagation of the source region but also increased phase speeds in the cold waters of the Eastern Pacific where convective source regions frequently disappear.

Despite the steady improvement of theoretical modeling of the IO, disturbing discrepancies between theoretical results and observations persist. The most serious of

these, and prevalent to all of the theoretical models, is a predicted propagation speed commonly twice as fast as that observed. A free Kelvin wave, believed to be the principal mode of IO-propagation, would propagate about 15° longitude per day, much faster than observed IO-speeds. Chang (1977) showed that a reduction of the Kelvin wave speed may be realized by introducing dissipation. This analysis does not indicate how the wave structure is maintained against dissipation. In addition, much of the structure and variability seen in the observations cannot yet be explained. This suggests that the IO is more complex than the simple explanations so far provided, and that some of the physical mechanisms responsible for its origin and maintenance are not yet fully understood.

In particular, the role, if any, that radiative cooling in the Eastern Pacific Ocean plays in the IO has not been systematically explored. Specifically, we hypothesize that radiative cooling within the sinking cell of the Walker circulation in the Eastern Pacific Ocean interacts with the IO and possibly affects its behavior in that region. Although the energy supplied by radiational cooling is a small portion of the total heating energetics in the Western Pacific Ocean it is the dominant source over the vast nonconvective areas of the Eastern Pacific Ocean. Figure 2.2 shows January through March average heating contributions along an equatorial cross section from 1000 mb to 150 mb (obtained from the NCEP/NCAR Reanalysis database, see Kalnay et al. 1996). Although these heating rates are model-derived quantities, they should represent a useful qualitative overview of the winter-time tropical heating structure. Figure 2.2a shows the total heating cross section in units of K day^{-1}. Total heating here refers to the summation of condensational heating, both deep-convective- and large-scale-heating (the latter is negligible in the

Jan—Mar

a. Equatorial Total Heating (Cooling)

b. Equatorial Radiative Cooling

c. % Radiative to Total
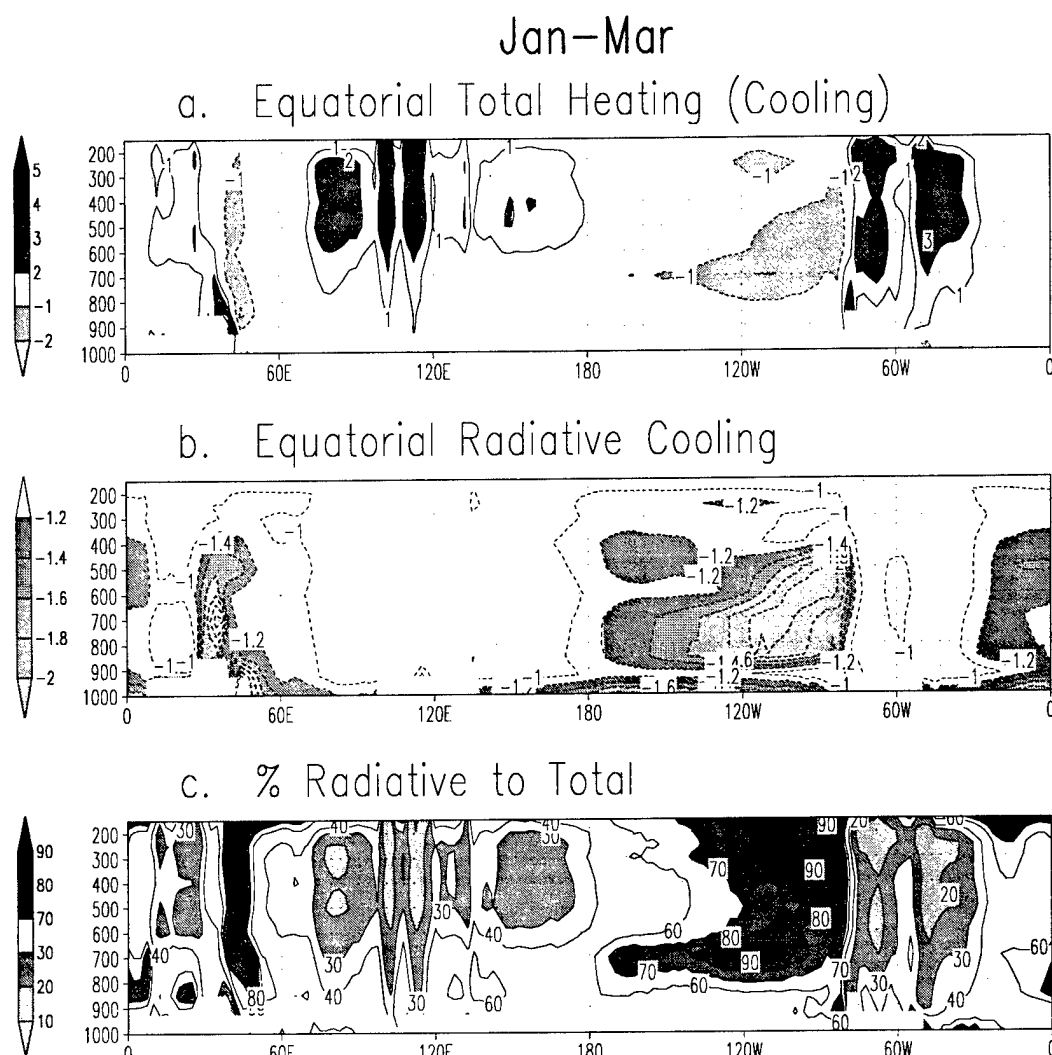
FIG. 2. 2 Equatorial heating cross section averaged for January through March taken from derived monthly heating climatologies from 1982 through 1994 reported by the NCEP/NCAR Reanalysis Project (Kalnay et al. 1996). Panels (a-b) show total heating and radiative cooling respectively in K day^{-1} along an equatorial slice from 0°-360° in longitude between 1000 mb - 150 mb. Panel (c) is the percentage of radiative cooling to total heating (or cooling).

tropics) shallow convective heating; vertical diffusive heating; shortwave radiational heating; and longwave radiational heating. Convective heating dominates Indonesia and the Western Pacific Ocean and radiative cooling dominates the Eastern Pacific Ocean. Also, the maximum convective heating in the Western Pacific Ocean occurs at higher vertical levels than does the maximum radiative cooling in the Eastern Pacific Ocean.

Figure 2.2b shows regions of significant radiative cooling again in units of $K\ day^{-1}$. Here, radiative cooling is defined as the summation of shortwave radiational heating and longwave radiational cooling (which is dominated by the longwave component producing a cumulative cooling affect). Figure 2.2c shows the percentage of radiative heating to total heating. This figure not only summarizes the relative importance of radiative cooling but also infers a Walker circulation; with rising motion in the convective regions of the Western Pacific Ocean and sinking motion in the radiatively cooled regions of the Eastern Pacific Ocean. This influence is based on scale analysis which shows an approximate balance in large tropical scales between adiabatic warming/cooling due to vertical motions and sinks/sources of heating. Finally, since radiative cooling is the dominant energy sink in the Eastern Pacific Ocean, it would seem reasonable to expect that it might impact slow moving dynamical systems (like the IO) as they transit that region. It is the objective of this research to quantify this relationship, if it exists. Also, by mass continuity, sinking motions in the Eastern Pacific Ocean require rising motions somewhere else. If such compensatory rising motions occur within the conditionally unstable tropical regions (such as the Western Pacific Ocean) then convection and latent heat release would result. It is not within the scope of the present dissertation to explore

fully such possible linkages between the Eastern and Western Pacific Ocean, since part of the signal is likely to be filtered out in the process of focusing on scales longer than 20 days.

2.2 Databases

The main data used in this dissertation are the NCEP/NCAR Reanalysis and the ISCCP datasets as well as an important subsidiary dataset, the Earth Radiation Budget Experiment. Discussion in this section focuses on aspects of these data sources relevant to this dissertation (e.g., period of study, tropical location, and parameters used).

2.2.1 NCEP/NCAR Reanalysis

The NCEP/NCAR Reanalysis project is a frozen state-of-the-art postanalysis/forecast system that will eventually assimilate observational data from 1957 through the present. In addition, the same fixed system will be used to extend this climatological archive into the future. Observations are gathered at NCAR and after a preliminary quality check are sent to NCEP for processing. Output fields from this NCEP processing are then sent on to NCAR (and other archive centers) for archiving and distribution. As of February 1996, the reanalysis archive available at NCAR included the period from 1982 through 1995. The project was inspired by the need to eliminate apparent "climate changes" introduced by the constant changes made to the NCEP operational Global Data Assimilation System. Sources of observational data are the global upper-air datasets (rawinsonde, pibal, aircraft) archived from the Global Telecommunications System circuit; the Comprehensive Ocean-Atmosphere Data Set (COADS) surface marine data;

supplemental aircraft and balloon data; surface land synoptic data; radiances from TOVS [Television and Infrared Operational Satellite (TIROS) Operational Vertical Sounder]; and satellite cloud-drift winds. Furthermore, these data have been supplemented by various upper-air datasets that were not available during NCEP operational runs. These additional data include portions of national archives from the United States, Russia, China, South Africa, Australia, Canada, Argentina, and Brazil. Climatological data are used in boundary conditions when analyzed fields are not available (e.g., Advanced Very High Resolution Radiometer-derived sea surface temperature climatology and surface albedo climatology from Matthews 1985).

The main data assimilation components of the NCEP/NCAR Reanalysis system are the data analysis, the forecast model, and observational quality control. First, a spectral statistical interpolation (SSI) is used (Parrish and Derber 1992; Derber et al. 1991) to assimilate data. An SSI pilot operational demonstration at NCEP showed major analysis and forecast improvements, especially in the tropics. One of the advantages of this three-dimensional variational analysis scheme is that the balance imposed on the analysis is valid throughout the globe, which makes the use of nonlinear normal mode initialization unnecessary. In addition, normal mode initializtion would have removed a part of the IO-circulation signal for which we are trying to isolate, thus making this dataset particularly well-suited for this research. Second, the assimilation module uses a T62 spectral model (~210 km resolution) with 28 vertical levels. Model sigma levels as well as standard output levels are shown in Fig. 2.3. By design, there is a concentration of model levels in the boundary layer and the stratosphere which assures reasonable boundary-layer resolution and minimal migration of upper-boundary-condition-effects down to
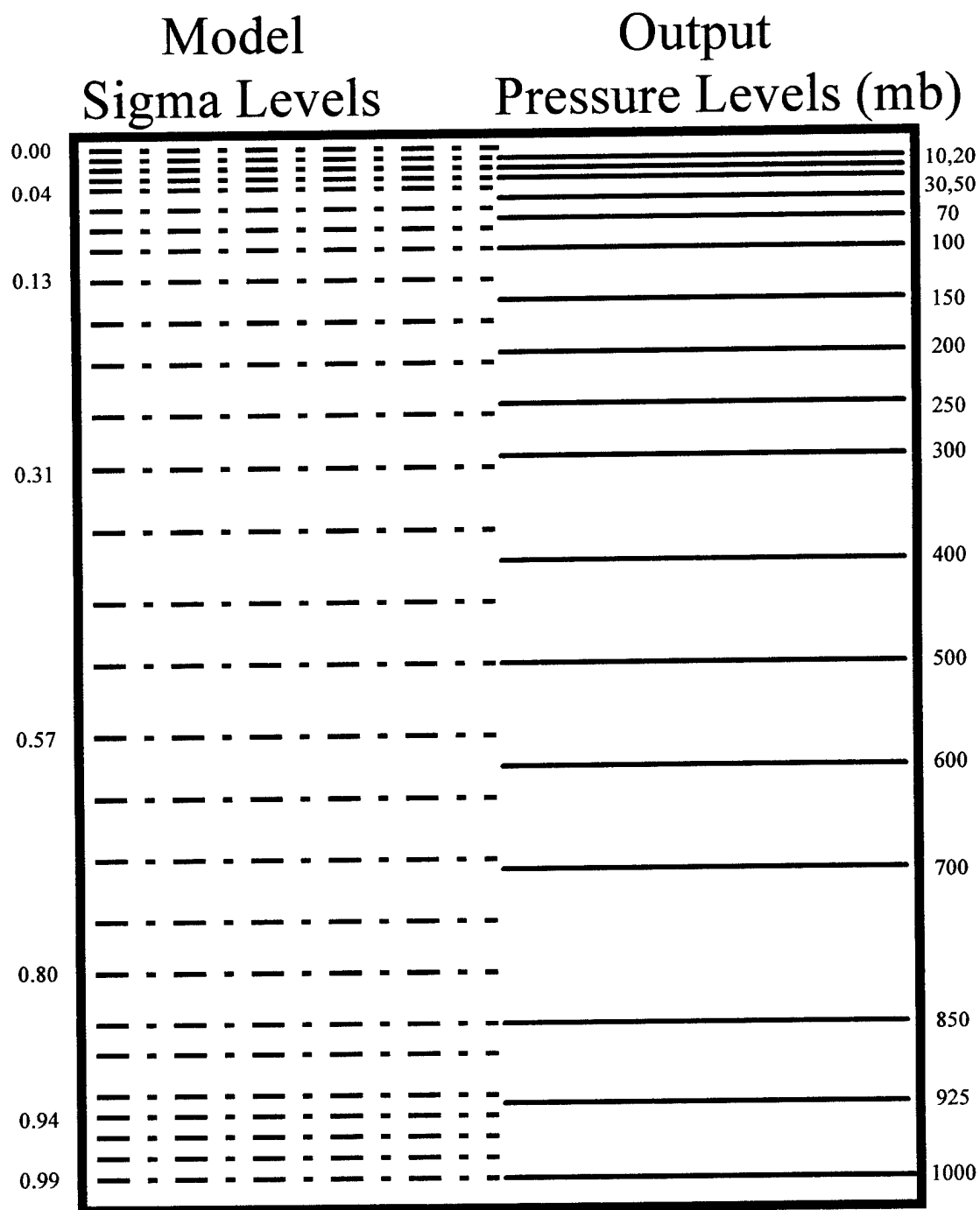
FIG. 2. 3 NCEP/NCAR Reanalysis model and output levels. Dashed lines indicate the 28 sigma levels of the analysis model, and solid lines indicate the 17 pressure levels of the output fields.

tropospheric levels. Additionally, the model uses a comprehensive suite of physical process parameterizations, including convection, large-scale precipitation, shallow convection, gravity wave drag, cloud and diurnal cycle interactional radiation, boundary layer physics, interactive surface hydrology, and vertical and horizontal diffusion processes. Third, quality control of input rawinsonde height and temperature fields is made via the Complex Quality Control method of Gandin (1988). In general, this scheme checks the hydrostatic balance of the radiosonde observations as well as their horizontal, vertical, and temporal consistency with the 6-h forecast field. All other data are quality controlled using the Optimal Interpolation Quality Control method of Woollen (1991, 1994). This method uses a statistical representativeness error model to identify and withhold data containing gross errors in a statistical sense.

There are a variety of output fields available from the NCEP/NCAR Reanalysis project. The two used for this study are the analysis-pressure and analysis-flux fields; both are available at 00, 06, 12, and 18 UTC. The pressure field is given on a 2.5° latitude-longitude grid (output vertical pressure levels are shown in Fig. 2.3) while the flux field is given on a 192 X 94 Gaussian grid. Parameters from the pressure field used in this research include atmospheric temperature and winds at 17 pressure levels as well as specific humidity at 8 levels (1000-300 mb). Surface temperature is the only parameter obtained from the flux field.

2.2.2 ISCCP

The International Satellite Cloud Climatology Project is an experimental cloud climatology derived from active geostationary- and polar-orbiting meteorological

satellites. It is part of a number of other research projects established under the World Climate Research Program (WCRP) to study cloud-radiation interactions on climate. The first stage of the ISCCP project is complete and includes 3-h and monthly cloud climatologies (C1 and C2 datasets respectively). These data are available through the Langley Distributed Active Archive Center (DAAC) for the period ranging from January 1983 through June 1991. In addition, second stage data (D1 and D2, which are an evolution of C1 and C2) became available in February 1996 through Langley/DAAC for the period extending beyond June 1991. This section focuses on the first stage 3-h ISCCP/C1 dataset.

Processing of the various satellite infrared (IR) and visible (VIS) radiances[1] begins by placing them into a common format and normalizing to a standard reference calibration (Rossow and Schiffer 1991). These data are concurrently reduced by selective sampling both spatially and temporally; producing the B3 radiance dataset with a nominal spatial resolution of 30 km and temporal resolution of 3 h.

The cloud analysis procedure of B3 data includes cloud detection, radiative analysis, and statistics. First, cloud detection is accomplished by collecting monthly variance statistics on VIS and IR radiances. Based on these statistics, estimates are made of VIS and IR clear-sky background radiances. The B3 data are then compared to estimated clear-sky backgrounds to determine the degree of cloudiness at each location and time.

---

[1] Geostationary satellites (METEOSAT, INSAT, GMS, GOES-WEST, and GOES-EAST) provide global coverage and are supplemented with data from at least one NOAA polar-orbiting satellite. Note that significant operational events that occurred between January 1985 and June 1991 include the addition of INSAT data starting in 1988 (full disc geostationary coverage centered at 74° E) as well as the failure of GOES WEST in 1989 (causing variable loss of coverage in the Central Pacific Ocean).

Second, radiative analysis compares radiative transfer calculations to B3 radiances in order to derive cloud top temperature (VIS and IR) and cloud optical depth (VIS only). Cloud top pressures (heights) are estimated by comparing cloud top temperatures to TOVS atmospheric profile data. Radiative calculations are made at 0.6 µm for VIS and 11 µm for IR corresponding to satellite radiance channels. One of the key assumptions made in the radiative calculations is that clouds can be represented as a single, isothermal layer, uniformly covering the image pixel area and composed of evenly distributed 10 µm water droplets. Third, in order to further reduce the cloud climatology to a manageable volume; cloud-coverage, optical-depth, and cloud-top-pressure statistics are derived for a 2.5° latitude-longitude grid at 3 h intervals. This level of processing forms the basis of the 3-h ISCCP/C1 dataset. Vertical resolution as well as the cloud classification scheme for VIS radiance statistics are shown in Fig. 2.4.

2.2.3 ERBE

The Earth Radiation Budget Experiment was a multisatellite project designed under WCRP to measure the earth's radiation budget. Global data are available from November 1984 through February 1990. However, the amount of global coverage varies for that period depending on how many instruments were available at a given time.[2] The wideband scanner data (ERBE/S9) contain regional coverage of daily average top-of-the-atmosphere outgoing longwave radiation (OLR). This longwave radiance is detected between frequencies of 5 to 50µm.

---

[2] ERBE scanner instruments operated on the NASA ERBS satellite from October 1984 through February 1990; on NOAA-9 from December 1984 through January 1987; and on NOAA-10 from September 1986 through May 1989.
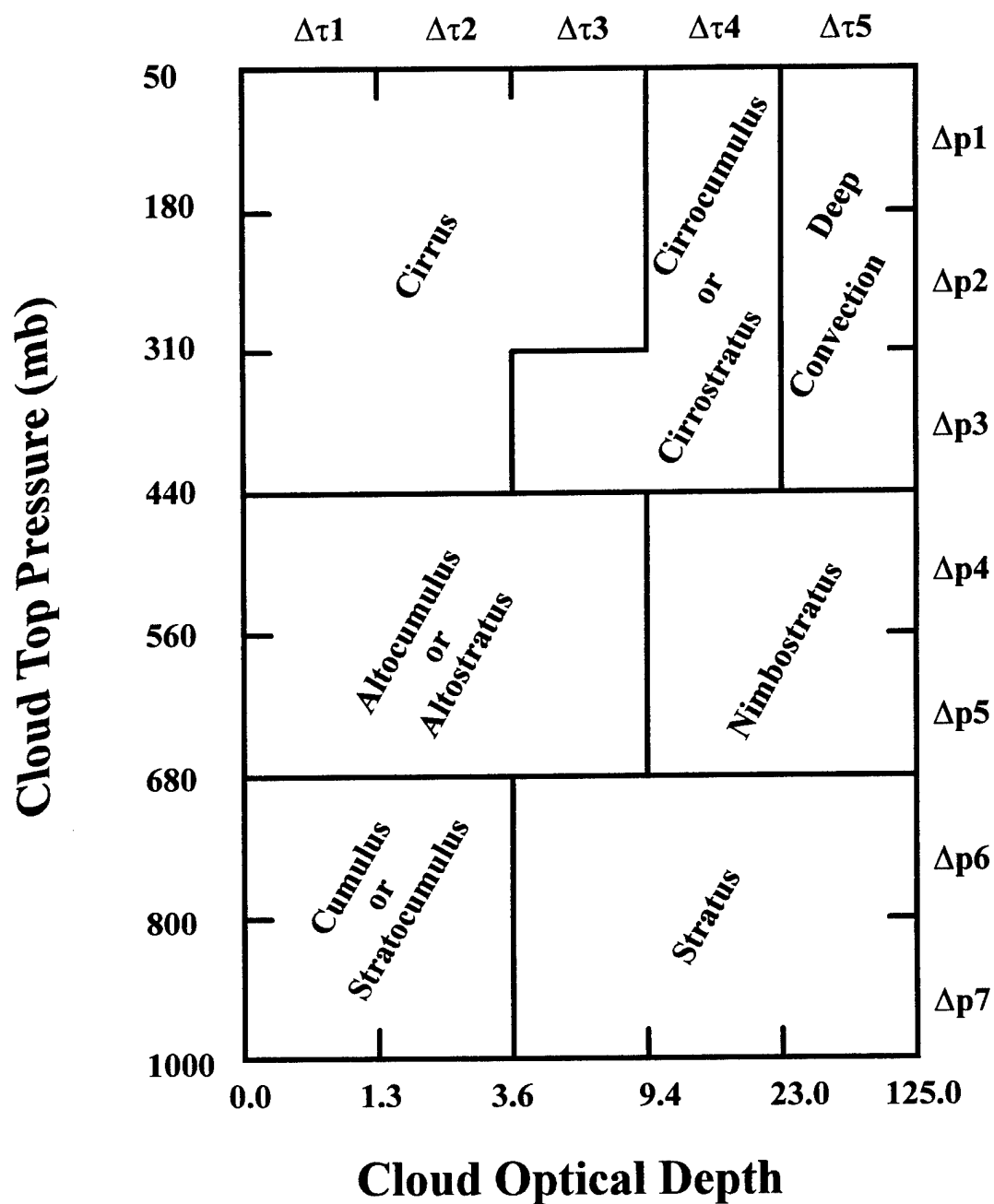
FIG. 2. 4. ISCCP cloud classification using satellite-derived values of cloud optical depth and cloud top pressures. Shown are seven pressure categories ($\Delta p1$-$\Delta p7$) and five optical depth categories ($\Delta \tau 1$-$\Delta \tau 5$) for a total of 35 cloud classification combinations of optical depth and cloud top pressures. Adapted from Rossow and Schiffer, 1991.

2.3 Relationship Between Tropical Dynamics and Radiation

The response of tropical circulations to diabatic heating depends on the vertical stratification of the atmosphere and the relative location of diabatic heating with respect to this stratification. This point is illustrated by examining the linear response to diabatic heating as shown by Simmons (1982). For the steady-state linearized case of no zonal-mean flow and no dissipation; the vorticity, thermodynamic and continuity equations can be written as

$$2(\Omega / a)v'\cos\phi = -2\Omega\sin\phi D, \tag{2.1}$$

$$-S\omega = Q, \tag{2.2}$$

$$D + \frac{\partial\omega}{\partial p} = 0, \tag{2.3}$$

where D is the perturbation divergence given by

$$D = \frac{1}{a\cos\phi}\frac{\partial u'}{\partial\lambda} + \frac{1}{a\cos\phi}\frac{\partial}{\partial\phi}(v'\cos\phi) \tag{2.4}$$

and S is the static stability given by

$$S = \frac{\kappa\overline{T}}{p} - \frac{d\overline{T}}{dp}. \tag{2.5}$$

Here u' and v' are the eastward and northward perturbation velocities; p is pressure; Ω is the earth rotational velocity, a is the mean earth radius; ϕ is latitude, $\overline{T}$ is the global-mean temperature at pressure p; $\kappa = R/C_p$ where R is the specific gas constant and C_p is the

specific heat at constant pressure; Q is the heating rate; and ω=dp/dt.

By eliminating D from Eq. (2.1) using Eqs. (2.2) and (2.3) Simmons obtained

$$v'\cos\phi = -a\sin\phi\frac{\partial}{\partial p}\left(\frac{Q}{S}\right), \qquad (2.6)$$

and from Eq. (2.4)

$$\frac{\partial u'}{\partial\lambda} = 2a\cos\phi\frac{\partial}{\partial p}\left(\frac{Q}{S}\right) + a\sin\phi\frac{\partial^2}{\partial\phi\partial p}\left(\frac{Q}{S}\right). \qquad (2.7)$$

Near the equator, the last term in Eq. (2.7) vanishes leaving the relationship

$$\frac{\partial u'}{\partial\lambda} \cong 2a\cos\phi\frac{\partial}{\partial p}\left(\frac{Q}{S}\right). \qquad (2.8)$$

It is apparent then that the linkage between the dynamic response and tropical forcing is modulated by the vertical structure of the heating. In addition, in the Tropical Eastern Pacific Ocean, the total heating (Q) is approximately equal to radiative cooling (Q_r) - see Fig. 2.2c, so that

$$\frac{\partial u'}{\partial\lambda} \propto \frac{\partial}{\partial p}\left(\frac{Q_r}{S}\right). \qquad (2.9)$$

This research will quantify relationships between Q_r, longitudinal overturnings, and the IO.

2.4 Motivation for Radiative Calculations

Radiative cooling rates shown in Fig. 2.2 are model-derived quantities taken from the NCEP/NCAR Reanalysis project output fields. They are available at 6-h intervals for the entire period covered by this study. Early consideration was given to using these model-derived results rather than explicitly calculating heating rates. The main reason they were not used is the inadequacy of NCEP/NCAR Reanalysis model cloud parameterizations at temporal frequencies needed to resolve the IO.[3] Radiative calculations based on satellite-measured (ISCCP) clouds provided a much better radiative fit to satellite-measured OLR.

This point can best be demonstrated by examining a typical 5-day average OLR field as produced by the NCEP/NCAR Reanalysis model and then calculating OLR based on ISCCP fields as described in Chapter 3. Figures 2.5 and 2.6 show satellite-measured versus reanalysis-derived OLR and calculated OLR respectively for the 5-day period centered on 27 February 1991. Figure 2.5a represents the satellite-measured OLR, Fig. 2.5b the Reanalysis-derived (or calculated) OLR, Fig. 2.5c the difference between Figs. 2.5a and 2.5b, and Fig. 2.5d the middle- and high-level cloud cover only as a proxy for radiative cloud forcing. This cloud cover was derived using the maximum cloud overlap method described in Chapter 3, subsection 3.1, using middle and high level clouds only.

The importance of radiative cloud forcing is evident by the close comparison between middle- and high-level cloud cover (d) and calculated OLR (b) less than 240 W m^{-2} for both figures. Notice though that Reanalysis-derived OLR (Fig. 2.5b) shows a number of

---

[3] Mid- and high-level cloud cover are the primary components to radiative forcing.

FIG. 2. 5 Satellite-measured versus NCEP/NCAR Reanalysis-derived OLR for the 5-day period centered on 27 February 1991. Contour intervals for (a-c) are 20 W m^{-2} with values given by gray-shade key to the left of figures. Panel (c) represents the difference between (a) and (b). Panel (d) shows middle- and high-level cloud cover used a proxy for cloud radiative forcing. Satellite-measured OLR data were obtained from the Climate Prediction Center, NCEP/NOAA (courtesy of K.C. Mo) from NESDIS averages of individual satellite scans. Daily values represent averages from the twice-a-day original data interpolated to 2.5° grids described by Liebmann and Smith (1996).

27 Feb 91: Satellite-Measured versus Reanalysis-Derived OLR
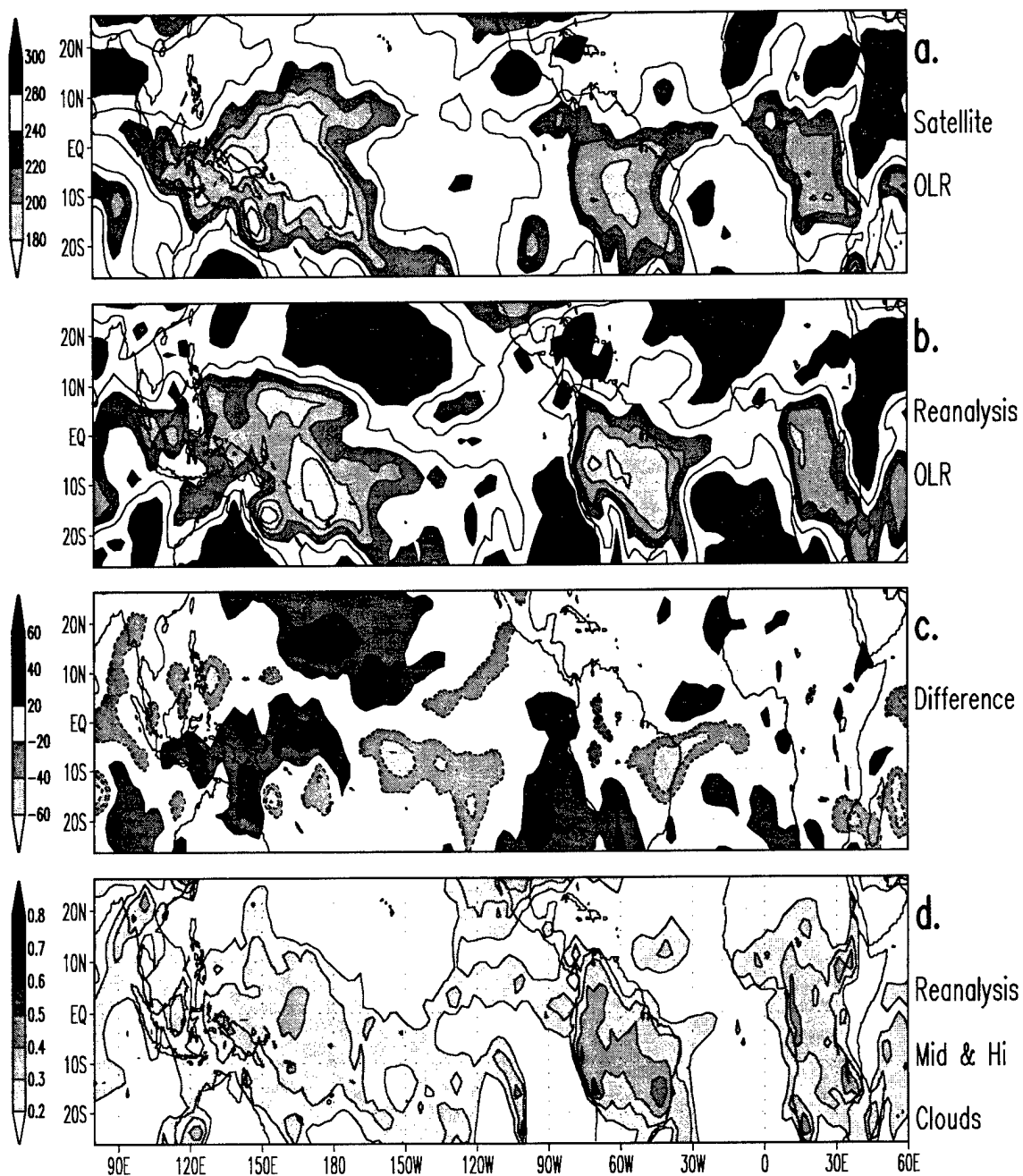
27 Feb 91: Satellite-Measured versus Calculated OLR
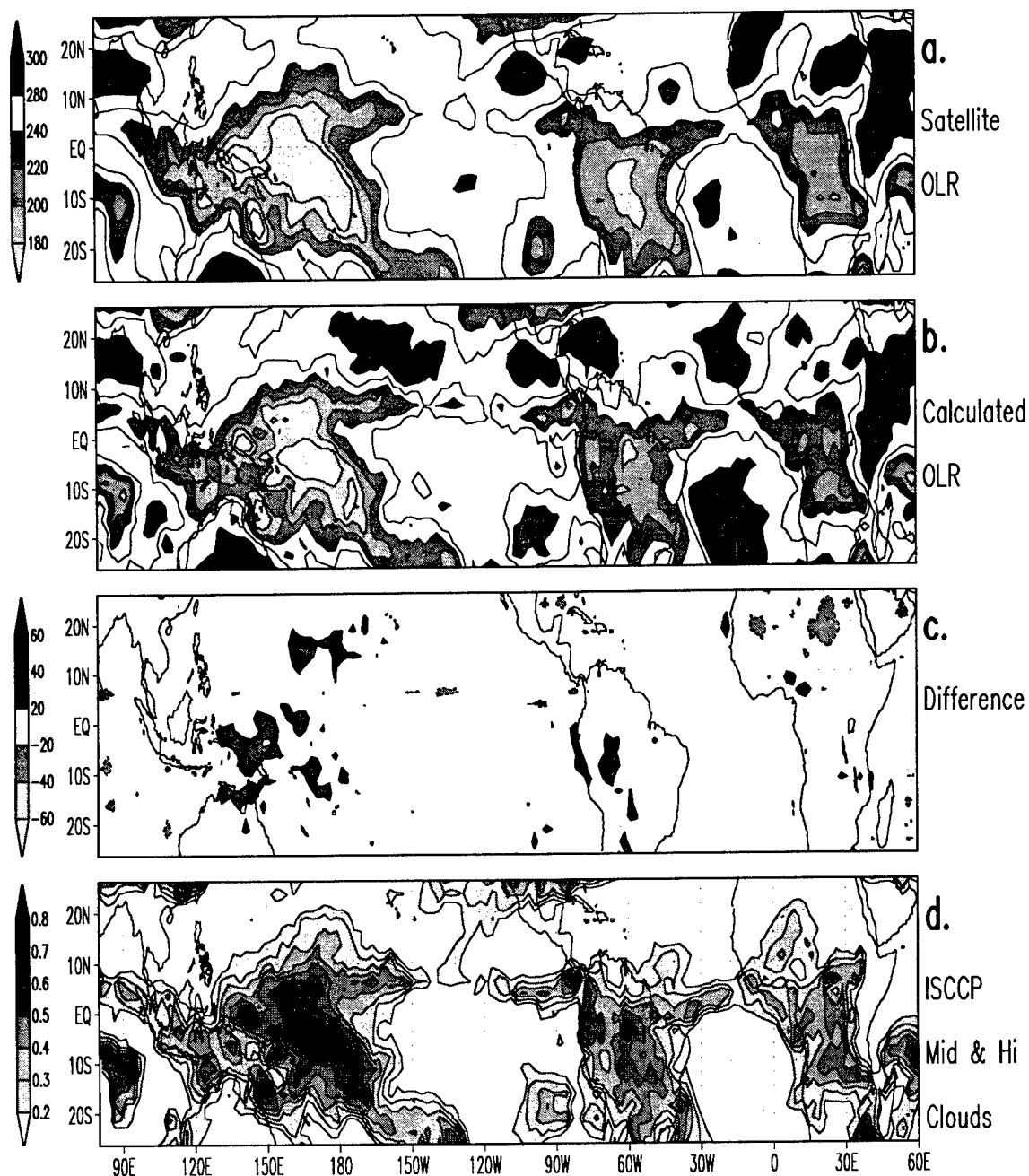
FIG. 2. 6 Satellite-measured versus calculated OLR for the 5-day period centered on 27 February 1991.

discrepancies from satellite-measurements due to differences in cloud cover shapes, particularly at the cloud boundaries. In addition, there is a total absence of Reanalysis-parameterized cloud at 15°N, 180°W and at 20°S, 95°W leading to large OLR errors in those regions (Fig. 2.5c). By comparing Fig. 2.5c with Fig. 2.6c it is obvious that radiative calculations based on satellite cloud fields are closer to observed OLR than model parameterized cloud in both extent and magnitude of OLR differences. Finally, it should be pointed out that the large difference in the amount of cloud cover shown in Fig. 2.5d (mostly in the range of 0.3-0.5) cannot be directly compared with that in Fig. 2.6d (0.3-0.8). This is because Reanalysis output cloud fields are reported only as low-, middle-, and high-level clouds which have been computed via a random cloud overlap method using unidentified model sigma levels (see Chapter 3, subsection 3.1 for definition of random cloud overlap). Therefore, individual model sigma-level cloud cover from which radiative calculations are based may not be reflected in these amounts even though the spatial shape would be.

CHAPTER 3

RADIATIVE ANALYSIS

3.1 Introduction

The interaction between radiative cooling and the propagation of the intraseasonal oscillation can only be speculated. Most theories for its creation and maintenance focus on convective signature regions of the Western Pacific Ocean identified primarily through seasonally filtered OLR. Yet, through observations of divergent wind anomalies, this tropical wave is seen to propagate through and frequently dissipate in the Eastern Pacific Ocean, a region of little or no convection. A plausible explanation is given by Garcia and Salby (1987). They argue that damped dispersion of Kelvin and Rossby waves away from the heating result in Kelvin wave westerlies propagating eastward to the point where they intercept the Rossby easterly response. In any case, observations suggest convergence in the Eastern Pacific Ocean and resulting sinking motion. It would seem reasonable to expect that here radiative cooling might interact with and possibly modify the behavior of the IO, since it is the dominant form of diabatic energy and a major energy sink in the region (see Fig. 2.2).

Recent developments have made it possible to calculate this radiative cooling response to the IO and to characterize its behavior. These developments include advances in physically describing the radiative properties of clouds, an efficient yet

accurate broadband radiative transfer model, and the availability of consistently produced and highly descriptive cloud and atmospheric data. In addition, the concurrent availability of these data over sufficiently long periods allows for the creation of a radiative climatology from which to describe seasonal radiative characteristics.

This chapter describes the steps taken to compute 5-day averaged three-dimensional tropical radiative-heating rates and fluxes for over 6 continuous years. In addition, a synopsis of derived results is included.

3.2 Model and Data

3.2.1 Radiative Transfer Model

Radiative calculations are made using the broadband radiative transfer model of Fu and Liou (1992). This model calculates fluxes and flux divergence (heating rates) via the delta-four-stream approximation to the radiative transfer equation in both solar and infrared (IR) wavelengths. In the IR, the Planck function is expressed in exponential form in terms of optical depth. The phase function and single scattering albedo are characterized for 16 atmospheric layers whose boundaries are defined by the NCEP/NCAR Reanalysis output model levels (see Fig. 2.3). These layers are assumed to be homogeneous, and vertical features are made continuous through the use of boundary conditions and internal continuity requirements described by Fu (1991). The delta-four-stream approximation is accurate to within ±5% when compared with computed "exact" adding method computations.

The spectral resolution of ice and water refractive indices includes 6 solar and 12 IR

bands.[4] In addition, nongray gaseous absorption from H_2O, CO_2, O_3, CH_4, and N_2O is incorporated using the correlated k-distribution approach. This method transforms frequency space (v) into cumulative probability space (g) for a given frequency spectral interval (Δv). This leads to a substantial reduction in numerical calculations, where ~10 000 v-intervals are replaced by a few g-intervals. Still, the computed heating rate has been checked to within 0.1 K day^{-1} as compared to line-by-line calculations. In addition, the method was shown to be exact for strong- and weak-line limits and for single lines and periodic lines. Finally, special treatment is given to calculations involving overlap bands and is described by Fu and Liou (1992).

Single scattering properties for hydrometeors of liquid, ice, rain, and graupel are parameterized. For ice, crystals are assumed to be hexagonal and scattering parameterizations are made in terms of mean effective size and ice water content (IWC). These parameterizations were derived from the results of 11 ice crystal distributions characterized by in situ aircraft observations (Fu and Liou 1993). When the mean effective ice crystal size is greater than 30 μm, scattering is calculated from results of the geometric ray-tracing program of Takano and Liou (1989). For sizes less than 30 μm a scattering program based on spheroids is used. For water droplets, Mie theory is used to parameterize single scattering properties based on liquid water content (LWC) and mean effective size. Graupel and rain shapes are also parameterized in the model but are not

---

[4] The solar spectrum is divided into 6 spectral bands between 0.2 and 3.5 μm. These bands include 0.2-0.7, 0.7-1.3, 1.3-1.9, 1.9-2.5, and 2.5-3.5 μm. The IR spectrum is divided into 12 spectral bands between 0 and 2200 cm^{-1}. These bands include 0-280, 280-400, 400-540, 540-670, 670-800, 800-980, 980-1100, 1100-1250, 1250-1400, 1400-1700, 1700-1900, and 1900-2200 cm^{-1}.

used for these large-scale calculations.

3.2.2 Data Sources

Input data for radiative calculations are derived from a number of sources. First, atmospheric temperature (1000-10 mb), atmospheric moisture (1000-300 mb), and surface temperature are obtained from the 6-h NCEP/NCAR Reanalysis dataset. Second, in order to parameterize cloud-LWC and -IWC, fractional cloud cover and cloud optical depth are used from the 3-h ISCCP/C1 dataset (Rossow and Schiffer 1991). Third, seasonal surface albedo climatology is adopted from Hummel and Reck (1979) over oceans and from Matthews (1985) over land. Fourth, surface emissivity is set to unity except for over tropical desert areas where satellite-derived surface emissivities reported by Prabhakara and Dalu (1976) are used. Fifth, TOVS total ozone amounts as reported in the ISCCP/C1 data are used as a basis to derive ozone profiles. In addition, the model is "tuned" to satellite-observed OLR obtained from the daily averaged wideband scanner instrument ERBE/S9 data.

3.3 Radiative Analysis Procedure

Radiative analysis should emphasize the four-dimensional variability of calculated radiative heating rates pertinent to the study of the intraseasonal oscillation. This guidance leads to the selection of the following spatial and temporal resolutions. The horizontal resolution of the 2.5° X 2.5° ISCCP grid within the tropics was selected and should be more than adequate to resolve waves which have zonal structures on the order of wave number one and two. Specifically, there are 144 grid points in longitude starting

at 1.25°E, and 24 grid points in latitude between 28.75°S. and 28.75°N. In the vertical, the 17 levels used by the NCEP/NCAR Reanalysis (see Fig. 2.3) seem ideally spaced to resolve the vertical structure of the tropical wave modes believed to be responsible for the IO (see Nogués-Paegle et al. 1989). Finally, in order to perform meaningful statistical correlations, concurrent radiative and dynamical calculations are performed over as long a period as possible. Therefore, the period from January 1985 through June 1991 was selected based on concurrent data availability and the variety of events found there, including enhanced events during the 1987 El Niño episode. In addition, all calculations are made for 5-day averaged data in order to describe the primary intraseasonal variations with time scales roughly between 10 days and 3 months.

3.3.1 Processing ISCCP/C1 Cloud Data

Cloud optical depth properties are given for ISCCP/C1 visible (VIS) data which are available for daytime hours only. Therefore, in order to properly weight the pentad (5-day) average, nighttime cloud amounts and optical properties are interpolated between the last evening and first morning observations at the standard ISCCP time intervals.[5] Next, cloud data are averaged into 5-day pentad averages.

The VIS vertical cloud structure is present in the form of cloud cover and optical depth and given for seven levels of cloud-top pressures and five optical depth ranges (see Fig. 2.4). From this, a vertically representative profile of cloud-LWC and -IWC is derived from which scattering parameterizations are based in the radiative code. After experimenting with different techniques, the following procedure was selected. For

---

[5] Time intervals for ISCCP/C1 data are 00, 03, 06, 09, 12, 15, 18, and 21 UTC.

LWC, the parameterization scheme of Slingo (1989) was used. This parameterization is given by:

$$\tau_i = LWP\left(a_i + \frac{b_i}{r_e}\right),$$ (3.1)

and

$$LWP = \int_{cloud\ base}^{cloud\ top} LWC\ dz,$$ (3.2)

where τ_i is the optical depth, LWP is liquid water path, a_i and b_i are parameterization coefficients. The (i) indices refer to a given spectral interval, for which the 0.57-0.64 μm interval was selected as being representative for scattering. This spectral range was selected because it contains the largest portion of solar energy for those coefficients specified in the parameterization. Actually, choosing coefficients from this part of the visible spectral interval does not change the derived LWC by more than ±5% for the entire visible spectrum (0.4-0.7 μm). The equivalent radius of drop size distribution (r_e) is defined as:

$$r_e = \frac{\int_0^\infty n(r)r^3 dr}{\int_0^\infty n(r)r^2 dr},$$ (3.3)

where r is the drop radius (μm) and n(r) is the drop size distribution function. A value of

r_e=10 μm was selected in order to be consistent with that used in the ISCCP radiative calculations. For IWC, the parameterization of Fu and Liou (1993) is used. This parameterization is given by:

$$\tau_i = \int_0^\infty \beta_i \, dz,$$

(3.4)

and

$$\beta_i = IWC \sum_{n=0}^N \frac{a_n}{D_e^n},$$

(3.5)

where β_i is the extinction coefficient, a_i and b_i are parameterization coefficients. The n-indices refers to the numerical fitting, where N is the total number of terms required to achieve a prescribed accuracy. We select N=1, which gives an accuracy to within ±5%. The parameterization coefficients used correspond to the visible spectrum as was done with the LWC calculations. The mean effecting ice crystal size (D_e) is analogous to r_e and is defined as:

$$D_e = \frac{\int_{L_{min}}^{L_{max}} D \cdot DLn(L)dL}{\int_{L_{min}}^{L_{max}} DLn(L)dL},$$

(3.6)

where D is the width of an ice crystal, n(L) the ice crystal size distribution, and L_{min} and L_{max} are the minimum and maximum lengths of ice crystals respectively. A mean

effective size of 41.5 μm was selected which is representative of a cirrostratus cloud type. Finally, the decision to use LWC- or IWC-parameterizations is based on the mean layer temperature. For values less than -15 C, IWC is used, otherwise LWC is used.

In order to use the cloud water parameterizations just described, a vertical cloud structure must be specified. For this, the cloud classification scheme used in the ISCCP data is adopted (see Table 3.1). The steps used to vertically distribute clouds are now described. One, cumulonimbus (Cb) and nimbostratus (Ns) cloud fractions are distributed vertically down to a climatological cloud base (1700 m AGL). Other cloud types are extended into the ISCCP-defined levels for which they are reported. Table 3.1 lists the cloud thickness used for these cloud types which were derived from zonally averaged cloud thickness climatology reported by Liou (1992). Two, total cloud cover (η_t) is computed from ISCCP data. This is necessary because the ISCCP data have already been averaged into pentads and because these data represents only the satellite "cloud-top" view, where the cloud structure underneath cloud-tops must be estimated. Total cloud cover is calculated by a weighted average of random- and maximum-overlap methods such that:

$$\eta_t = C\eta_r + (1-C)\eta_m, \tag{3.7}$$

where

$$\eta_m = \max(\eta_1, \eta_2, \dots \eta_7), \tag{3.8}$$

and

Table 3.1. ISCCP cloud types (Rossow and Schiffer 1991) with associated zonally averaged climatological cloud thickness (adapted from Liou 1992).

Cloud Classification	Cloud Type	Cloud Thickness (m)
High[a]	Cirrus (Ci)	1700
	Cirrocumulus (Cc) or Cirrostratus (Cs)	1700
	Cumulonimbus (Cb)	Extended[d]
Middle[b]	Altocumulus (Ac) or Altostratus (As)	1000
	Nimbostratus (Ns)	Extended[d]
Low[c]	Cumulus (Cu) or Stratocumulus (St)	1000
	Stratus (St)	200

[a] High clouds are contained in ISCCP levels 50-180, 180-310, and 310-440 mb.

[b] Middle clouds are contained in ISCCP levels 440-560, and 560-680 mb.

[c] Low clouds are contained in ISCCP levels 680-800, and 800-1000 mb.

[d] For Cb and Ns, cloud thickness is computed by calculating thickness between reported cloud top and a climatological cloud base (1700 m AGL).

$$\eta_r = 1 - \left[(1 - \eta_1)(1 - \eta_2)...(1 - \eta_7)\right],$$ (3.9)

where η_m is maximum cloud overlap, $\eta_{1\text{-}7}$ are individual layer cloud cover, η_r is random cloud overlap and C is a tuning factor described in subsection 4.1. The random cloud overlap method used here is a seven-level extrapolation of the three-level method used by Lee et al. (1992). Three, optical depth is reported in five ranges as shown in Fig. 3.1. The ambiguity implicit in choosing a discrete value within these ranges is used to vertically normalize the LWC/IWC parameterizations to a tropically typical water content profile used by Cox and Griffith (1979), see Table 3.2. The optical depth assigned to the LWC (or IWC) parameterization is then

$$\tau = \tau(1 - 5) + W\Delta\tau$$ (3.10)

where $\tau(1\text{-}5)$ is the ISCCP-specified optical depth (Fig. 3.1), W is the interpolation weight (Table 3.2), and $\Delta\tau$ is the interpolation range used by the ISCCP/C1 data. The optical depth assigned to multilayer convective clouds (Cb and Ns) is computed in the same manner and then distributed throughout the multiple model layers containing these
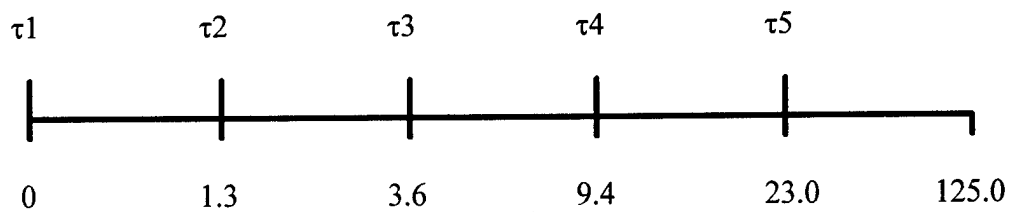
FIG. 3. 1 ISCCP-specified optical depths.

Table 3.2. Optical depth interpolation weights based on tropical cloud water contents used by Cox and Griffith (1979).

ISCCP Pressure Levels (mb)	Interpolation Weight[a]
50-180	0.01
180-310	0.03
310-440	0.09
440-560	0.20
560-680	0.36
680-800	0.69
800-1000	1.00

[a] These values are dimensionless. However, they can be interpreted as cloud water content in units of $g\ m^{-3}$.

cloud types. Four, 7-level cloud water contents are interpolated to the relevant 17-levels adopted from the NCEP/NCAR Reanalysis (Fig. 4) and used by the radiation code.

3.3.2 Processing ISCCP/C1 TOVS Ozone Data

The ISCCP/C1 database contains ozone column abundance as measured from the TOVS instrument aboard NOAA polar-orbiting satellites. From this integrated value, ozone mixing ratio at each grid point for all vertical levels is estimated by curve fitting to seasonal ozone profiles. These tropical seasonal ozone profiles are derived by averaging seasonal climatology of ozonesonde observations reported by Komhyr et al. (1989) for

station data at two near-tropical locations. The first is from Hilo, Hawaii (19°N, 155°W) and the second is from American Samoa in the South Pacific Ocean (14°S, 170°W).

3.3.3 Processing NCEP/NCAR Reanalysis Data

Temperature and moisture data from the NCEP/NCAR Reanalysis are processed consistent with cloud data. That is, fields are interpolated onto the 2.5° X 2.5° grid used by ISCCP data and then averaged into 5-day pentads. Moisture fields are converted from relative humidity to mixing ratios and saturated mixing ratios. Mixing ratio is set to saturated wherever there are clouds. The computation of saturated mixing ratio is made with respect to ice for levels with temperatures less than -15°C and with respect to water for levels with temperatures 0°C and above. Values between 0°C and -15°C are computed by linear interpolation. In addition, since relative humidity is only reported up to 300 mb, stratospheric water vapor is extrapolated from the 300-mb values. This is done so that:

$$mr(lvl) = mr(300\ mb)WT \qquad (3.11)$$

where mr(lvl) is the extrapolated mixing ratio at each level above 300 mb, mr(300 mb) is the observed 300-mb mixing ratio, and WT is the fractional amount of water vapor at each level relative to the 300-mb value as derived from the US Standard Atmosphere, 1976.

This method of stratospheric moisture extrapolation was one of three methods tested and was selected primarily because it was the only one that consistently produced a smooth radiative profile near the 300-mb boundary. One of the alternative methods

tested was simply that of setting stratospheric moisture to zero. The other method tested was a routine obtained from NCEP (courtesy of Dr. Henry Juang, Environmental Modeling Center) which performed an exponentially decreasing moisture extrapolation into stratospheric layers and used satellite-derived microwave limb moisture profiles (with 10° latitudinal resolution) above 80 mb. Of the three methods tested, there was virtually no change in the calculated OLR at 10 mb.

3.3.4 Surface-Temperature, -Albedo, and -Emissivity

During preliminary comparisons with ERBE-measured OLR, large systematic errors were discovered in calculated OLR over specific land regions. These regions included the Sahara dessert, South Africa, the Tibetan Plateau, parts of Australia, and regions of South America particularly over the Andes range. These discrepancies have been largely mitigated by the following adjustments to input surface parameters. Firstly, the source for surface temperatures was switched from ISCCP-reported satellite-retrieved values to the surface temperatures reported by the NCEP/NCAR Reanalysis. Problems with using surface temperatures from the NMC (now NCEP) forecast analysis model as reported by Rossow et al. (1989) have apparently been resolved within the NCEP/NCAR Reanalysis model, at least within tropical latitudes (30°S to 30°N). Secondly, substantial improvements were made over desert areas by allowing for surface emissivities less than one in those regions. Specifically, surface emissivity for the 1250-800 cm^{-1} spectral region is specified as estimated by Prabhakara and Dalu (1976). Thirdly, surface albedo has been spectrally adjusted between 0.2 - 0.7 μm using the findings of Cess and Vulis

(1989) and a simple spectral energy-weighted correction suggested by Fu (1995). This correction assumes that:

$$\alpha_{total} = \frac{W_v}{S}\alpha_v + \frac{W_n}{S}\alpha_n, \tag{3.12}$$

where α_{total} is the total solar surface albedo, α_v and α_n are the visible and near-infrared solar surface albedos respectively, W_v and W_n are the visible and near-infrared spectral energies respectively, and S is the total solar spectral energy (solar constant). In addition, it was estimated from the results of Cess and Vulis that $\alpha_v/\alpha_n \approx 0.3$ for all vegetative surface types.

3.3.5 Radiative Calculations

Radiative calculations are made using 5-day mean input fields rather than calculating radiative profiles every 3 or 6 h, filling missing (night time) cloud values and then averaging these radiative fields for 5 days. Indeed, tests performed by Zhang et al. (1995) showed that the best way to fill missing values is to interpolate in time the physical properties of the atmosphere and then make radiative calculations rather than interpolating calculated fluxes. Furthermore, in order to calculate radiative fluxes and heating rates based on data representing 5-day mean conditions, the following three primary assumptions were made. One, the amount of solar radiation available during a 24-h period is calculated by multiplying the solar constant (set at 1360.3 W m^{-2}) by the fractional amount of daylight at that latitude and date. Two, the 5-day mean sun-sky position is approximated by calculating the mean cosine of the solar zenith angle for a given latitude for the third day within a pentad. Three, radiative heating rates (and fluxes)

are computed at each gridpoint for cloudy- and clear-sky conditions. The total heating

rate is then estimated (as described by Lee et al. 1992) by

$$\left(\frac{\partial T_r}{\partial t}\right)^{pc} = \eta_t \left(\frac{\partial T_r}{\partial t}\right)^{c} + (1 - \eta_t)\left(\frac{\partial T_r}{\partial t}\right)^{nc},$$ (3.13)

where $\partial T_r/\partial t$ is the radiative heating rate, and the superscripts pc, c, and nc represent

partly cloudy, cloudy, and clear conditions, respectively. In addition, in order to calculate

the radiative heating rate associated with cloudy sky conditions, calculated cloud-LWC

(or -IWC) is fractionally distributed throughout the entire model layer based on η_t for the

horizontal extent and on cloud thickness relative to layer thickness for the vertical.

Finally, concentrations of gaseous absorbers, other than water vapor and ozone as

previously discussed, are set to fixed values. These values are 330.0 parts per million

volume (ppmv) for CO_2, 1.6 ppmv for CH_4, and 0.28 ppmv for N_2O.

3.3.6. Isolating Intraseasonal Oscillation Signatures by Filtering Radiative Calculations

A spectral filter is applied to calculated results in order to identify the radiative

heating field variations associated with the IO. This filter removes heating rate signatures

that do not fall within the spectral range of 25-80 days (5-16 pentads). Consequently, the

magnitude of these filtered IO radiative anomalies are reduced to about 1/10th of the

nominal daily radiative cooling rate. For instance, a typical value for radiative cooling at

600 mb in the Eastern Pacific Ocean is -1.0 K day^{-1} whereas a typical IO-filtered anomaly

in the same region is around ±0.1 K day^{-1}.

3.4 Model Tuning and Validation

3.4.1 Cloud Overlap Tuning Factor

The cloud overlap tuning factor (C) given in Eq. (3.7) was derived by tuning calculated OLR produced by the model to ERBE-measured OLR for the month of June 1985. Daily ERBE OLR results were averaged into pentads and then compared with model calculated outgoing longwave fluxes at 10 mb. The tuning factor was then iteratively adjusted to produce the smallest average percent error over the entire tropical grid. The resulting optimum value for C was found to be 0.17 which produced an area-averaged error of 4.1%. This value was then used throughout radiative calculations for the 6½ year period between January 1985 and June 1991. In effect, use of this tuning factor fixes the total cloud cover for each grid point to a value close to that produced by the maximum overlap cloud layering method given by Eq. (3.8).

3.4.2 Validation

After computing the three-dimensional tropical radiative structure for the 6½-year period of this study, calculated outgoing radiative longwave fluxes at 10 mb were checked against satellite-measured OLR. During the comparison one major discrepancy was discovered and then corrected. Specifically, large differences between calculated and satellite-measured OLR were discovered for the months of October and November of 1988 and 1989. These differences were caused by a misreporting of ISCCP cloud dates for those years (reported October and November 1988 cloud data were actually data for October and November 1989 and vice versa). Radiative calculations were then re-run and checked.

Figures 3.2-3.3 show an example comparison made for the pentad period centered on 14 March 1987 and is typical of other periods compared. In Fig. 3.2, satellite-measured OLR values (a) show remarkably good agreement as to the location of cloud depicted by the lower values of OLR (values less than $240\ W\ m^{-2}$). This can almost wholly be attributed to the correct cloud cover locations and extent as input from the satellite-derived ISCCP cloud data. Discrepancies between calculated- and satellite-observed OLR are shown in Fig. 3.3a as differences and in Fig. 3.3b as percentage difference relative to OLR measurements. Again, the most striking feature in both of these panels is the close agreement between calculated- and satellite-measured-OLR for nearly all of the tropics.

In order to determine if there were any systematic biases, comparisons were made between seasonally-averaged satellite-measured OLR and seasonally-averaged calculated OLR. Seasons were defined by January-March, April-June, July-September, and October-December OLR pentad averages for the 6½-year period representing northern hemispheric winter, spring, summer, and fall respectively. Figure 3.4 shows the winter (a) and summer (b) differences between satellite-measured and calculated OLR; these seasons represented extreme positions of annual OLR cycle in the tropics with spring and fall being transition seasons. All of the positive differences (calculated OLR larger than measured OLR) are located in regions of active tropical convection. Figure 3.5 shows bias as defined by the OLR-difference divided by the square root of OLR-difference squared and is shown as a compliment to Fig. 3.4 in order to highlight biased regions. Notice in Fig. 3.4 the northern migration from winter to summer of OLR differences over
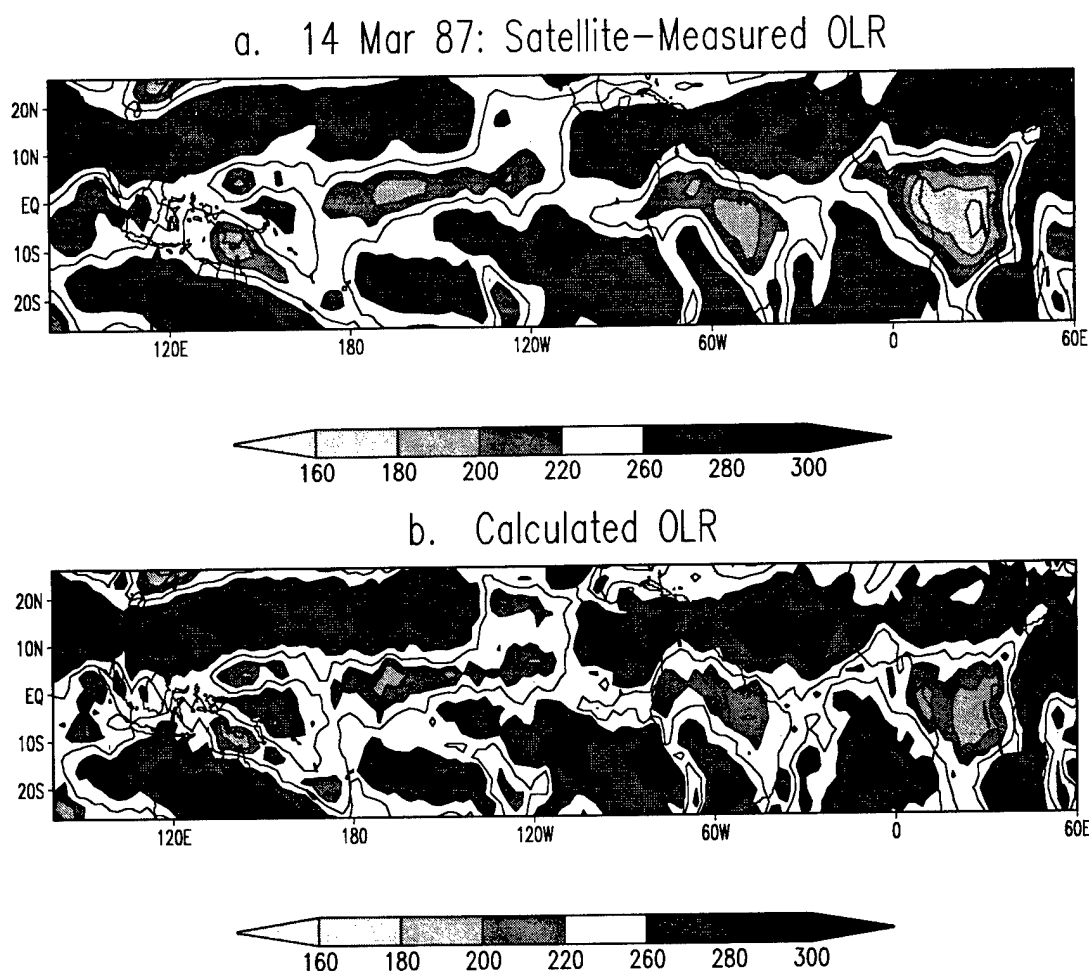
FIG. 3. 2 Satellite-measured OLR (a) and OLR calculated by the radiative model of Fu and Liou (1992) - (b). Values represent 5-day average (pentad) period taken from 12 March 1987 through 16 March 1987. Units are W m^{-2}. Satellite-measured OLR data were obtained from the Climate Prediction Center, NCEP/NOAA (courtesy of K.C. Mo) from NESDIS averages of individual satellite scans. Daily values represent averages from the twice-a-day original data interpolated to 2.5° grids described by Liebmann and Smith (1996).

a. 14 Mar 87: OLR Difference
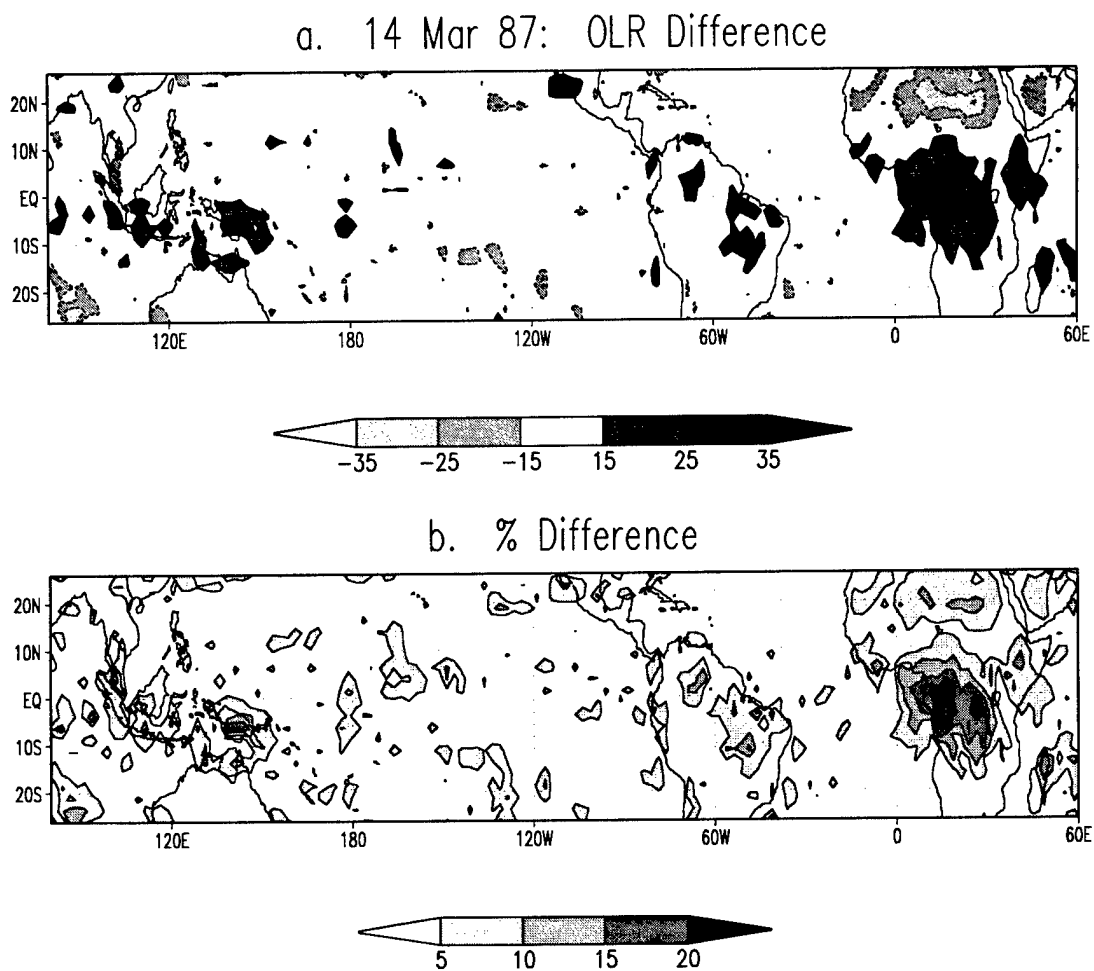
b. % Difference

FIG. 3. 3 Difference between calculated OLR and satellite-measured OLR (a) shown in Fig. 3.2 (units in W m^{-2}). Panel (b) shows this difference as a percentage relative to satellite-measured OLR.

Calculated-Measured OLR Difference
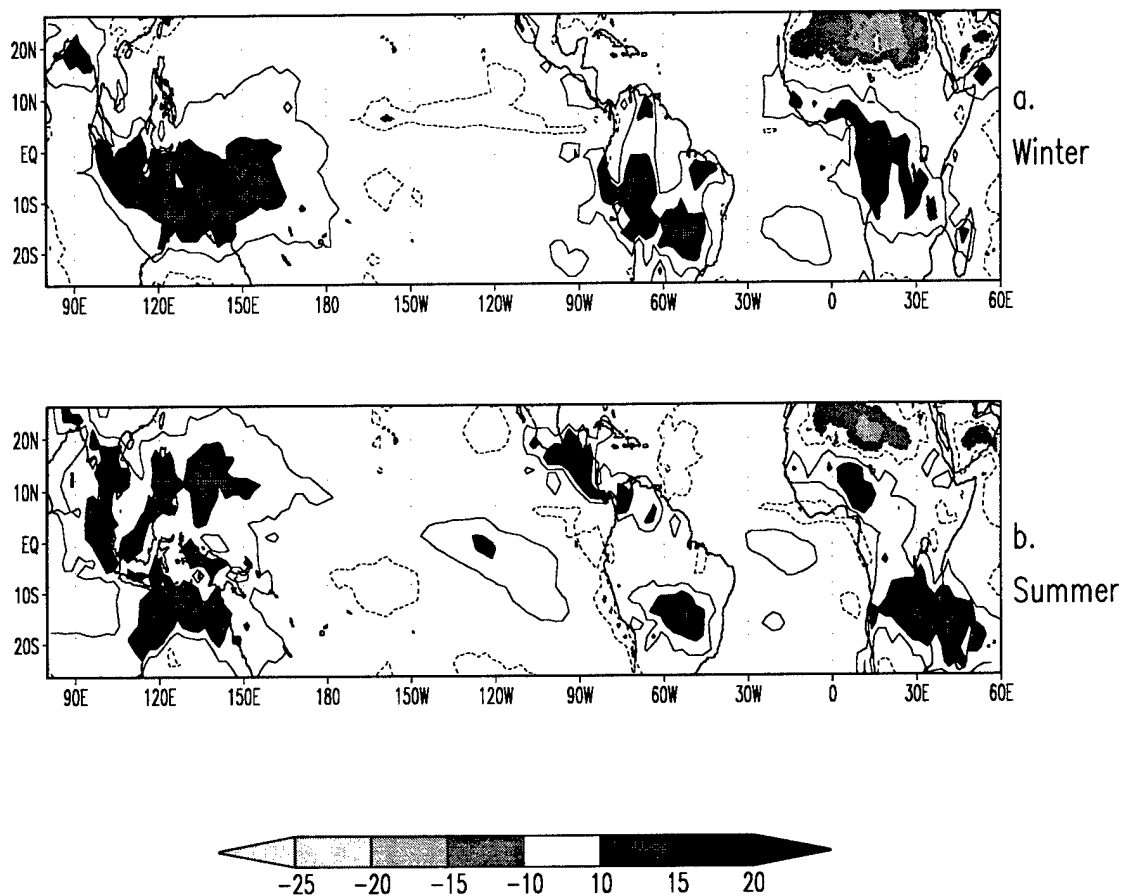
FIG. 3. 4 Difference between (seasonally averaged) calculated and satellite-measured OLR in units of W m^{-2}. Winter season (a) is defined as all OLR pentads averaged for January-March for 6½-year period and summer season (b) is all pentad averages taken between July-September for same period.

FIG. 3. 5 Bias of seasonal OLR difference shown in Fig. 3.4 for both (a) winter and (b) summer seasons.

the Western Pacific Ocean and South and Central America associated with seasonal migration of convection centers. One possible explanation for the positive anomalies over tropical land areas is an underreporting of cloud optical depth over these regions when diurnally enhanced convection is active. For these cases, using 5-day average cloud optical depth properties, where night time values are interpolated, may not be representative of the mean 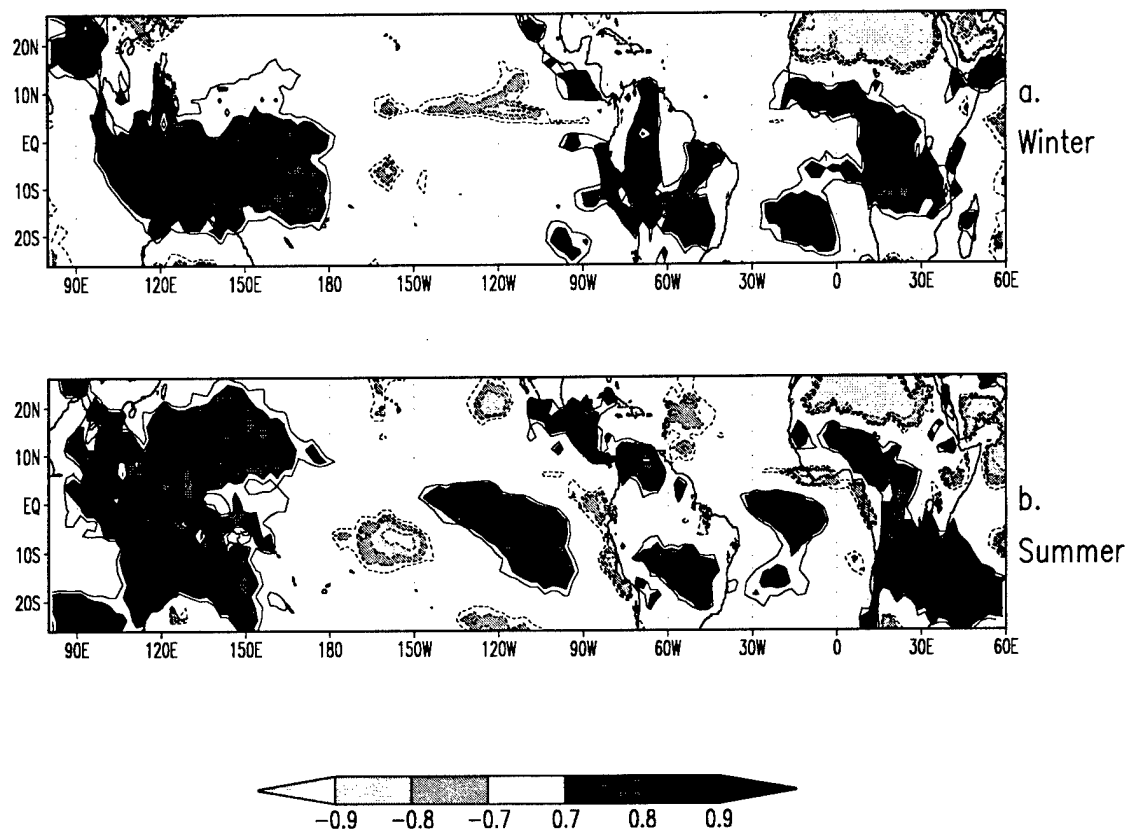conditions. The positive discrepancies over broad ocean areas (predominately in the Western Pacific Ocean) seem to randomly appear within oceanic convective systems such as the Inter-Tropical Convergence Zone (ITCZ) or the South Pacific Convergence Zone (SPCZ). This randomness can be seen in the one pentad OLR comparisons of Fig. 2.6 and Figs. 3.2-3.3. The cause for this inaccuracy is more tenuous and is probably related to the combination of assumptions made pertinent to convective cloud types (Cb and Ns), especially those regarding cloud water content as derived from optical depth and cloud thickness as well as those regarding cloud cover and cloud layering. Finally, it is evident that surface emissivity and/or surface albedo assumptions (discussed in subsection 3.4) do not entirely resolve negative OLR differences over the Sahara desert.

The vertical representativeness of calculated heating rates and fluxes cannot be directly validated since three-dimensional observations of these quantities do not exist. However, the overwhelming contributor in moderating the radiative profile is clouds. Therefore, by selecting areas of low-level-only, mid-level-only, and high-level-only cloud types and then comparing the calculated OLR to ERBE-measured OLR for those regions, an estimate as to the vertical representativeness of calculated radiative parameters can be

made. Five pentads containing areas with all three of the isolated cloud types were examined. An average longwave radiative profile for each of the cases was calculated. Next, the calculated upwelling longwave flux at 10 mb was compared with ERBE-measured OLR for those areas. The results were consistently good, with agreement within ± 10 W m^{-2} for all cases.

Based on the tests just described, we conclude that the three-dimensional radiative profiles calculated here are generally accurate to within ± 10 W m^{-2} for layered cloud types and even better than that for clear skies. Errors within convective cloud types are as high as ± 40-50 W m^{-2} for a few individual cases, but the majority fall within ± 20 W m^{-2} and have a positive bias (meaning radiative calculations randomly underestimate the cooling effect of convective clouds). It is likely that calculations in these regions could be improved by using a more complex tuning constant C. For instance one could allow for latitudinal and seasonal variations of C as well as using a different constant for convective clouds than that used for stratiform clouds. However, since the aim of this study is to evaluate the radiative structure of the Eastern Pacific Ocean, an area of mostly clear skies or low-level stratiform clouds, this level of processing is not necessary, and errors within the Eastern Pacific Ocean of ± 10 W m^{-2} seem acceptable. Finally, radiative calculations on this spatial and temporal scale over the entire tropics are believed to be unique, and these errors, even over convective areas, may be acceptable for other research applications.

3.5 Results

Calculated results are presented by first describing the three-dimensional total radiative heating field and then the anomalous radiative heating field associated with the IO. For total radiative heating rates, seasonal variations are characterized by average January and July results.

Since the total radiative heating structure is largely controlled by cloud forcing, a knowledge of cloud cover and vertical cloud structure is necessary in order to analyze the radiative results. Figure 3.6 shows the average January cloud cover for five vertical levels as derived from ISCCP/C1 data. One of the main features seen in this figure is the deep convection visible in the Indian Ocean and the Western Pacific Ocean along the Inter Tropical Convergence Zone (ITCZ) and South Pacific Convergence Zone (SPCZ). In addition, clouds in the Central- and Eastern-Pacific Ocean are characterized by the narrow band of shallow convection within the ITCZ as well as a large area of low-level stratus off the west coast of South America. For the July averages shown in Fig. 3.7, a number of differences from the January case are evident associated with a northward seasonal progression of cloudiness. First, the amount of deep convection in the Indian Ocean and Western Pacific ocean is greatly reduced. Second, convection within the ITCZ over the Eastern Pacific Ocean is deeper and more extensive. Third, there is an expanded area of low-level stratiform clouds off South America.

Vertical cross-sections of total radiative heating (K day^{-1}) for five latitudinal slices (20°S, 10°S, Eq., 10°N, and 20°N) are shown in Fig. 3.8 for the January average and in Fig. 3.9 for the July average. The most prominent feature in the tropical northern hemisphere in January is the large amount of radiative cooling at 20°N centered at about

January Average Cloud Cover
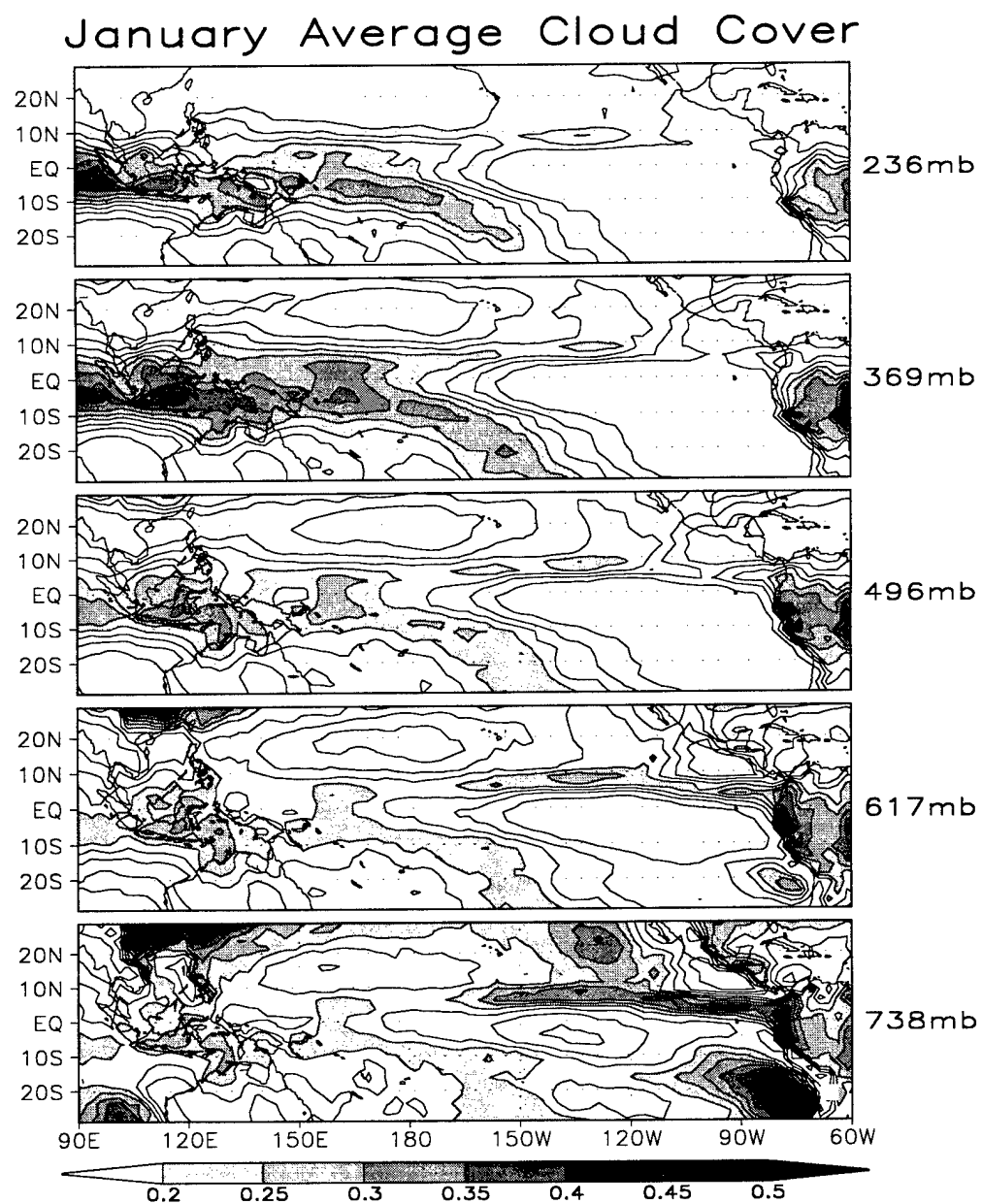
FIG. 3. 6 Average January cloud cover fraction for five vertical levels as derived from ISCCP/C1 data. Pressure levels represent the midpoint of the ISCCP-defined layer. Contour interval is 0.05 with values greater than 0.2 shaded as indicated by the key.

July Average Cloud Cover
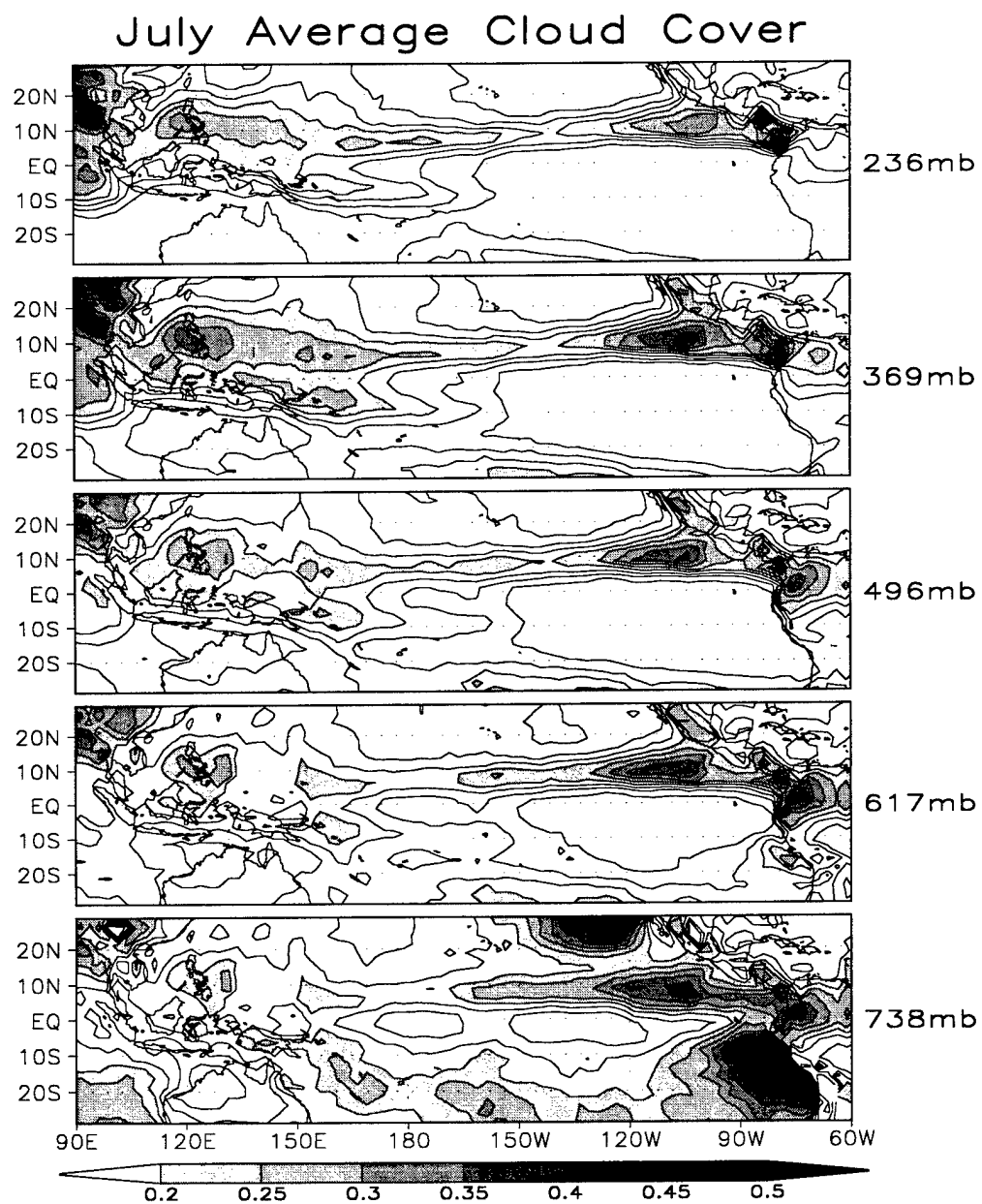
FIG. 3. 7 Average July cloud cover fraction.

January Average Radiative Cooling
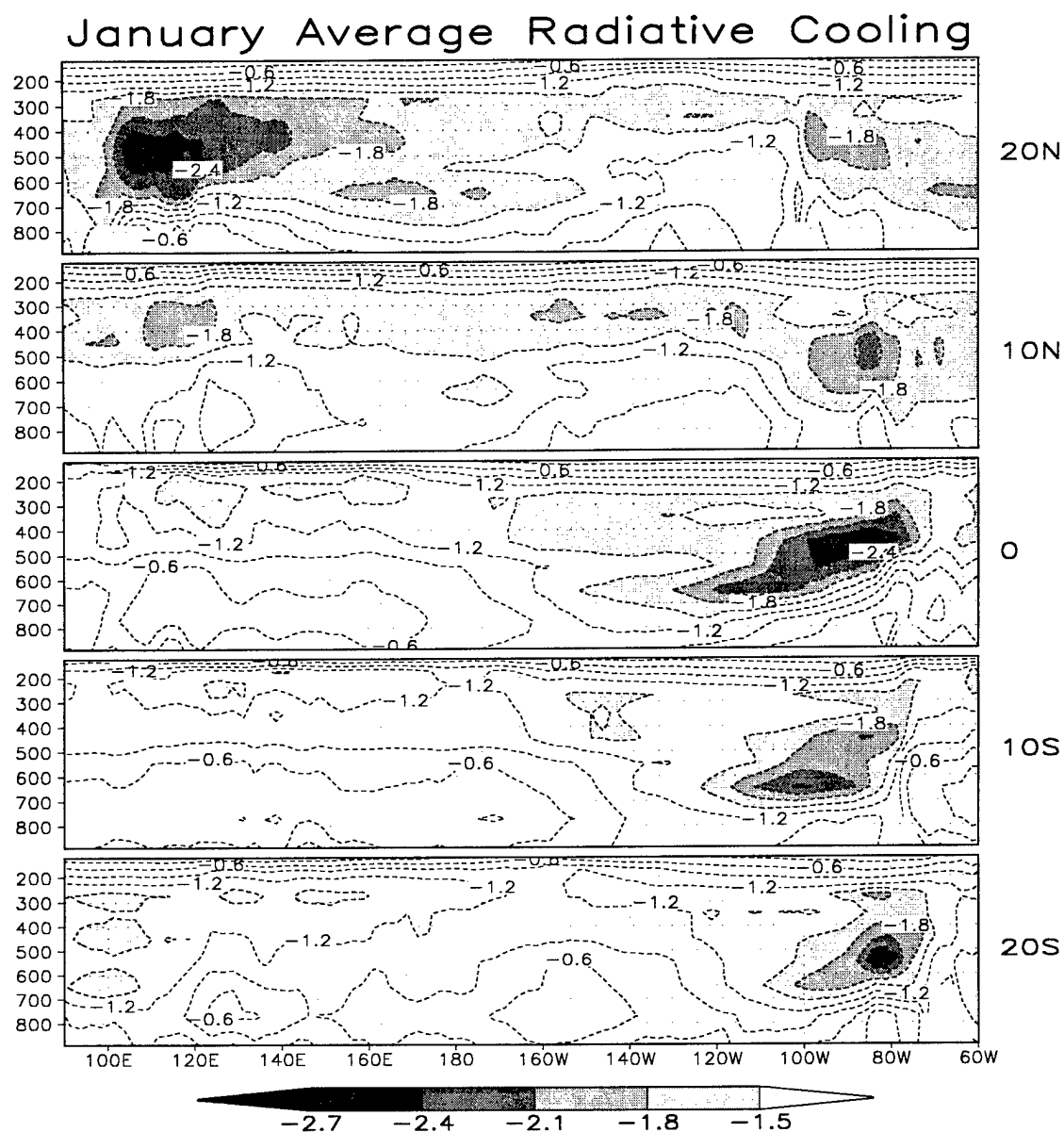
FIG. 3. 8 Average January total radiative heating rate (K day⁻¹) from 1000-10 mb for

cross-sections at 20°N, 10°N, equator, 10°S, and 20°S. Contour interval is 0.3 K day⁻¹

with contours smaller than -1.5 K day⁻¹ shaded as indicated by the key.

FIG. 3. 9 Average July total radiative heating rate.

500 mb over Asia (~110°E). This cooling is located in a relatively cloud-free area as shown in Fig. 3.6 and is related to the subsiding branch of the local Hadley cell with origins at equatorial latitudes at similar longitudes. In fact, as should be expected, the most prominent areas for radiative cooling in Figures 3.8-3.9 are located in regions of little or no mid- and high-level cloudiness as shown in Figures 3.6-3.7. This is because in those regio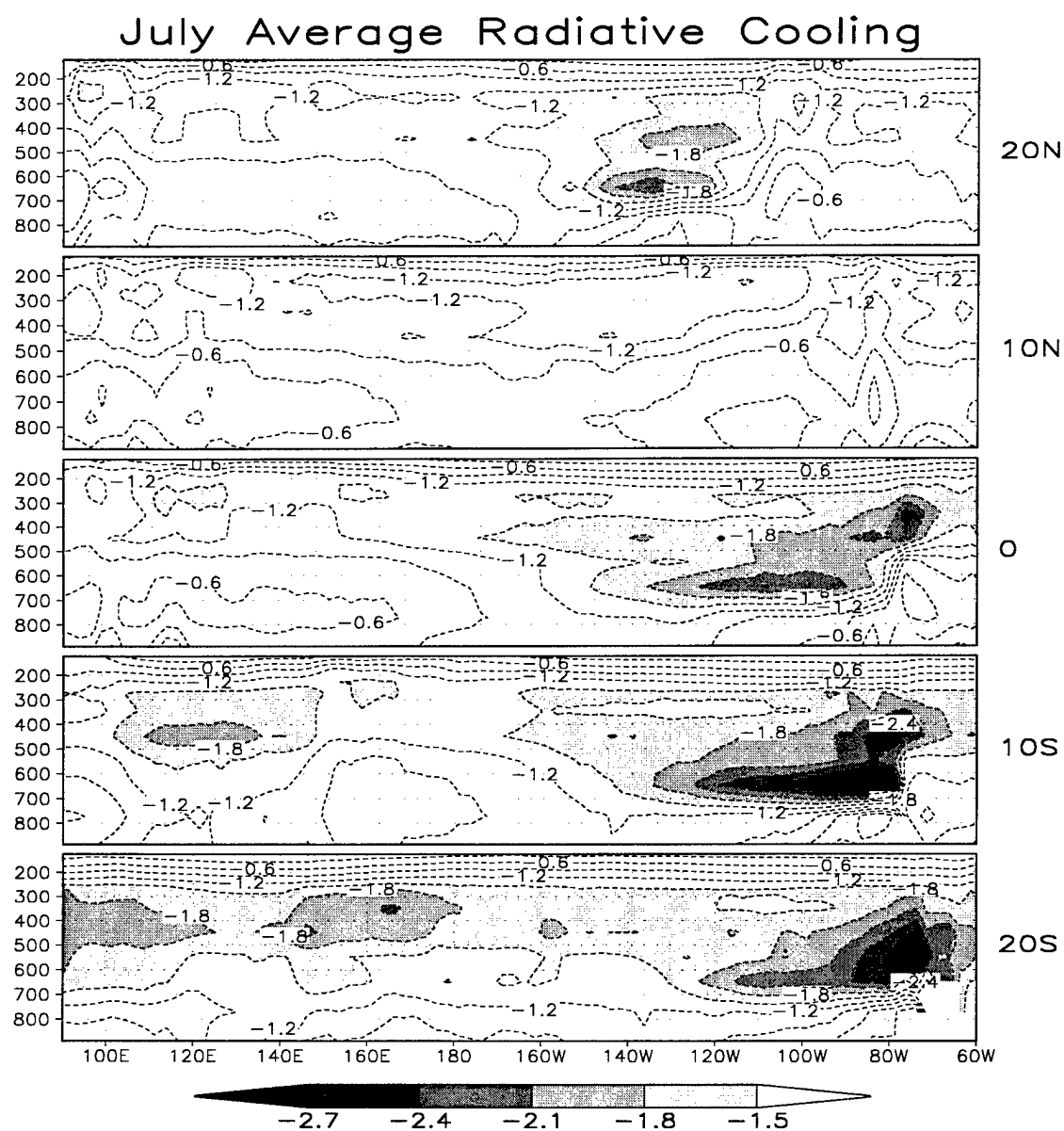ns, radiative cooling is really the only component to diabatic heating and need not compete with the greenhouse effect of clouds. The other prominent feature of Fig. 3.8 is the expanse of mid-level radiative cooling that occurs in both hemispheres in the Eastern Pacific Ocean but is especially strong from the equator and southward. Also, note the longitudinal tilt to the level of maximum cooling in that region due to a longitudinal thickening of low-level clouds increasing from west-to-east in the Eastern Pacific Ocean. For the July average radiative cooling (Fig. 3.9), there is an increased magnitude as well as increased longitudinal extent to the cooling maximum in the region of Eastern Pacific Ocean in the Southern Hemisphere. As can be seen from Fig. 3.7, this is due to an increasing longitudinal extent to mid- and high-level cloud-free areas and is not affected by the increased low-level clouds off the west coast of South America. Indeed, since low-level cloud tops are in general below the effective radiative level for clear skies, it is not expected that they would affect radiative cooling. Finally, there is a decrease in radiative cooling at 10°N in the Northern Hemisphere Eastern Pacific Ocean due to increasing mid- and high-level cloud cover.

The radiative cooling response to the IO can best be shown through a Hovmöller diagram of radiative cooling anomalies. Figure 3.10 shows "positive" and "negative" anomalies produced from filtered radiative cooling calculations for the 1987 "El Niño"

FIG. 3. 10 Radiative cooling anomalies at 648 mb during the 1987 "El Niño" year (units are K day^{-1}). Anomalies are defined as the remaining signal after filtering out frequency variabilities smaller than 20 days or greater than 90 days and then averaging those between 10°S and 10°N. Negative anomalies are shown by dashed lines with values smaller than -0.1 plotted at a contour interval of 0.1. Positive anomalies are shown by thin solid lines and are shaded as indicated by the gray-scale key. The thick solid line indicates the subjectively estimated position of the IO for a given date and longitude.
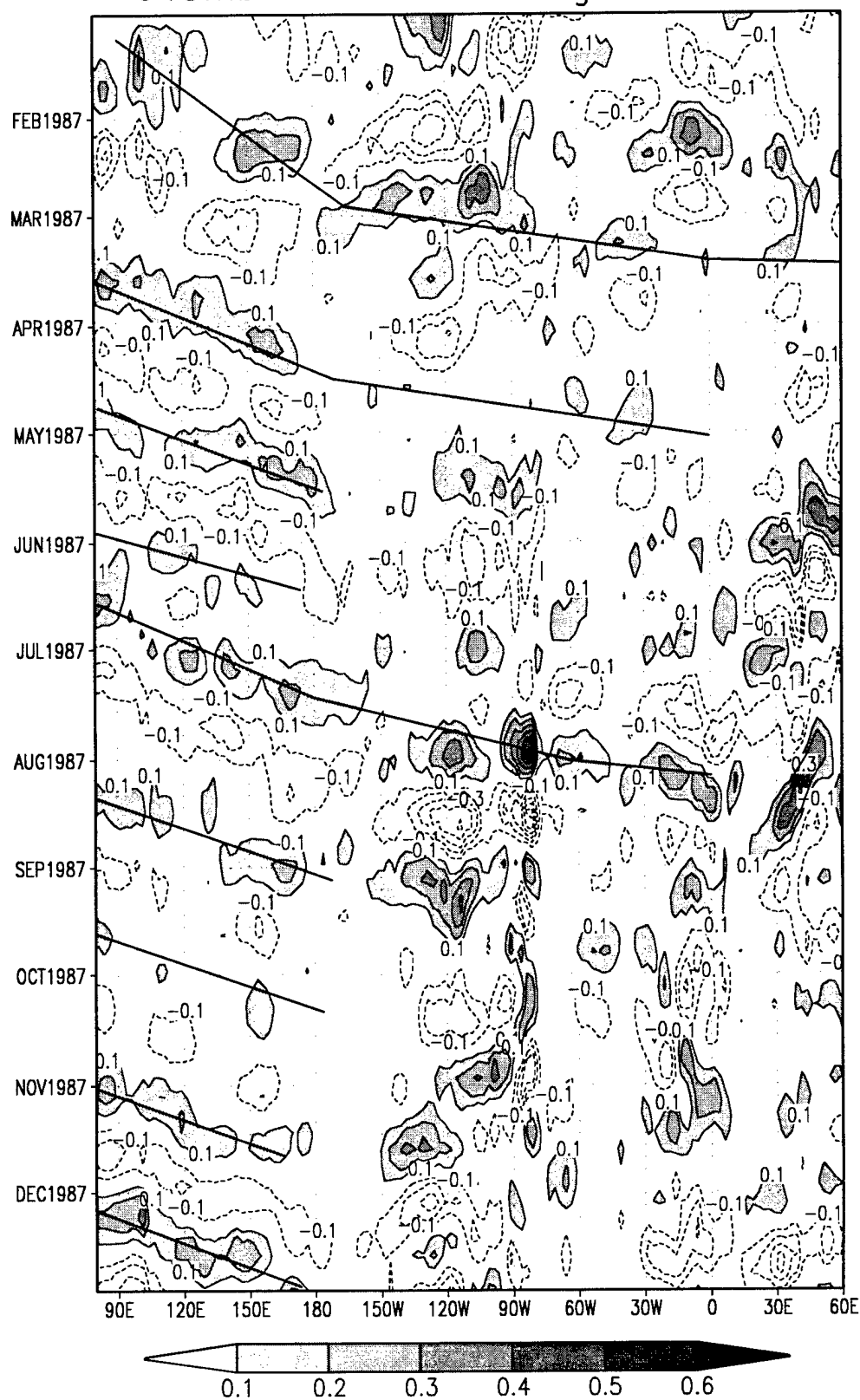
year at 648 mb. This level was selected because it shows the maximum response to IO-propagation. Anomalies are calculated relative to the nonfiltered state so that positive (negative) contours refer to heating rates warmer (colder) than the nonfiltered state, which is of course always negative. Thick, solid lines indicate a subjectively-located position of the IO as indicated by filtered-OLR (see Fig. 2.1). Notice that positive anomalies occur along the convective centers associated with IO-propagation due to suppression of radiative cooling at the wave front. In addition, for the events of January-March and August-September there are negative anomaly centers in the Eastern Pacific Ocean (~120°W) contemporaneous or preceding IO-passage and possibly associated with subsidence in an enhanced Walker circulation. Correlation analysis to be presented later will quantify the extent that such relationships hold for a longer data base.

CHAPTER 4

NORMAL MODES ANALYSIS

4.1 Introduction

It has been almost three decades since Matsuno (1966) first described the characteristics of quasi-horizontal wave motions in the equatorial area. His linearized analysis was based on a single-layer primitive-equation model on a beta plane centered at the equator. This analysis revealed the existence of two basic equatorial modes: the mixed Rossby-gravity mode and the Kelvin mode. Atmospheric numerical models that use spherical harmonics to solve the nondivergent vorticity equation are based on scaling arguments applicable to mid-latitudes where divergent circulations are relatively small. However, extrapolation of this technique into the tropics has not been very successful mainly because divergent circulations associated with deep tropical convection are significant there. Furthermore, since divergence seems to be important in the motion of low frequency ultralong waves (like the IO) it is probably more appropriate to use linearized primitive-equation than the nondivergent vorticity equation (Kasahara 1976).

Kasahara and Puri (1981) developed eigensolutions (normal modes) for free oscillations of a linearized primitive-equation model, extending Matsuno's (1966) analysis to spherical coordinates. These solutions are obtained for both vertical and horizontal structure equations. The horizontal structure is described by a spherical

harmonics function which is explicitly related to the vertical structure through equivalent depth. An important property of the horizontal function is that it is orthogonal, thus allowing for simultaneous decomposition of wind and height fields into individual wave modes (Kasahara 1984). In the present research, it is desirable to use the normal mode technique to isolate wave modes as represented by wind and height fields thus allowing identification of the mode of oscillation which represents the bulk of IO-variations in equatorial latitudes.

4.2 Method of Solution

In order to model the essential features of tropical ultralong waves, a method of producing eigensolutions (normal modes) for a system of primitive equations is used as developed by Kasahara and Puri (1981). The basic state atmosphere is assumed to be at rest with temperature varying only with height. Next, the linearized horizontal equations of motion over a sphere can be written as:

$$
\left.
\begin{aligned}
&\frac{\partial u'}{\partial t} - 2\Omega v' \sin\phi = -\frac{1}{a\cos\phi}\frac{\partial}{\partial \lambda}\left[gz + RT_0(\sigma)\ln(p_s)\right]', \\
&\frac{\partial v'}{\partial t} + 2\Omega u' \sin\phi = -\frac{\partial}{a\partial \phi}\left[gz + RT_0(\sigma)\ln(p_s)\right]', \\
&\frac{\partial}{\partial t}\left\langle\frac{\partial}{\partial \sigma}\left\{\frac{\sigma}{R\Gamma_0}\frac{\partial}{\partial \sigma}\left[gz + RT_0(\sigma)\ln(p_s)\right]'\right\}\right\rangle - \nabla\cdot\mathbf{V}' = 0,
\end{aligned}
\right\}
\tag{4.1}
$$

where primed quantities represent small perturbations on the atmospheric basic state. Also, $\sigma = p/p_s$; p_s is surface pressure; u' and v' are the zonal and meridional perturbation wind components; $\mathbf{V}'=(u',v')$; Ω, a, g are earth's angular velocity, radius, and

acceleration of gravity respectively; T_0 and Γ_0 are basic-state temperature and lapse-rate respectively; λ is longitude; ϕ is latitude; R is the gas constant; and t is time. Equation (4.1) is then solved via separation of variables assuming:

$$\left.\begin{aligned} u' &= \overline{u}\,\Psi(\sigma), \\ v' &= \overline{v}\,\Psi(\sigma), \\ \left[gz + RT_0(\sigma)\ln(p_s)\right]' &= g\overline{h}\,\Psi(\sigma), \end{aligned}\right\} \tag{4.2}$$

which is vertically coupled by the vertical dependence function, $\Psi(\sigma)$. In addition, the overbar denotes the horizontal- and time-varying part of the solutions. Also notice that h represents the pseudo height field, which is given by

$$h = z + \frac{R\Delta T}{g}, \tag{4.3}$$

and $\Delta T = T(z) - T(\sigma)$. Inserting Eq. (4.2) into Eq. (4.1) one obtains:

$$\left.\begin{aligned} \frac{\partial \overline{u}}{\partial t} - 2\Omega\overline{v}\sin\phi &= -\frac{g}{a\cos\phi}\frac{\partial \overline{h}}{\partial \lambda}, \\ \frac{\partial \overline{v}}{\partial t} + 2\Omega\overline{u}\sin\phi &= -\frac{g}{a}\frac{\partial \overline{h}}{\partial \phi}, \\ \frac{\partial \overline{h}}{\partial t} + D\nabla\cdot\overline{V} &= 0. \end{aligned}\right\} \tag{4.4}$$

Here D is a separation constant and is commonly referred to as equivalent depth. This horizontal system is known as Laplace's tidal equations or simply the shallow water equations over a sphere. Additionally, Eq. (4.4) is related to the vertical structure through

$\Psi(\sigma)$ and must satisfy the relationship

$$\frac{d}{d\sigma}\left(\frac{\sigma g}{R\,\Gamma_0}\frac{d\Psi(\sigma)}{d\sigma}\right)+\frac{1}{D}\Psi(\sigma)=0. \tag{4.5}$$

Now, the solution to Eq. (4.4) and Eq. (4.5) can be given by a system of vertically coupled Hough spherical harmonics such that

$$\left(\bar{u},\bar{v},\bar{h}\right)^{T}=\mathbf{S}_{n}\mathrm{H}_{r}^{s}(\lambda,\phi\,;n)\exp\!\left(-i\sigma_{r}^{s}t\right), \tag{4.6}$$

where T signifies transpose, n the vertical mode index, r the meridional index, s the zonal wave number, and $\mathbf{S}_n$ a scaling matrix given by:

$$\mathbf{S}_{n}=\begin{pmatrix}(gD_{n})^{\frac{1}{2}} & 0 & 0 \\ 0 & (gD_{n})^{\frac{1}{2}} & 0 \\ 0 & 0 & D_{n}\end{pmatrix}. \tag{4.7}$$

The Hough spherical harmonics function $[\,\mathrm{H}_{r}^{s}(\lambda,\,\phi;\,n)]$ is given by

$$\mathrm{H}_{r}^{s}(\lambda,\phi\,;n)=\mathcal{H}_{r}^{s}(\phi\,;n)\exp\,(is\lambda)=\begin{pmatrix}U_{r}^{s}(\phi\,;n) \\ -iV_{r}^{s}(\phi\,;n) \\ Z_{r}^{s}(\phi\,;n)\end{pmatrix}\exp\,(is\lambda), \tag{4.8}$$

and $\mathcal{H}_{r}^{s}$ is the meridional structure function. The solution to this equation can be obtained by a series of associated Legendre polynomials. Finally, the three-dimensional normal mode representation is satisfied by solving one horizontal eigenvalue problem for each equivalent depth.

4.3 Properties of Normal Mode Solutions

In general, there are two types of solutions to the Laplace tidal equations [Eq. (4.3)], which are classified by frequency. These include either high-frequency inertia-gravity waves or low-frequency rotational-Rossby waves. However, for the lowest wave number near the equator, a third type exists which is called the mixed-Rossby-gravity wave and it exhibits properties of both wave types (Matsuno 1966). In addition, for free gravity waves there exists an eastward propagating solution for the lowest wave number in which meridional velocities are zero and zonal velocities maximize at the equator. This mode is known as the Kelvin wave. Geisler and Stevens (1982), Anderson and Stevens (1987), and others have extended Gill's (1980) linearized shallow water model to show that the essential features of IO-propagation can be attributed to a combination of mixed-Rossby gravity- and Kelvin-waves generated by a fixed heating source over Indonesia. Furthermore, outside of the source region, the Kelvin solution becomes the dominant contributing component.

The horizontal structure equation given by Eq. (4.8) is a function of meridional index (r) and this allows isolation of particular modes such as the Kelvin mode, which is particularly relevant to our discussion. In addition, vertical structure functions are selected so that Kelvin mode dynamics, which are principally contained within the upper troposphere (Gill 1980, Geisler and Stevens 1982), are well resolved. Figure 4.1 shows the vertical structures 1-3 (a) and 4-6 (b). These structures are the solutions to Eq. (4.5) for each equivalent depth chosen (vertical mode) and are analogous to divergence, where zero-crossings represent the levels of nondivergence. Vertical mode one (equivalent

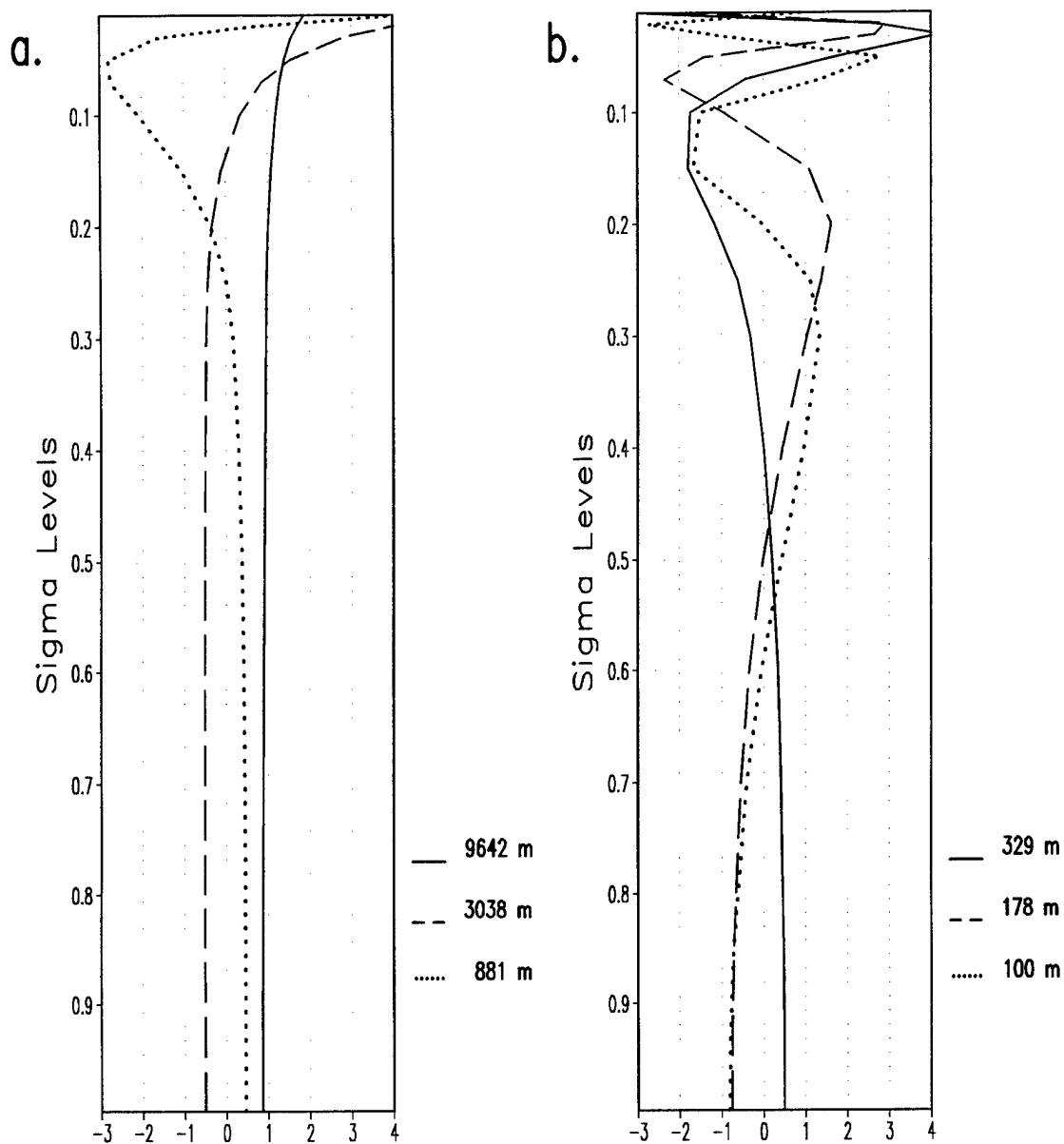# Normal Mode Vertical Structure Functions

FIG. 4. 1 Vertical structure functions for modes 1-3 (a) and 4-6 (b) used in this normal

mode analysis. Associated equivalent depth is given (in meters) to the right of each

figure and modes are ordered in terms of decreasing equivalent depth.

depth, 9642 m) is divergent throughout the atmosphere and is known as the barotropic mode or external mode, additional modes are known as baroclinic or internal modes. Notice that for each successive internal mode, there is one additional zero-crossing. Also note that the maximum upper tropospheric responses, where Kelvin mode dynamics are most prominent, are found in mode four, five, and -six (σ =~0.13, etc.).

4.4 Processing

4.4.1 NCEP/NCAR Reanalysis Data

Normal mode Kelvin solutions were derived from wind and height fields obtained from the 17-level 2.5° NCEP/NCAR Reanalysis database. This analysis is processed to be temporally consistent with that used for the radiative analysis described in Chapter 3. In addition, since more data were available from this database than for the ISCCP database, the period of calculations was extended to include the interval from January 1985 through December 1993.

The first step in processing was to average data into pentads which were concurrent with those used for radiative calculations. Next, fields were converted to a 17-level sigma coordinate system and interpolated onto a global spherical grid with a horizontal resolution of 32 points in longitude and 40 Gaussian points in latitude. Thus, the horizontal grid provides a resolution of approximately 11.25° X 4.41° which offers adequate spacing to resolve large-scale tropical modes associated with the IO.

4.4.2 Numerical Procedure

The numerical procedure used to produce normal mode solutions as described by Kasahara and Puri (1981) is now discussed. First, the vertical structure function [$\Phi_n(k)$]

for each equivalent depth vertical mode (n) as a function of discrete sigma level (k) can be expressed in finite-difference form as

$$\Phi_n(k) = \Psi_n(k)\left[\frac{(\Delta\sigma_k + \Delta\sigma_{k+1})}{2}\right]^{\frac{1}{2}}. \qquad (4.9)$$

This approximation is then expressed as an orthogonal matrix eigenvector problem so that vertical structure solutions for all n are obtained. Second, three-dimensional wind and height fields are expanded onto an input data vector which is defined by

$$X^i(\lambda,\phi,k) = (u^i,v^i,z^i_{pseudo})^T = \sum_{k=1}^{17} S_n X_n(\lambda,\phi)\Phi_n(k), \qquad (4.10)$$

where

$$\left.\begin{array}{l} z^i_{pseudo} = z^i + \dfrac{RT_0(\sigma)}{g}\ln\!\left(\dfrac{p_s}{p_0}\right) \\[2em] X_n(\lambda,\phi) = S_n^{-1}\displaystyle\sum_{k=1}^{17} X^i(\lambda,\phi,k)\Phi_n(k). \end{array}\right\} \qquad (4.11)$$

The superscript (i) refers to input field variable, p_0 a 1000-mb normalization level, and S_n^{-1} to the inverse of S_n, which is defined by Eq. (4.6). Third, the input vector vertical transform $[X_n(\lambda,\phi)]$ is used in combination with the Hough spherical harmonics function [Eq. (4.7)] to save wave coefficients as a function of wavenumber (s) and meridional index (r). These wave coefficients $[X_r^s(n)]$ are calculated for each vertical mode (n) such that

$$X_r^s(n) = \sum_{\lambda=0}^{2\pi} \sum_{\phi=-\pi/2}^{\pi/2} X_n(\lambda, \phi) \left[H_r^s(\lambda, \phi; n) \right]^*, \qquad (4.12)$$

where the superscript * denotes the complex conjugate operator. Fourth, the zonal and meridional wind and geopotential fields for the Kelvin mode (represented by meridional structure r=1) are reconstructed onto the 32 X 40 grid point truncated grid previously discussed. This reconstruction is accomplished by summing contributions from wave numbers 1-10 from 17 sigma levels for the vertical modes specified so that

$$X_m(\lambda, \phi, n) = \sum_{k=1}^{17} \sum_{s=1}^{10} S_n X_{r=1}^s(\lambda, \phi, n) \Phi_n(k). \qquad (4.13)$$

There is one horizontal eigenvalue problem to solve for each equivalent depth. Kelvin wind solutions are obtained for individual internal modes 2-6 (see Fig. 4.1) as well as for total Kelvin wind reconstruction represented by contributions from all five of these internal vertical modes.

4.5 Isolating Intraseasonal Oscillation Signatures by Filtering Normal Mode Calculations

A spectral filter is applied to calculated results in order to identify the Kelvin mode variations associated with the IO. This filter is processed in the same way as that used for the radiative calculations so that correlations between like-filtered datasets can be performed (described in Chapter 5). That is, Kelvin winds that do not fall within the spectral range of 25-80 days (5-16 pentads) are removed. Magnitudes of filtered Kelvin winds are generally between ½ and ¼ of the unfiltered Kelvin wind magnitudes.

4.6 Results

Filtered Kelvin mode output has been saved for seven sigma levels[6] which adequately described the vertically truncated Kelvin modes. In general, the largest reconstructed Kelvin mode response (n=2-6) occurred at the 0.2 σ-level. Figure 4.2 shows a Hovmöller diagram of individual vertical-mode filtered Kelvin U wind responses at the 0.2 σ level for the 1987 "El Niño" year. The two largest responses occurred at vertical mode n=4 (a) and vertical mode n=5 (b). Figure 4.3 shows the much smaller responses at vertical modes n=3 (a) and n=6 (b). Note the plot scales are different for these two figures. The n=2 response is negligibly small and is not plotted here. These results are a direct result of the vertical structures shown in Fig. 4.1. For example, as expected from Fig. 4.1, the n=4 mode shows its largest tropospheric response at the 0.15 σ-level whereas the n=6 mode shows its largest tropospheric response at both the σ=0.15 and σ=0.30 levels. However, as previously mentioned, the maximum total Kelvin U response (reconstruction of modes n=2-6) occurs at 0.2 σ. Note that unlike the convective-cloud-related anomalous-OLR diagram shown in Fig. 2.1, the anomalous-Kelvin U response is apparent at all longitudes (although stronger in convective source regions). In addition, the position of the IO as indicated by OLR signals of Fig. 2.1 matches up well with a line bisecting the positive anomalous Kelvin U (dark-colored shading) and that of the negative anomalous Kelvin U (light-colored shading). This validates the use of the NCEP/NCAR Reanalysis wind and height fields as input to the normal mode analysis. This database must capture the essential features of the atmosphere. Finally, the breakdown of

---

[6] These saved levels include 0.925, 0.85, 0.7, 0.3, 0.25, 0.2, and 0.15 σ.

1987 Anomalous Kelvin Wind

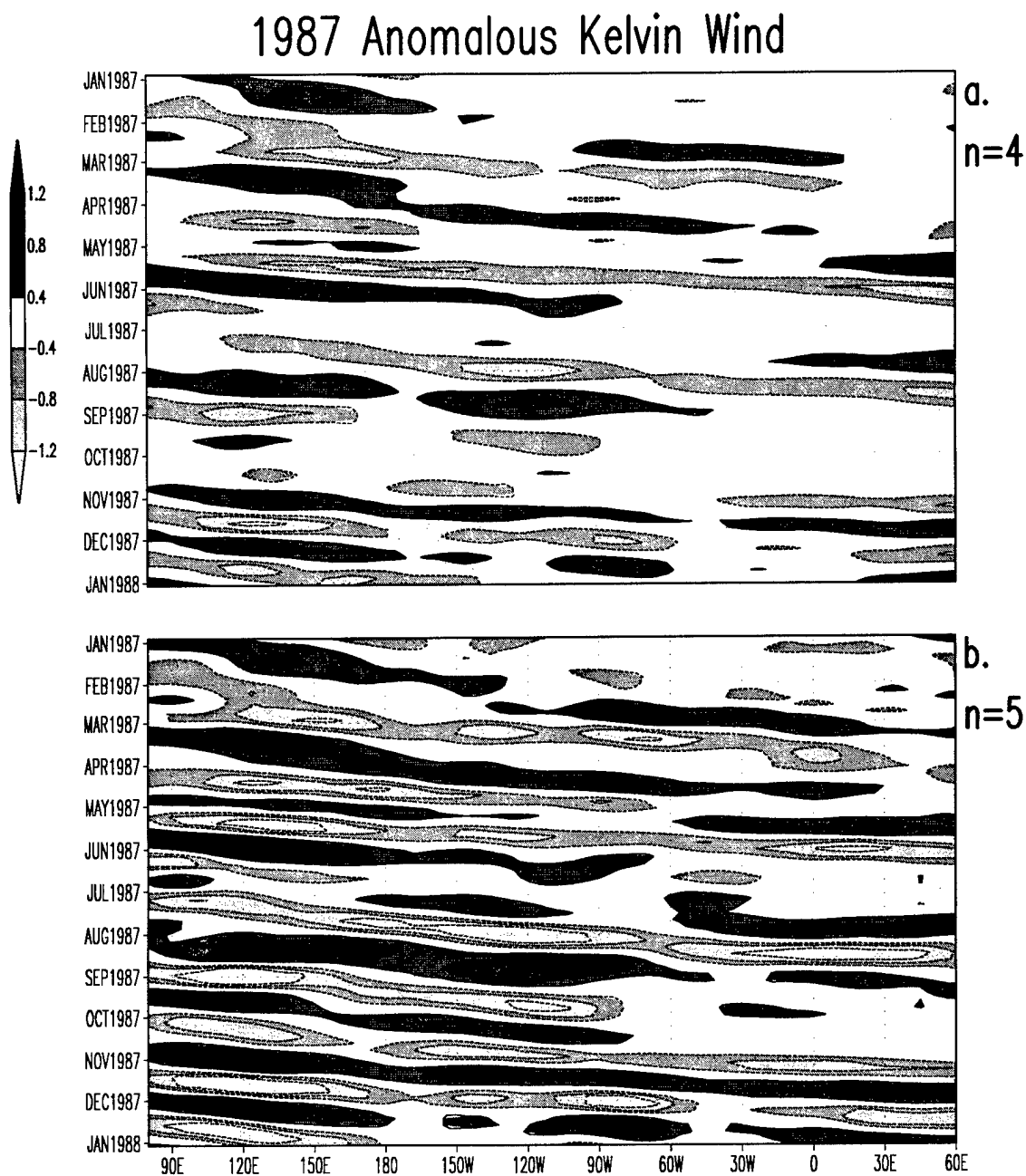FIG. 4. 2   1987 Anomalous Kelvin wind (U) for (a) vertical mode n=4 and (b) n=5.

Contour interval is 0.2 m s^{-1} with greater than $|\pm0.4|$ shaded as indicated by the shade key.

1987 Anomalous Kelvin Wind

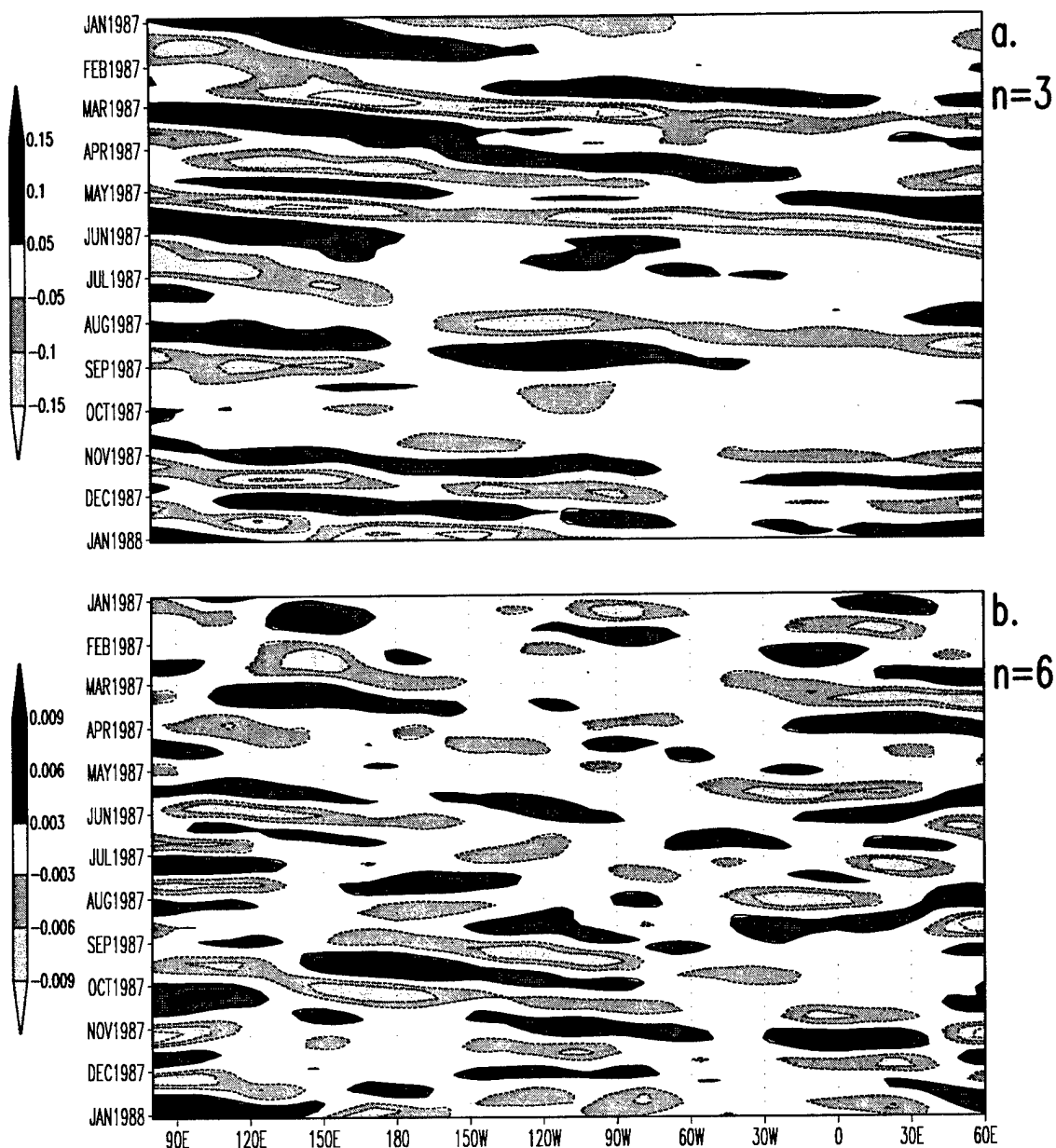FIG. 4. 3 Anomalous Kelvin wind (U) for (a) vertical mode n=3 and (b) n=6. Contour

interval for (a) is 0.05 m s^{-1} and for (b) is 0.003 m s^{-1} with shading as indicated by the

shade key.

anomalous Kelvin U (light-colored shading). This validates the use of the NCEP/NCAR Reanalysis wind and height fields as input to the normal mode analysis. This database must capture the essential features of the atmosphere. Finally, the breakdown of anomalous-Kelvin U for the 1987 period just discussed is applicable to all periods calculated (1985- 1993) except that the number and magnitude of IO events in those non-El Niño years is generally smaller.

In order to demonstrate the relative importance of the anomalous Kelvin U response in relation to the Kelvin U field, variances for these parameters were calculated based on the 649 pentads within the 1985-1993 period.[7] Figure 4.4 shows the variance of total reconstructed (n=2-6) filtered Kelvin U (a) and unfiltered Kelvin U (b). Panel (c) shows the ratio of average (a) and average (b) computed between 10°S and 10°N. As can be seen from panel (c) there is a great deal of longitudinal variability to the anomalous Kelvin contribution to the total Kelvin wind. The greatest contribution occurs over the convective source regions maximizing at about 105°E. There are two regions of relatively high contributions in the Eastern Pacific Ocean, the larger maximizing at about 135°W and a smaller maximizing along the South American West Coast at 80°W. In addition to these, there are peaks over Africa (20°E) and in the Indian Ocean (~60°E).[8] It appears from this figure that anomalous Kelvin winds (Fig. 4.4.a) make up a significant portion of the total variability (Fig 4.4.b) within the upward and downward cells of the Walker circulation.

---

[7] Actually there are 657 pentads in this 9-year period. However, the spectral filter discussed in subsection 5 is unstable for approximately the first and last four pentads. Therefore, statistics exclude these pentads.

[8] Longitudinal scale of these plots is picked to emphasize the Pacific Ocean.

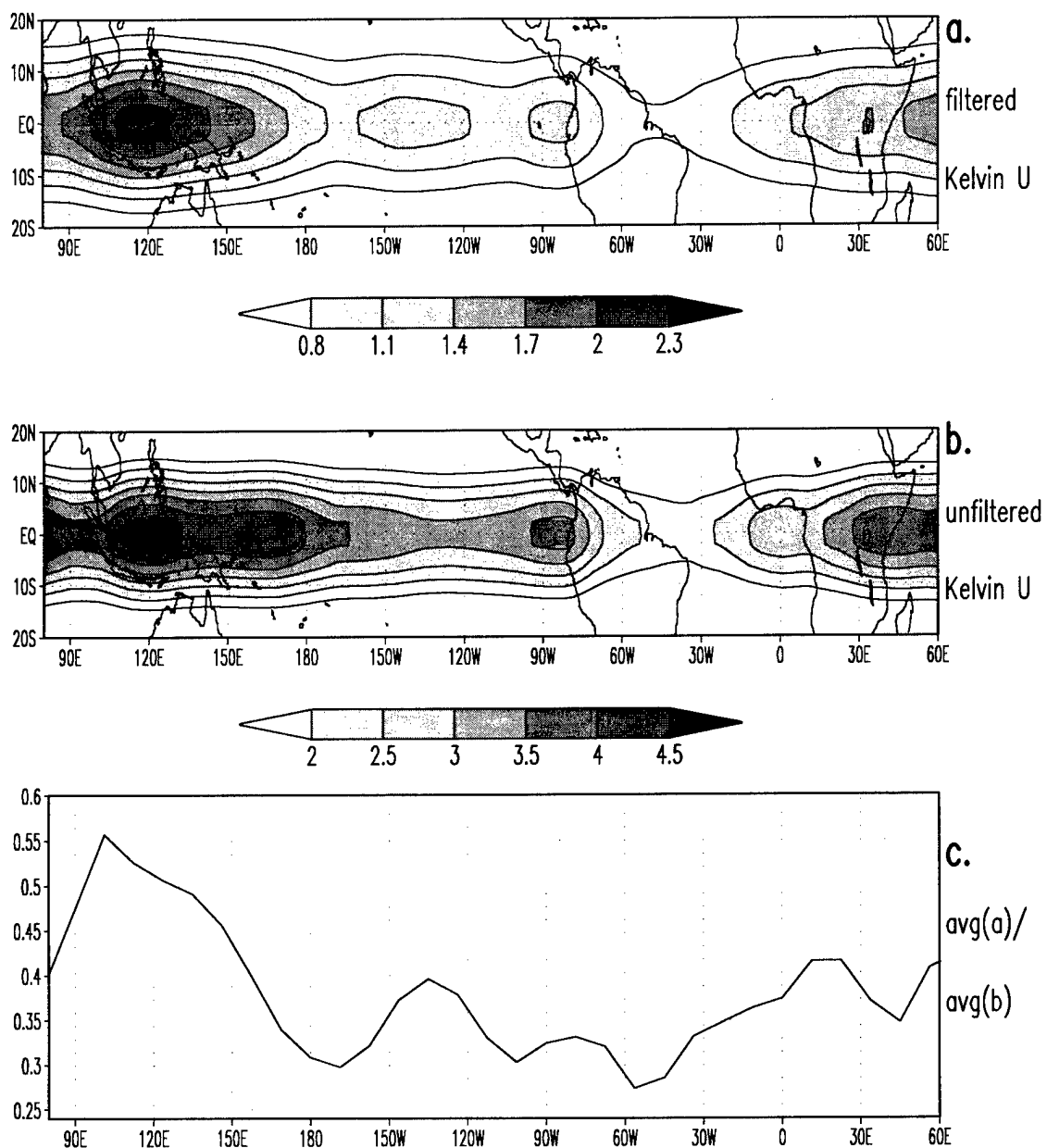# Variance of Filtered Kelvin U and Unfiltered Kelvin U

FIG. 4. 4 Variance of (a) filtered Kelvin U and (b) unfiltered Kelvin U. Contours are indicated by shade key located beneath each figure with units of m s^{-1}. Panel (c) is the ratio of average (a) and (b) computed between latitudes 10°S and 10°N.

As discussed in Chapters 2 and 4 (subsection 1), convectively driven divergent circulations are the impetus to Kelvin wave generation. Figure 4.5 shows a variance comparison similar to that of Fig. 4.4 except that total Kelvin U is compared to filtered divergent U. The divergent wind is computed from the Helmholtz theorem, which states that any velocity field can be divided into divergent $\mathbf{V}_\chi$ and nondivergent $\mathbf{V}_\psi$ components so that

$$\mathbf{V} = \mathbf{V}_\psi + \mathbf{V}_\chi, \tag{4.13}$$

and

$$\begin{aligned} \mathbf{V}_\psi &= \mathbf{k} \times \nabla \psi, \\ \mathbf{V}_\chi &= -\nabla \chi. \end{aligned} \tag{4.14}$$

Here ψ is the stream function and χ is the velocity potential defined in terms or rotational/nondivergent (r) and nonrotational/divergent (d) components as

$$\begin{aligned} u_r &= -\frac{\partial \psi}{\partial y}, & v_r &= \frac{\partial \psi}{\partial x}, \\ u_d &= \frac{\partial \chi}{\partial x}, & v_d &= \frac{\partial \chi}{\partial y}. \end{aligned} \tag{4.15}$$

Figure 4.5 (a) shows the U-component of the divergent wind while (b) is the unfiltered Kelvin U. Note that while (b) is the same plot as Fig. 4.4 (b), it has been interpolated to a 129 point longitudinal grid used for Fig. 4.4 (a) so that comparisons can be made. This produces the jagged appearance of both (b) and (c). Also notice that there is a scale

Variance of Filtered Divergent U and Unfiltered Kelvin U
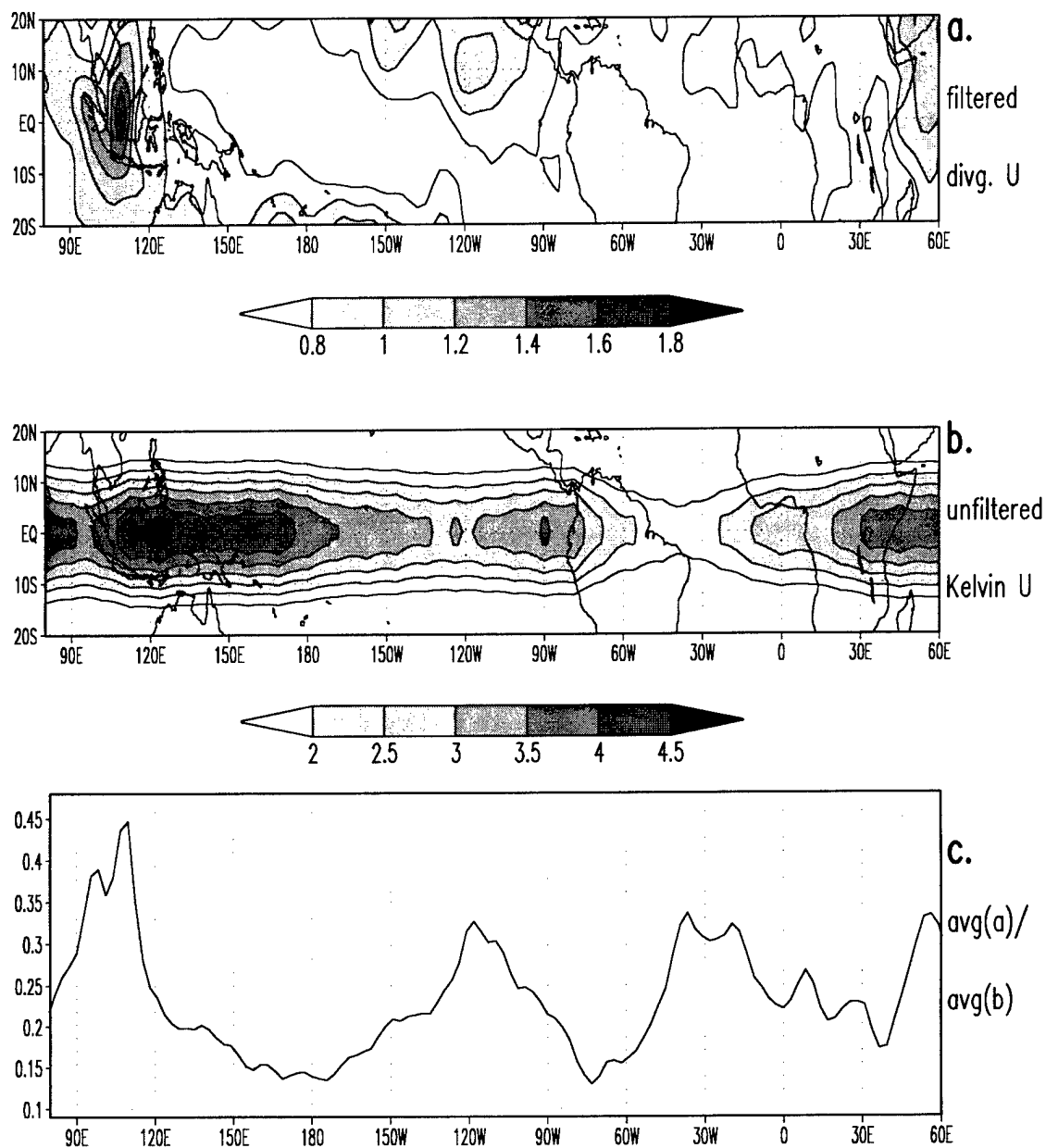

FIG. 4. 5 Variance of filtered divergent U and unfiltered Kelvin U.

difference between Fig. 4.4 (c) and Fig. 4.5 (c). As with the previous figure, Fig. 4.5 (c) shows a great deal of longitudinal variability in the contribution of anomalous divergent U in relation to total Kelvin U. There is even a high degree of similarity as to the positions of these contributions. Again, the maximum contribution occurs at the convective source region around 110°E and there is an Eastern Pacific Ocean maximum at 120°W both of which seem to be associated with the Walker circulation. However, the structure and position of these contributions are somewhat different, especially with regards to the location of the single maximum in the Eastern Pacific Ocean (120°W) and the maximum in the Eastern Atlantic Ocean (40°W). These differences can probably be attributed to the fact that unlike anomalous Kelvin U, which only has a U-component, anomalous divergent U depicts only the zonal contributions to the anomalous divergent circulation. The mass-wind balance reflected in the Kelvin mode corresponds to that of a free gravity wave in the x-direction and reflects geostrophic balance in the meridional direction. In contrast, there is no mass-wind constraint in the divergent wind, which directly results from mass-continuity.

In order to characterize the relationship between anomalous Kelvin U and anomalous radiative heating a composite winter-season case has been created from calculated data previously discussed. This discussion serves as a lead-in to the statistical correlations described in the next chapter. Figure 4.6 (a) shows the average of strong winter-season positive-phase IO events at the 0.2 σ-level that occurred during the period of this study. Strong cases are defined as those exceeding ± 1sd, where sd refers to standard deviation. Positive-phase and negative-phase (not shown) refer to + 1sd and - 1sd composites

Composite Positive-Phase Winter-Season Anomalous Kelvin U
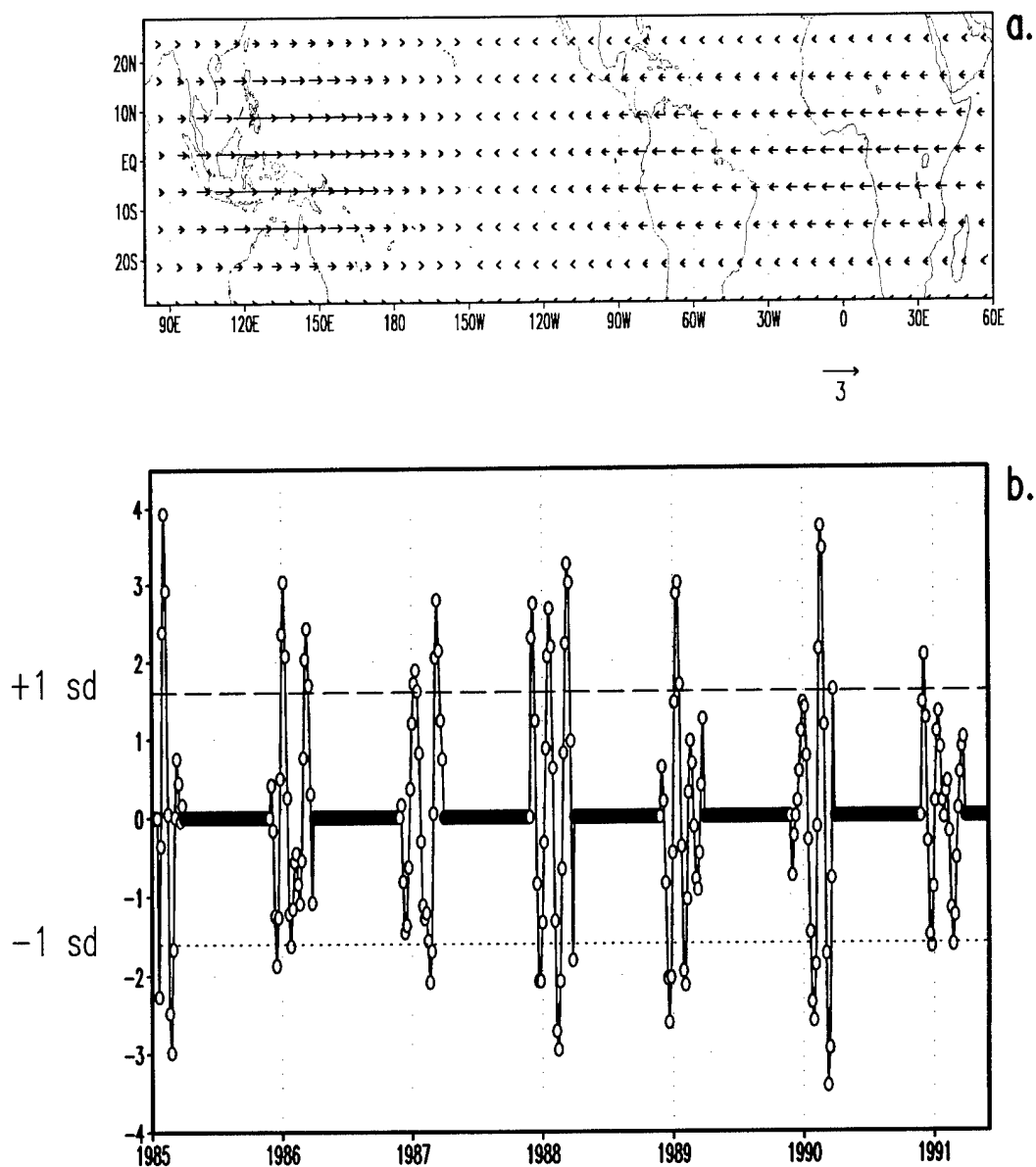

FIG. 4. 6 Positive-phase winter-season composite of anomalous Kelvin U (a) in units of

m s^{-1}. Panel (b) shows winter time cases with ± 1 standard deviation indicated by dashed

and dotted lines respectively.

respectively. Figure 4.6 (b) shows all winter-season pentads (defined as January-February-March) with + 1sd and - 1sd cases falling above and below the horizontal dashed and dotted lines. This positive-phase composite (a) shows the positive anomalous Kelvin U pulse over Indonesia and the Western Pacific Ocean indicating that the convective center is located in the Indian Ocean for this composite time (t=0). Note the anomalous overturning circulation implied by this pulse. In addition to this eastward anomalous pulse there is an anomalous westward pulse to the east of 100°W feeding into the convergent region of the west-central Pacific Ocean (140°W).

The composite lag-lead evolution of both anomalous Kelvin U (fku) and anomalous radiative heating (fdt) is shown in Fig. 4.7 (a-h). Lag and lead times are at pentad intervals so that for example t=-1 refers to the pentad composite preceding that shown by Fig. 4.6 (a), t=0 the same period as Fig. 4.6 (a), t=+1 the pentad composite after t=0 and so on. Several points regarding the evolution of fdt and fku can be inferred from this figure. One, the positive fku-pulse develops in response to convection (implied by positive fdt indicated by dark-colored shading). There is a positive outflow just ahead of the convective region in the Western Pacific Ocean (panels a-d). However, as convection stalls and dies off over the Central Pacific Ocean (panels e-h) anomalous Kelvin winds detach themselves from this convective-drag and propagate quickly eastward. Two, anomalous sinking motions (implied by negative fdt indicated by light-colored shading) which lie adjacent to anomalous heating centers precede these convective centers in the Western Pacific Ocean (Fig. 4.7 a-d) and decrease in magnitude with eastward IO propagation. In addition, as these convective centers approach the Central Pacific Ocean

FIG. 4.7 Comparison of anomalous Kelvin U (fku, in units of m s^{-1}) and anomalous radiative cooling (fdt, in units of K day^{-1}) for wintertime positive-phase case at periods between composite minus one pentad (a. t=-1) through composite plus six pentads (h. t=+6). Anomalous radiative heating rate intervals are given by the shade key to the left of each diagram.

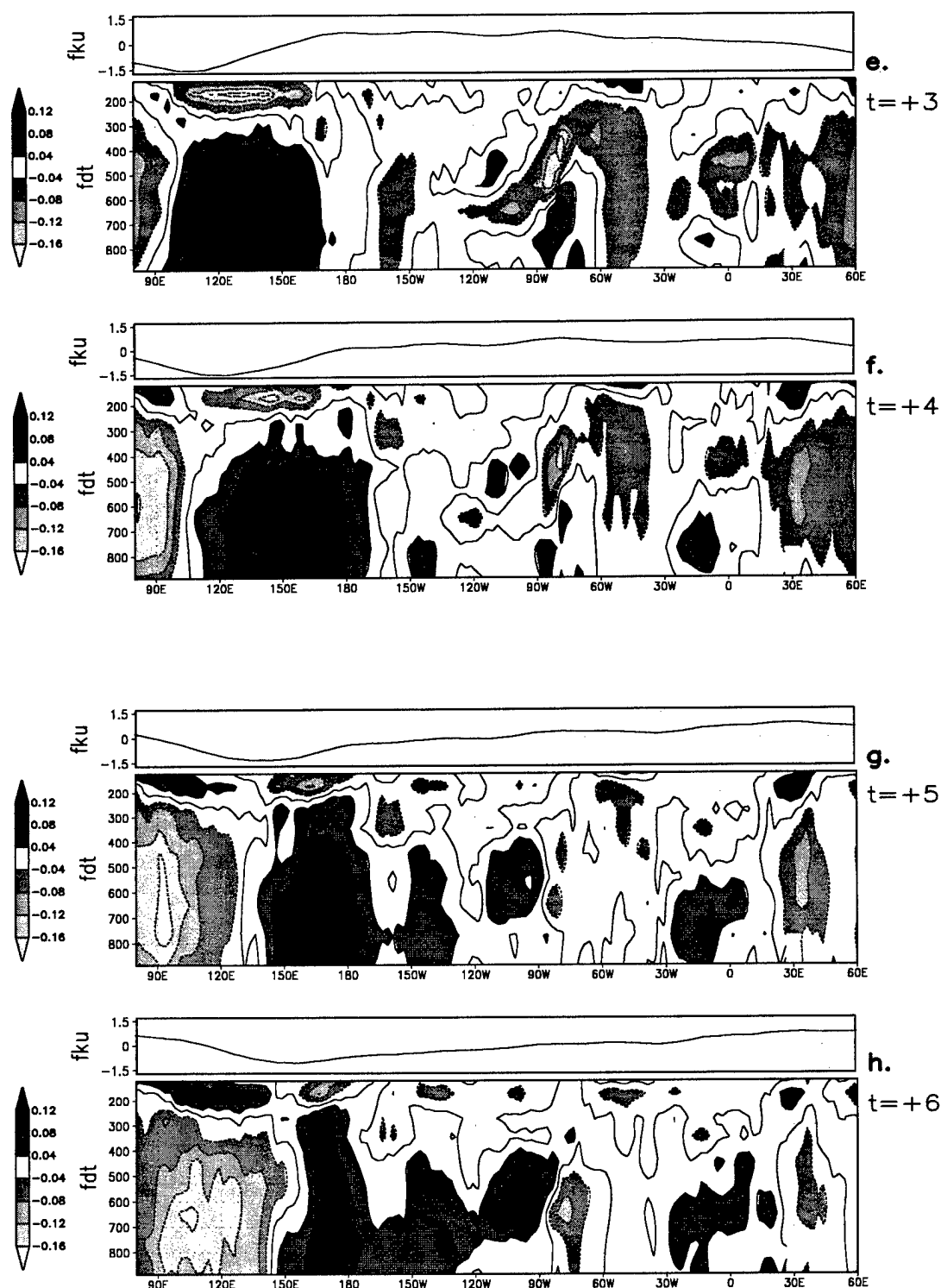Anomalous Composite Kelvin U and Radiative Heating
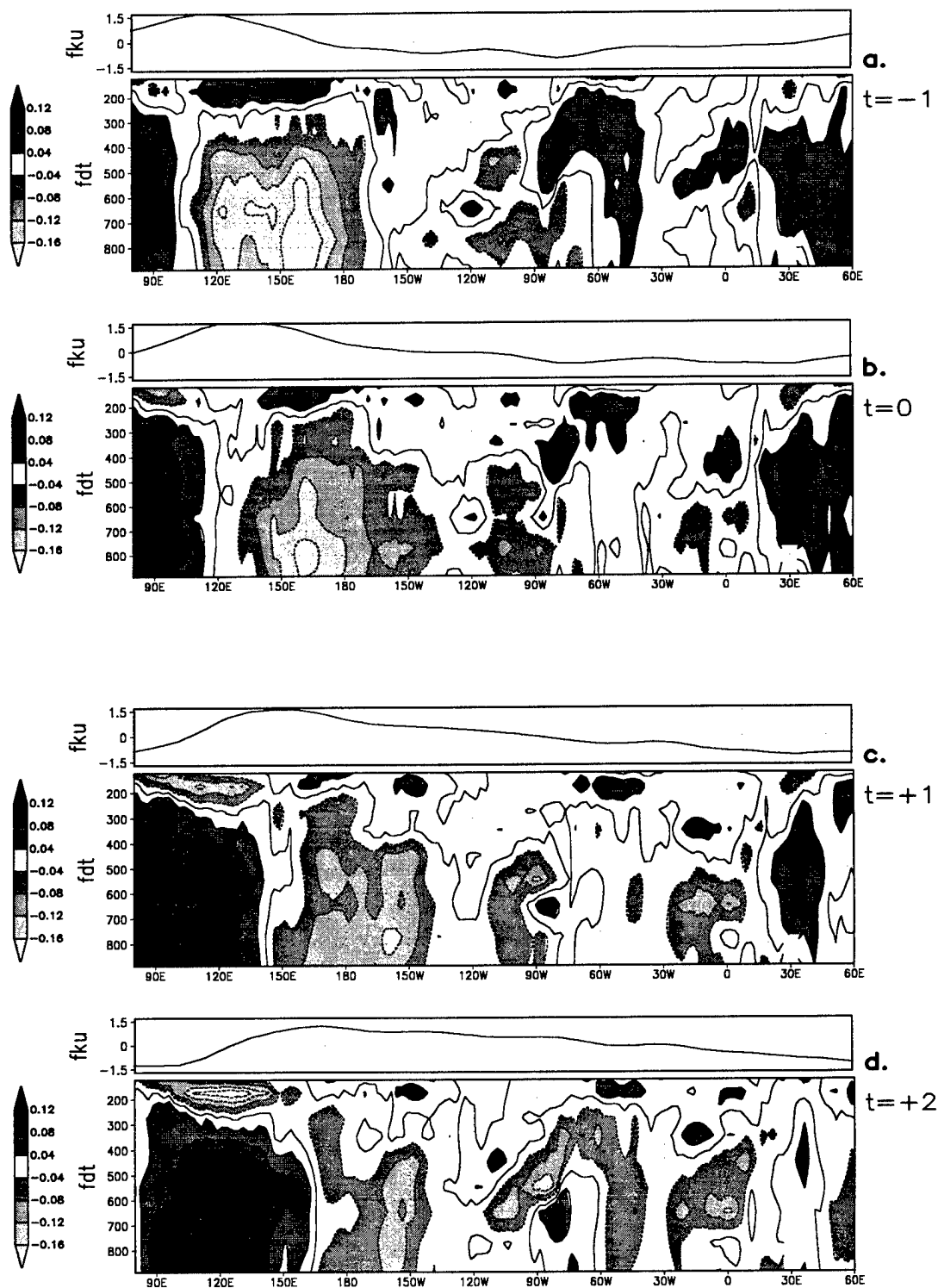
FIG. 4. 7 (Continued)

(Fig. 4.7 e-h) the anomalous sinking motion centers which had preceded convection die off completely and mass balance seems to be maintained by sinking motion behind (westward) of dissipating convection centers. These centers are likely associated with the advance of the next IO wave. Three, radiative cooling anomalies in the Eastern Pacific Ocean are sensitive to the IO phase. As long as the IO (indicated by the advance of the positive fku-pulse) lies to the west of this region (panels a-e) there is a somewhat fixed region of anomalous radiative cooling at about 110°W (assumably associated with the downward branch of the Walker circulation). However, as the IO passes (panels e-h) this region becomes one of anomalous radiative heating, consistent with the more eastward location of the Kelvin pulse; with anomalous divergence (and thus anomalous rising motion) in its wake.

Obviously, there is a strong relationship between anomalous radiative heating and anomalous Kelvin U. This relationship is explored in more detail by the correlative analysis described in Chapter 5.

CHAPTER 5

COMPARISONS

5.1 Introduction

This chapter compares and attempts to characterize the relationship between IO-filtered radiative heating (fdt) in the Eastern Pacific Ocean and IO-filtered Kelvin zonal winds (fku) in the Western Pacific Ocean as described in Chapters 3 and 4. Hovmöller diagrams of fdt and fku were presented in Fig. 3.10 and Figs. 4.2-3. Clearly, both fields showed a significant IO-scale response. The question is then, how do these two fields compare to each other, and what is the nature of their relationship.

The theoretical dependence of the wind field on the diabatic heating field has already been discussed in Chapter 2, subsection 3, and can be used here to investigate wind forcing by radiative heating. Specifically, anomalous radiatively forced winds can be calculated by using the linearized dynamic equations as employed by Simmons (1982) and given by Eqs. (2.6) and (2.7) in terms of fdt-forcing (Q_r) to produce anomalous radiative winds (u_{rad} and v_{rad}). Recall that in the Eastern Pacific Ocean, radiative heating represents the bulk of total diabatic heating ($Q \approx Q_r$) so our discussion is most applicable to that region. Figure 5.1 shows calculated radiatively forced winds (u_{rad} and v_{rad}) using the same composite case criteria as described in the previous chapter, at time t=0, for the 500-mb level. Shaded values given in (a) depict the calculated $\partial/\partial x(u_{rad})$ field, which is
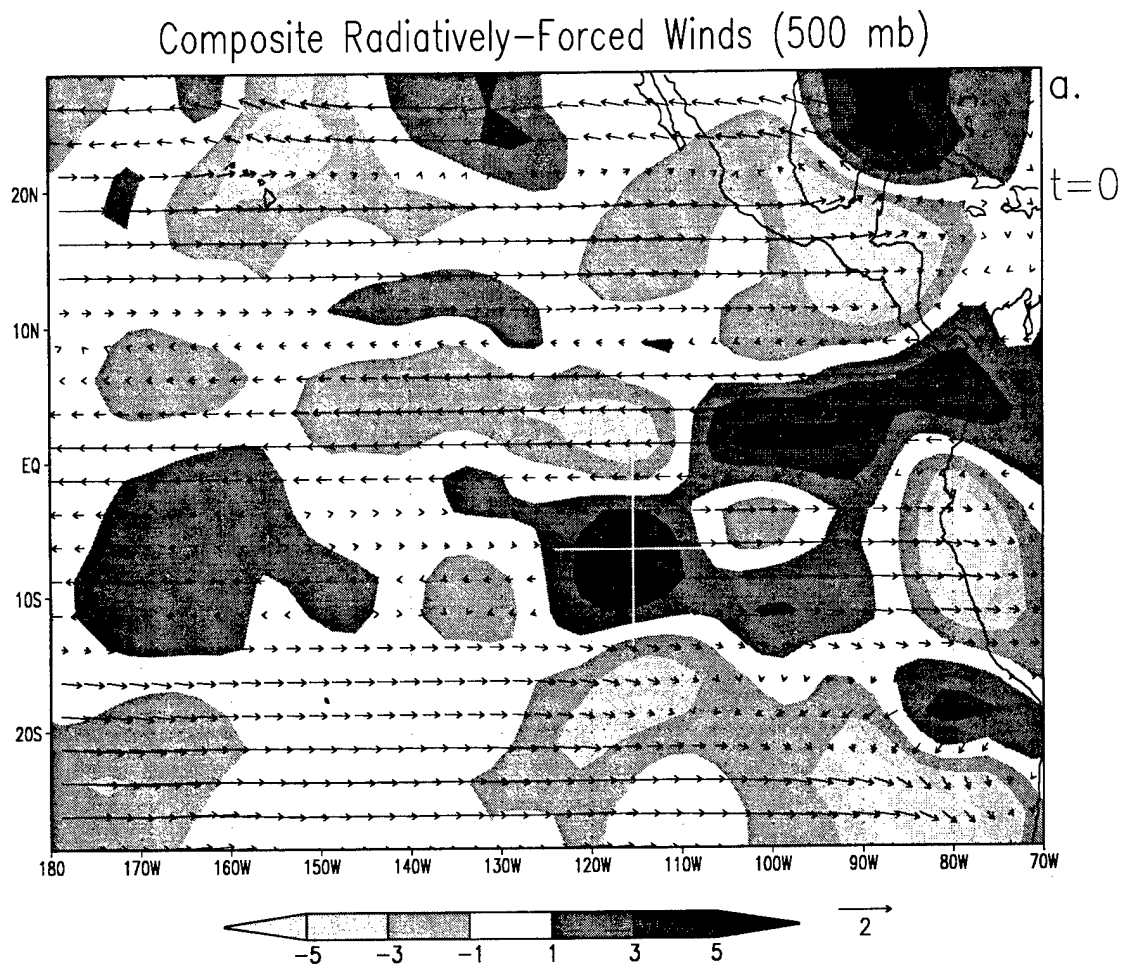
FIG. 5. 1 Radiatively-forced winds at 500 mb for composite time t=0. Shaded values are

$\partial/\partial x(u_{rad})$ in units of 10^{-7} s^{-1}. The vector radiatively forced wind field is given in m s^{-1}

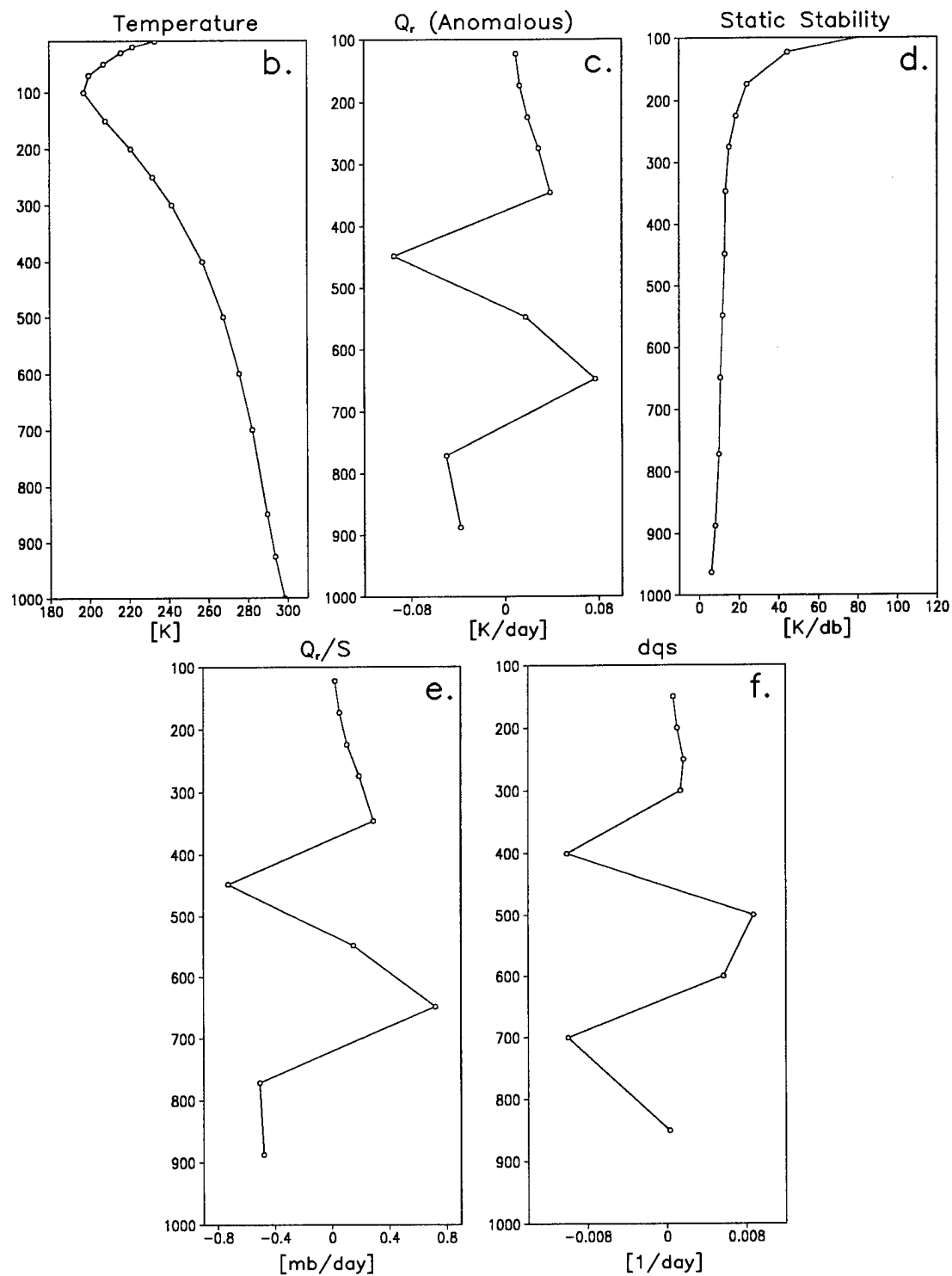with vector scale arrow given below panel (a). Units used in (b-f) are indicated below

each abscissa.

FIG. 5. 1 (Continued)

simply Eq. (2.7) times $(a \cos \phi)^{-1}$; and vectors give the calculated u_{rad}, v_{rad} vector wind field.[9] In order to demonstrate the evolution of these calculations, panels (b-f) show vertical profiles of individual calculation steps at a point described by the white cross-hairs shown in Fig. 5.1.a. Panel (b) shows the average tropical lapse-rate for the period of this study as derived from NCEP/NCAR Reanalysis monthly atmospheric temperature data averaged between 20°S and the equator. This temperature profile is then used to calculate static stability (S) as given by Eq. (2.5) and shown in Fig. 5.1d. Next, static stability was checked against values proposed by Gates (1961); producing substantial agreement; and then fixed for all calculations. Panel (c) shows the Q_r profile; (e) the Q_r/S profile; and (f) the $\partial/\partial p(Q_r/S)$ profile [$\partial/\partial p(Q_r/S)$ is labeled as dqs in the figure]. There are a number of points which can be drawn from this figure. First, the magnitude of the anomalous radiatively forced wind field (~ 1.0 m s^{-1}) is significant and is basically the same order of magnitude as that of the anomalous zonal Kelvin wind field (see fku in Fig. 4.7b). Second, as should be expected from the $\tan \phi$ term in Eq. (2.6); the meridional wind component is negligible; especially near the equator. Third, horizontal patterns of $\partial/\partial x(u_{rad})$ reflect horizontal variations of the $\partial/\partial p(Q_r/S)$ and its meridional gradient. Substantial time changes are noted in this gradient throughout the IO-composited event. Fourth, static stability (Fig. 5.1b) is nearly constant throughout the tropical troposphere. Therefore, Q_r/S (Fig. 5.1e) is basically just Q_r times a constant (S does not effect the vertical variation of dqs). Fifth, the vertical profile of dqs (Fig. 5.1f), a

---

[9] Note that u_{rad} is calculated by integrating backwards in longitude from 61.25°W to 178.75°W and that the fdt is assumed to be zero at 61.25°W. In addition, missing fdt values are interpolated.

derivative in pressure, mostly has the effect of shifting the Q_r/S profile vertically, and thus the most significant wind response is found not at the level of maximum heating, but in neighboring layers.

It was noted in Chapter 2.1 that IO-signatures are primarily found in negative anomalous OLR signatures (as a proxy for convection) and in upper level divergent wind anomalies. The former method is preferable in regions of convection because it is directly measured. However, in regions of nonconvection (like the Eastern Pacific Ocean) the later method is preferred because it relies only on the wind field. Therefore, upper-level anomalous divergent-winds should be a good indicator of anomalous rising or sinking motions associated with the IO in all regions (inferring overturning circulations). In addition, zonal divergence arising from $\partial/\partial p(Q_r/S)$ as produced from Eq. (2.7) should be a good measure of the anomalous radiative heating impact on the overall IO-circulation. Figure 5.2a-h shows the zonal radiative forced divergence [$\partial/\partial x(u_{rad})$ - Eq. (2.7) converted to Cartesian coordinates] as well as a graph of 200-mb zonal divergent winds [u_{div} - see Eq. (4.15)]. These figures were produced in the same way as Fig. 4.7. That is, meridional variations between 20°S and the equator are averaged to produce mean southern hemisphere positive-phase wintertime averages for each composite time. Note that negative values denote convergence and positive values denote divergence. However, the concept of u_{rad} breaks down in convective areas; generally west of 180°; where $(Q \neq Q_r)$. A point-by-point discussion of Fig. 5.2a-h follows:

a. Note that Kelvin winds (fku) shown in Fig. 4.7 are generally in phase with u_{div} although the former have a slightly higher magnitude. This difference in magnitude is

FIG. 5. 2 Anomalous composite u_{div} and $\partial/\partial x(u_{rad})$ for wintertime positive-phase case at periods between composite minus one pentad (a. t = -1) through composite plus six pentads (h. t = +6). Units are m s^{-1} for u_{div} and 10^{-7} s^{-1} for $\partial/\partial x(u_{rad})$. Values for $\partial/\partial x(u_{rad})$ are indicated by the shade key to the left of each diagram.

Anomalous Composite u_{div} and $d/dx(u_{rad})$
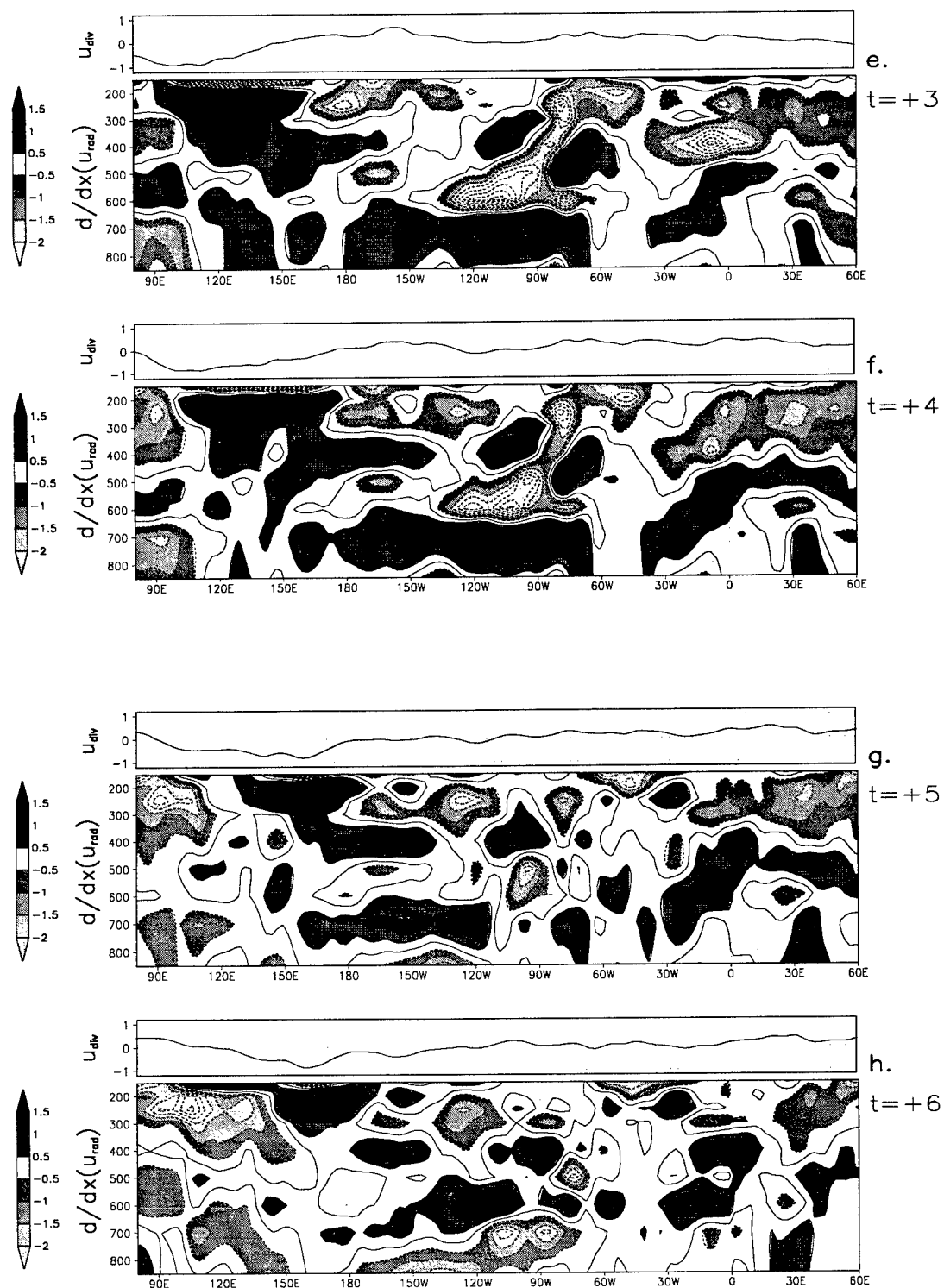

a. t=−1

b. t=0

c. t=+1

d. t=+2
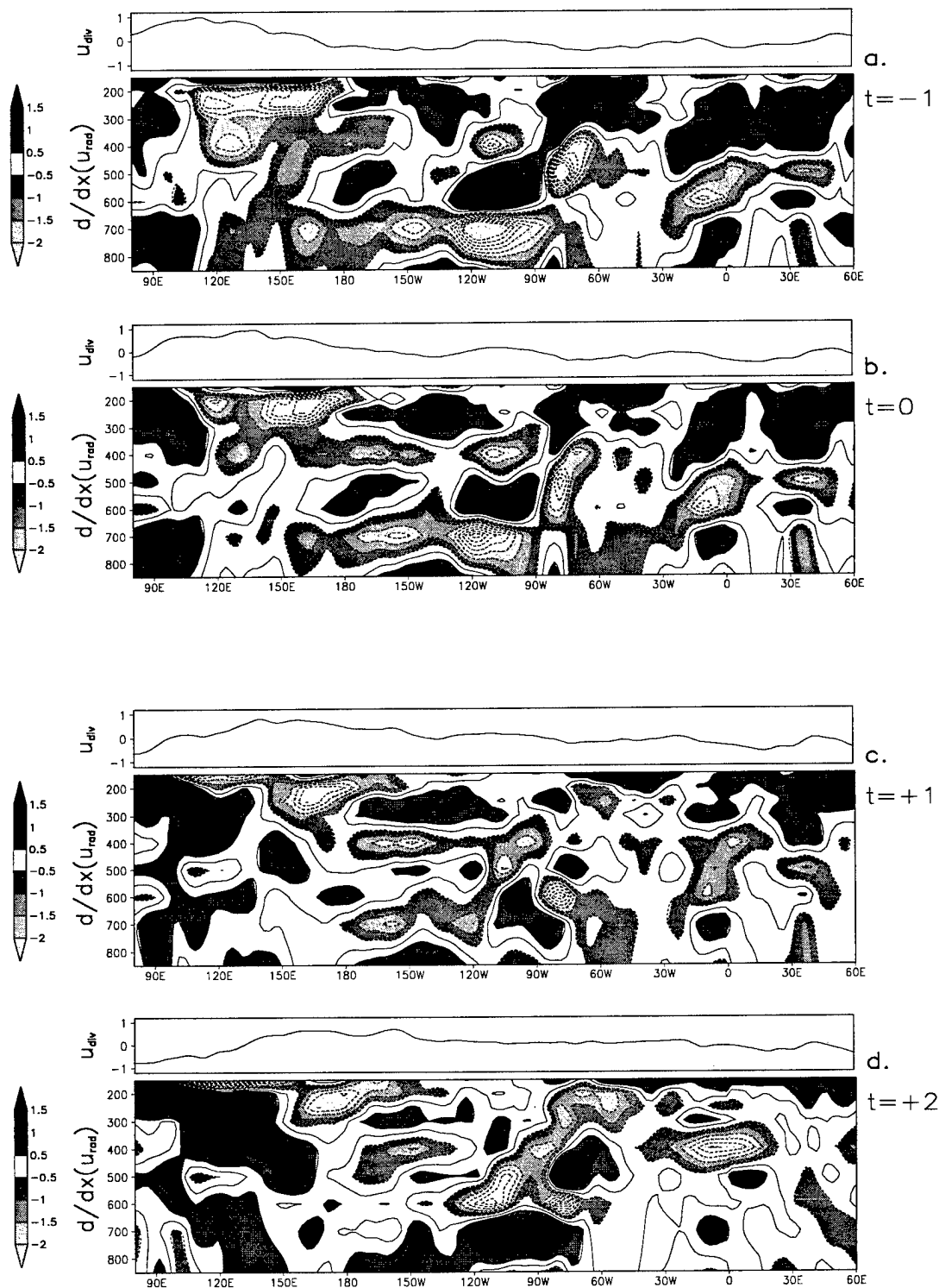
FIG. 5. 2 (Continued)

likely due to the fact that unlike Kelvin winds, which only have a zonal component, divergent winds can have a substantial meridional component. In addition, fku and u_{div} plots are made at different zonal resolutions at least partially accounting for the increased structure seen in the u_{div} plots.

b. Many of the largest values for divergence and convergence $[\partial/\partial x(u_{rad})]$ are due to large values of $\partial/\partial p(Q_r/S)$ [not shown] as expected from Eq. (2.8). Nevertheless, there are some locations, particularly in the Eastern Pacific Ocean, where this is not the case. For example, convergence at 700 mb and 110°W for both t = -1 and t = 0 is not supported by large values in $\partial/\partial p(Q_r/S)$. The reason for this is related to point e below and an explanation for it follows the discussion of this figure.

c. Initially at 200 mb, there is convergence ahead of the positive-phase pulse and divergence behind it. As the IO progresses past the Eastern Pacific Ocean, the convergence/divergence region weakens and stalls as the IO-pulse continues eastward. For example, convergence found east of 180° at time t = +3 and t = +4 has become concurrent or lagged (instead of preceding) the main IO-pulse. In addition, this convergence implies enhanced downward vertical motions below 200 mb which would serve to strengthen the Walker circulation at these times.

d. Zonal convergence/divergence patterns show banded vertical structures with maximum values (positive and negative) found at 400 mb and 700 mb between 160°E to 90°W. These levels are at first negative ahead of the IO-pulse (t = -1 to t = +1) and then switch signs behind the IO-pulse (t =+3 to t = +5). This means that at the upper levels, Q_r serves to enhance the Walker circulation ahead of the IO-pulse and weaken it behind it.

At 700 mb, the reverse is true. This is consistent with Eq. (2.2) which indicates rising/sinking motions with diabatic heating/cooling with associated divergence/convergence aloft and compensating convergence/divergence below the heating maxima.

e. There is a consistent vertically complex dqs signal in the Eastern Pacific (120°W-80°W) with usually four vertical layers of alternating positive and negative anomalies.

An interesting and unanticipated result from these calculations was that the assumption made to produce Eqs. (2.8) and (2.9) from Eq. (2.7) does not hold for the case when $Q \approx Q_r$. Specifically, neglecting the second term in Eq. (2.7) because $\sin \phi$ goes to zero at the equator does not hold (except right at the equator). This is due to the large meridional gradients of $\partial/\partial p(Q_r/S)$. Figure 5.3 illustrates this point. Plotted are the first and second terms of Eq. (2.7) at 400 mb and $t = 0$. These are labeled F1 and F2 respectively. Clearly, the $\partial^2/\partial\phi\partial p(Q_r/S)$ term is dominant despite the effect of $\sin \phi$. The F2 term is particularly strong in the region between 120°W and 80°W which is the same region encompassing highly structured areas found in Fig. 5.2. This analysis leads to the finding that there are probably two types of scales to the relationship between fdt and fku. The first is a remote scale in which anomalous upper-level winds associated with the IO impact radiative heating up to 150° downstream through enhanced or suppressed Walker circulations. The second is a local scale which is mostly seen in the Eastern Pacific Ocean and arises from the meridional gradients of $\partial/\partial p(Q_r/S)$. Now, in order to extend this comparative analysis from a qualitative one to a quantitative one, statistical correlative comparisons are made.
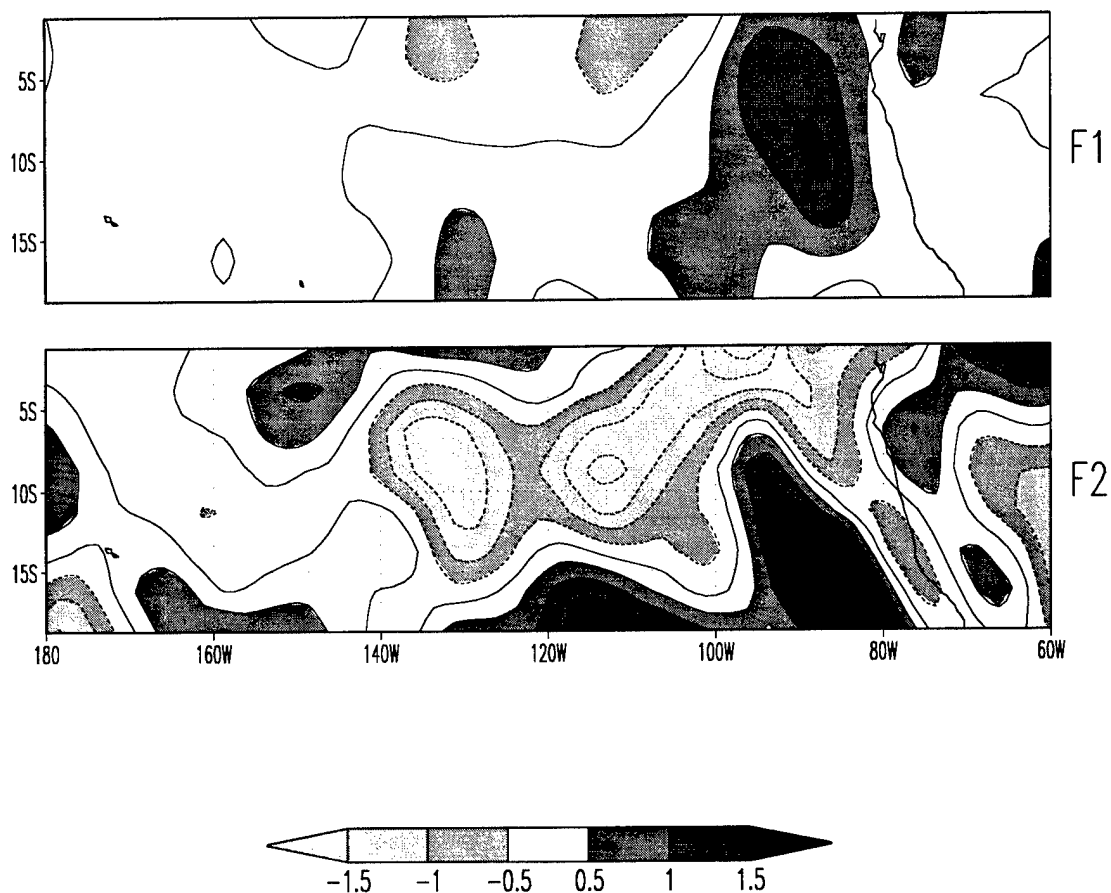
400mb F1 and F2 Comparison at t = 0

FIG. 5. 3   Comparison of 400 mb F1 and F2 at composite time t = 0.   Here

F1=2acos$\phi\partial/\partial$p(Q/S) and F2=asin$\phi\partial^2/\partial\phi\partial$p(Q/S) from Eq. (2.7).   Units are in meters and

the contour interval is 0.5 with values shaded as indicated by the key.

5.2 Correlations Analysis

The importance of the connection between fku and fdt can be statistically estimated by computing linear correlation coefficients (r_{XY}) between the two fields. These coefficients are defined as:

$$r_{XY} = \frac{\sum_{n=1}^{N}(X_n - \overline{X})(Y_n - \overline{Y})}{\left[\sum_{n=1}^{N}(X_n - \overline{X})^2 \sum_{n=1}^{N}(Y_n - \overline{Y})^2\right]^{1/2}}, \tag{5.1}$$

where X_n and Y_n represent a time series of two variables with time index n to be correlated, $\overline{X}$ and $\overline{Y}$ their respective means, and N the number of data points. For this comparison, lagged correlations were performed. That is, fku was held constant at time n and correlated against fdt at time n-lag (or n+lag). Specifically, calculations were performed at lag -10 through lag +10 in order to examine the time evolution of the cause/effect relationship between the two fields. In addition, fku was fixed at point located at the equator, 146.25°E, and at the 0.2 σ-level while fdt included 10 vertical levels (887 mb - 122 mb) with horizontal extent ranging from 121.25°W - 68.75°W and 28.75°S to 28.75°N. The selection of the location for fku was based on the level for maximum Kelvin wind response (equator at 0.2σ), and its zonal location on the maximum Eastern Pacific Ocean response in the fdt field. Several other zonal points were also tested but their inclusion in this discussion would not add to this analysis since we are simply interested in the correlative response to an IO-circulation with wave number on the order of one located somewhere within the upward branch of the Walker

circulation and its relationship with radiative cooling in the downward branch. Before examining the results of correlations between fdt and fku, their cross-correlation coefficient and individual populations were examined so that the question of correlation significance could be addressed.

First, in order to determine meaningful levels of significance, r_{XY} is assumed to be normally distributed. This assumption was checked by using the asymmetrical normalization formula of Panofsky and Brier (1968) given as:

$$z_{XY} = \frac{1}{2}[\ln(1 + r_{XY}) - \ln(1 - r_{XY})], \tag{5.2}$$

where z_{XY} is the normalized distribution of a possible asymmetrical r_{XY}. Comparisons between z_{XY} and r_{XY} were made at several pressure levels for the Eastern Pacific Ocean and showed very little difference between the two; thus confirming a normally distributed r_{XY}.

Second, there are 474 pentads between January 1985 and June 1991. However, this is not the number of degrees of freedom (independent cases). Allowances for up to 10 lag cases (and 10 lead cases) as well as 4 unreliable cases at the beginning and end of the period (because of the spectral filter) leave 446 cases to examine. Time series of fdt and fku are temporally related through the filtering process which highlighted wave structures having periods on the order of 30 to 60 days Therefore, in order to measure the degree of temporal dependence, lagged autocorrelations were performed; fdt correlated with itself and fku correlated with itself. Figure 5.4 shows autocorrelation results for both fields at a selected spatial point. Note that many spatial points were tested and those results varied
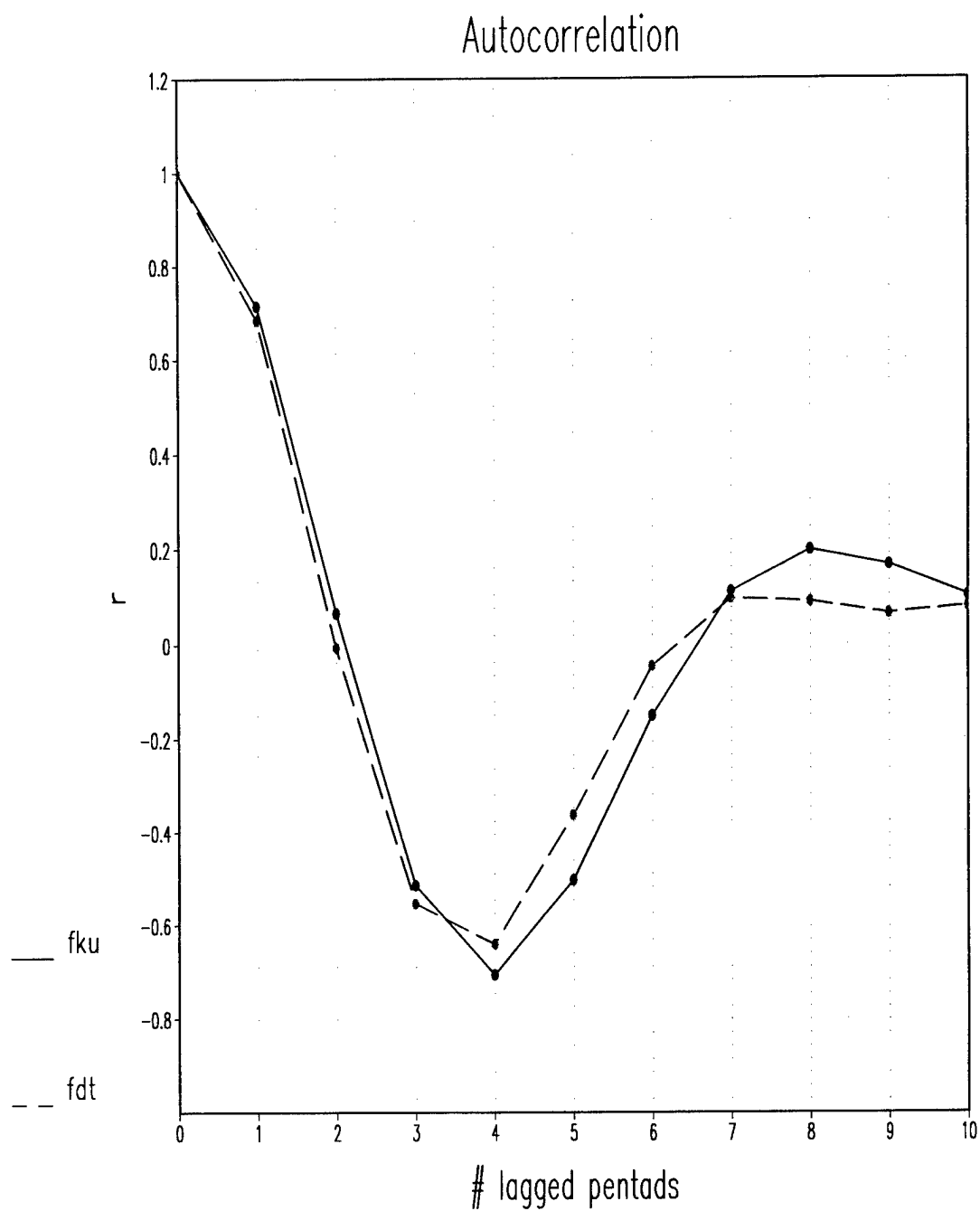
Autocorrelation

FIG. 5. 4 Lagged autocorrelation of fdt and fku. The abscissa represents the number of

lagged pentads for a given correlation and the ordinate is the calculated value of the
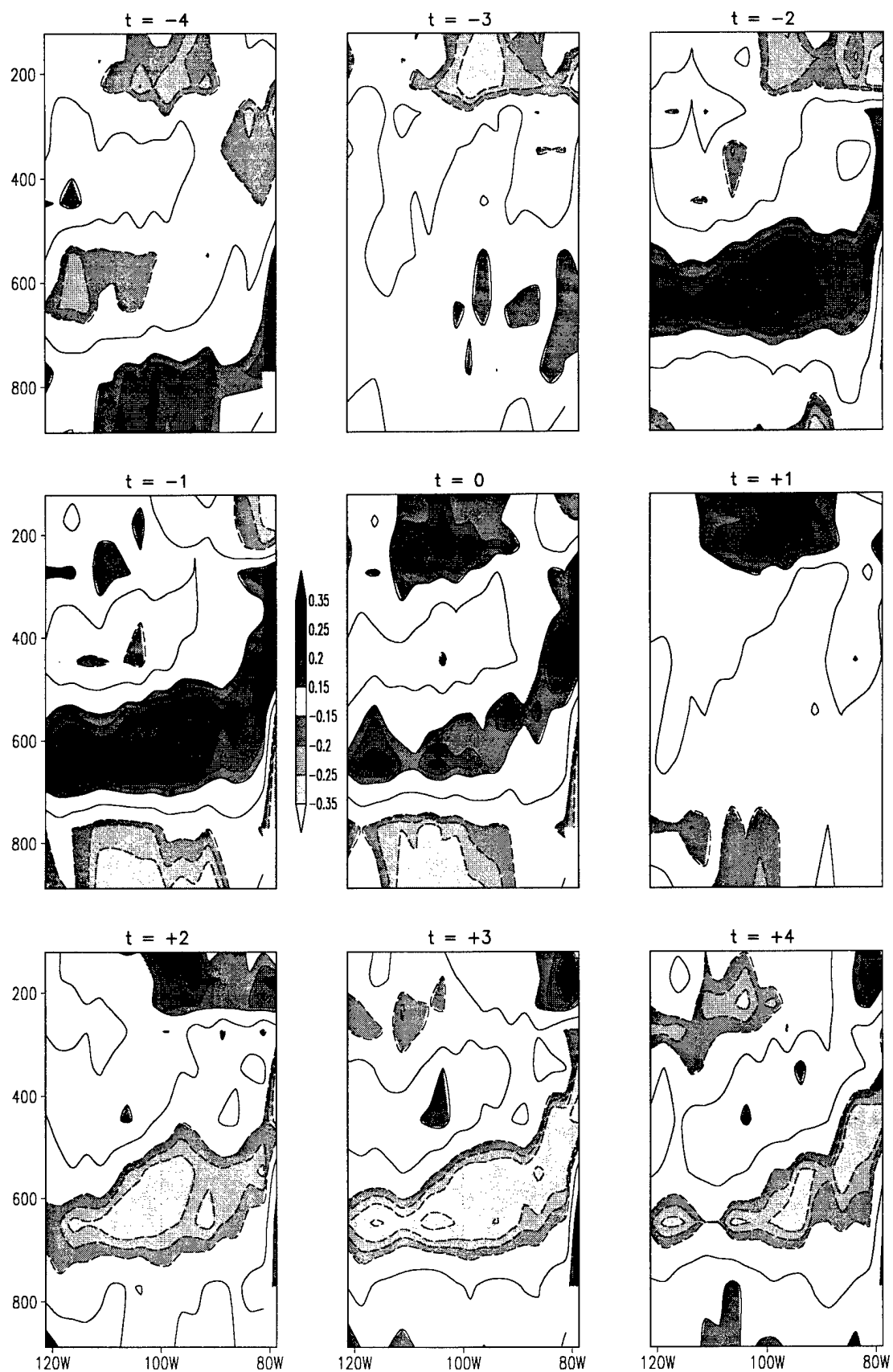
correlation coefficient (r).

very little from the ones selected here. It is obvious from the figure that these IO-filtered fields show the same temporal scale as the IO itself and only after about 5 or 6 pentads does a point become independent. Therefore, instead of having 446 independent cases to examine, there are actually only 446/6, or 74 independent cases.

Third, an interpretive point should be clarified. The idea behind these correlations is to measure the importance that the upper-level IO-scale wind field has on IO-scale radiative heating in the Eastern Pacific Ocean. However, fdt and fku represent filtered data of all periods between January 1985 and June 1991. These cases represent a range of IO signals from weak to strong, in addition to cases where there was no IO at all. Moreover, in order to maximize the number of cases in the correlation population it was decided to use all available data, rather selecting certain cases based on some type of strength criteria and then correlating this greatly reduced number of cases. Therefore, we temper the discussion of significance by the fact that what is being correlated is fdt and fku and not IO-only radiative heating and upper-level Kelvin winds. In a way, this makes any level of significance found here more meaningful, as any relationship discovered should have a higher level of significance obtained from a larger database rather than from periods selected to isolate a strong IO (for example).

5.3 Results

Figure 5.5 shows a lag-time-varying-height-longitude distribution of fdt correlation coefficients at 1.25°S correlated with an equatorial fku at 0.2 σ and zonal position 146.25°E. Values above 0.19 are significant at the 90% level, those above 0.23 at the 95% level, and above 0.30 at the 99% level. Positive correlations signify that the signs of

FIG. 5. 5 Zonal cross-section of lagged correlation coefficients between fdt and fku. The fku point is fixed in space and it is located on the equator, 146.25°E, at the 0.2 σ-level. Correlations have been made for each three-dimensional Eastern Pacific Ocean fdt-grid-point. Shown here are coefficients for an fdt cross-section located at 1.25°S, 121.25°W to 78.75°W, at 10 vertical levels spaced between 887 mb and 122 mb. Lag (lead) times vary from t = -4 to t = +4 labeled at the top of each panel. Shade intervals are indicated on the key located between the t = -1 and t = 0.

fku and fdt are the same and negative correlations signify they are different. For instance, a positive correlation coefficient indicates that either there is a positive fku in the West-Central Pacific Ocean and it is related to a positive fdt in the Eastern Pacific Ocean or that there is a negative fku related to a negative fdt. This figure addresses some of the key points proposed by this research. The most obvious is that there is a significant relationship between the remote fields of fku and fdt. Now, for the sake of simplifying the analysis, as well as relating what is happening to earlier discussions regarding positive phase composites, the following IO-phase scenario is adapted. However, nothing can be inferred about the IO-phase from these correlations, and this scenario is simply chosen as a frame of reference. We specify that at $t = 0$, fku at 146.25°E is at its maximum positive value corresponding to the maximum positive phase of the IO. In addition, for lag (lead) times, the sign of fku is the same as those observed for the positive-phase composite case shown in Fig. 4.7 in reference to 146.25°E so that at $t = \pm2$ fku is slightly positive ahead/behind the maximum pulse respectively and at $t = \pm4$ the sign of fku is negative. Downstream, fdt should be responding through enhanced/suppressed Walker circulations due to the strong IO-pulse to the west. Given this background, the following interpretation of the correlation evolution is given:

One, 200 mb correlations are examined. Based on the adopted signs of fku, fdt at 200 mb starts as a positive value at $t = -4$, but switches to negative by $t = -2$ and back to positive at $t = 0$ and remains so through $t = +4$. In addition, at the 90% significance level; roughly those values shaded above $|\pm0.20|$; correlations are not nearly as extensive as those found at 650 mb. Radiative cooling at 200 mb has little (or no) impact on flow

kinematics, since the static stability (S) rapidly increases with height at upper levels (see Fig. 5.1d), with S values at 200 mb about twice as large as those at 600 mb.

Two, the largest and most significant correlation for any level and time occurs at 650 mb at t = -2 and t = -1. This correlation is positive, signifying a positive fdt at this level. This is an important result as it clearly shows that the radiative heating response precedes the upstream wind response by 5 to 10 days. In addition, positive fdt infers rising motion and divergence at upper levels, a result to be expected with increasing westerlies towards the east. However, this flow is just a small perturbation to the general circulation in the region which at 650 mb is the level of maximum cooling in the total radiative cooling field (see Figs. 3.8 and 3.9) and with relatively low values of S locally is expected to induce strong sinking motions.

Three, correlations at 650 mb for times other than t = -2 and t = -1 are considered. The t = 0 response is a relatively weak one at this level signifying that the upstream fku does not lead to a significant contemporary fdt response here. Rather, the fdt reaction precedes fku as just described. At t = +2 , fdt becomes negative, but by t = +4 it turns positive again. Additionally, this temporal pattern (positive fdt at all times except t = +2) is asymmetrically opposite of that occurring at 200 mb (which shows positive fdt at all times except at t = -2).

Four, there is some response below 800 mb, and this is in general opposite in sign to that at 650 mb. However, this response only occurs in 3 of the 9 pentads shown and is not nearly as strong as that at 650 mb.

Five, the signs and inferred vertical motions are reversed for the negative phase IO-

case.

This figure shows only one dimension - that of the zonally-aligned correlations for a cross-section at 1.25°S. Figure 5.6 shows the other dimension, with variations of correlation coefficients along a meridional cross-section taken at 110°W for the lag times indicated. There are three significant features seen in this figure. First, there is a narrow (~10°) meridional extent to the positively correlated area at 650 mb at time t = -2. Also, the 650-mb negative correlations at t = +2 are of the same magnitude as those for t = -2, but they are meridionally offset. Second, the phase of the 200 mb response is such that it is contemporaneous with fku at t = 0 leading to positive fdt occurring most significantly between 10°S and 15°S. This level also shows a similar negatively correlated response at t = +4. In addition, the below-800 mb response occurs at the same time as the 200 mb response but is of opposite sign. Third, the negatively correlated region seen at 650 mb, 22°S, at t = -2 appears to propagate towards the equator through t = +2. This region is one of negative fdt. Other features in the figure appear to be secondary to the ones just discussed.

Summarizing, the main features of Figs. 5.5-6 appear to be the 650 mb response since it occurs first relative to the 200 mb and below-850 mb response. At 650 mb, then, there is a positive fdt response and it occurs with a one to two pentad lag relative to 0.2 σ fku upstream. Next, contemporaneous responses occur at 200 mb and below-850 mb, and these responses are of opposite signs.

Finally, Figure 5.7 shows the phase-amplitude relationship between two points along the 110°W meridian at 648 mb. The largest coefficients occur close to the equator

FIG. 5. 6 Meridional cross-section of lagged correlation coefficients between fdt and fku taken at 110°W. Lag (lead) times are indicated to the right of each panel. Contour shade interval is the same as in the previous figure and indicated by shade key.
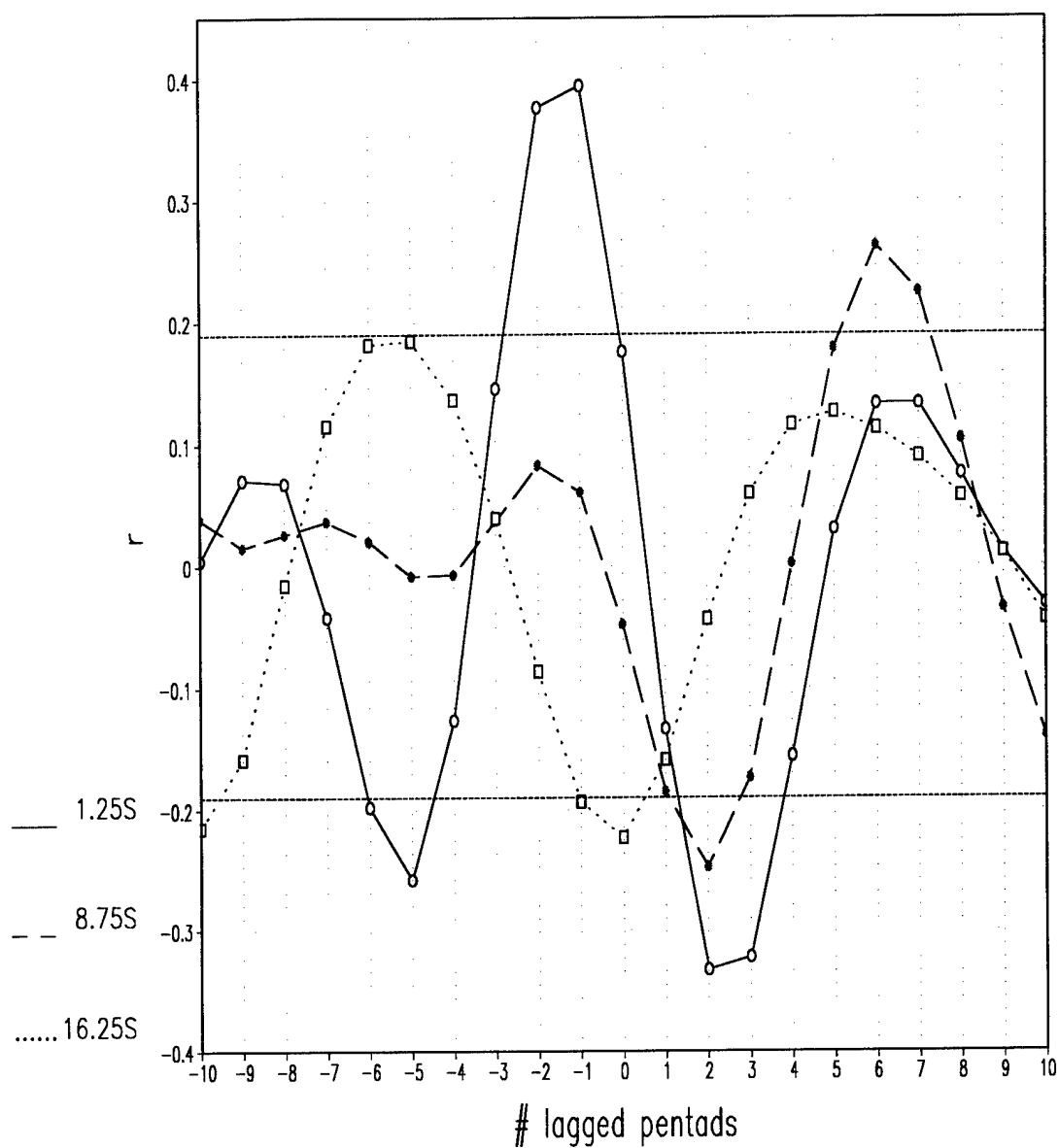
Correlation Meridional Cross-Section
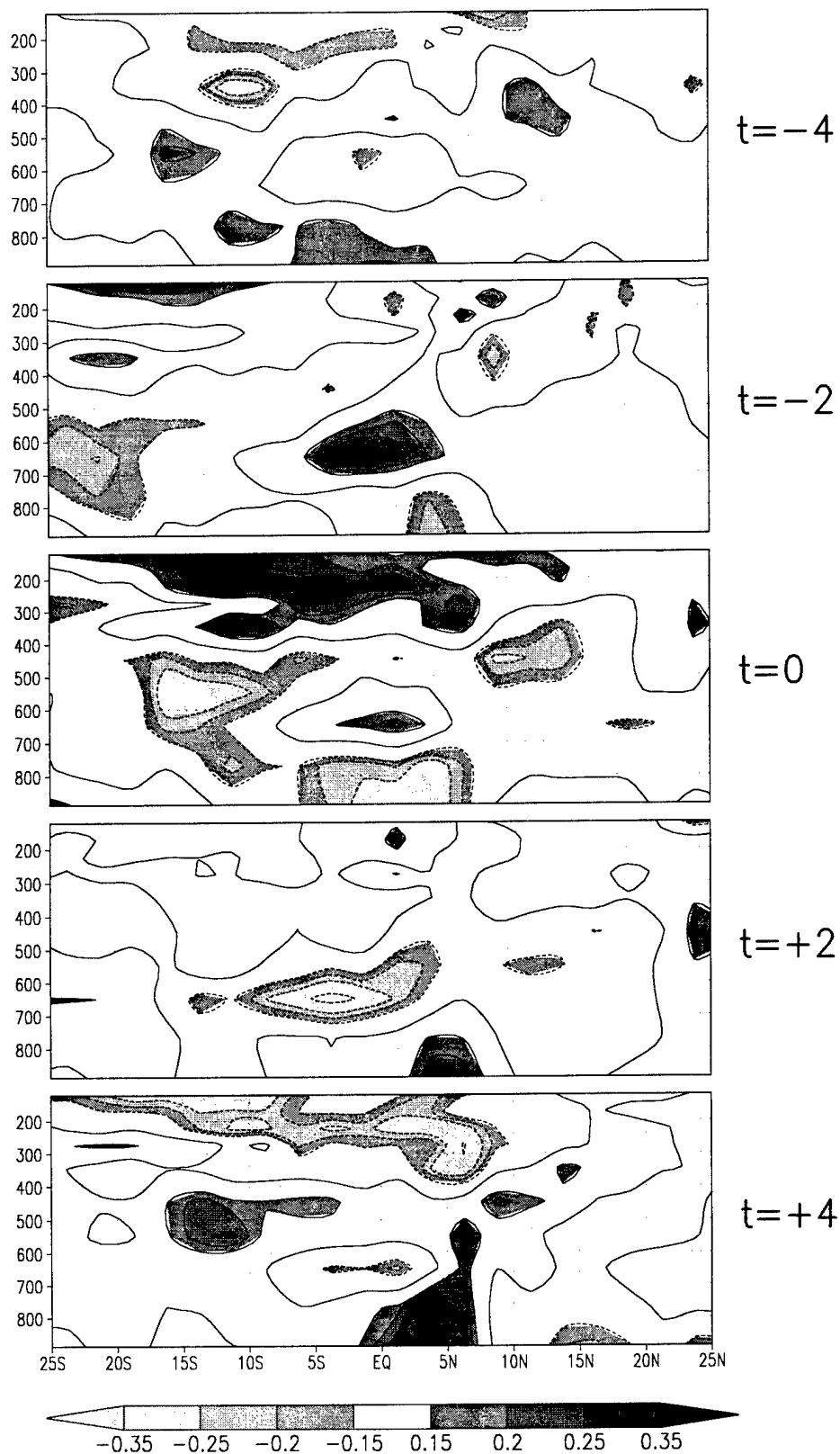
FIG. 5. 7 Lagged meridional variation of correlation coefficients for three selected points. Points are located at 110°W and 648 mb for latitudes indicated by the key located in the lower left of the diagram. The significance levels at 90% (r = ±0.19) are marked by short dashed lines.

(1.25°S) with lags -1 and -2, and the amplitude of the correlation coefficient decreases with latitude. At 16.25°S, maximum correlation values are about half of those found close to the equator, indicating that the IO-signal is diluted by other processes at higher latitudes. An interpretation consistent with the results shown here is that 1-2 pentads prior to the onset of the westerly pulse over the Western Pacific, anomalous radiative heating is observed over the Eastern Pacific close to the equator. This results in an enhanced divergence aloft due to the resulting vertical motion and it fortifies the westerly pulse, through the Atlantic Ocean into the Eastern Hemisphere. Once the Kelvin pulse has peaked over the Western Pacific, significant negative correlations are found, suggesting an associated radiative cooling which progresses from the subtropics to the equator. This cooling is associated with sinking motion and convergence to the east of the westerly Kelvin pulse. The weaker negative correlation peak that precedes the maximum correlation coefficient is likely the impact that both fku at 146.25°E and fdt in the Eastern Pacific Ocean feel from the IO before it reaches 146.25°E.

CHAPTER 6

DISCUSSION

6.1 Introduction

Correlation results presented in the previous chapter established a substantial relationship between upper-level IO-forced Kelvin winds and radiative heating anomalies in the Eastern Pacific Ocean as well as the timing and three-dimensional location of the radiative response. However, the evolution of a typical response is still unclear because of the lack of IO-phase information inherent in statistical correlation analysis. Therefore, a case study for a selected portion of the first IO event of 1987 is presented here with emphasis on the IO-positive-phase as it progresses across the Pacific Ocean. Figure 6.1 shows a meridional cross-section of filtered radiative heating (fdt) at 110°W, which from Figs. 5.6-5.7 should be representative of the meridional radiative cooling response to the IO at selected phases. The IO-phase can be determined by the zonal cross-section of filtered equatorial 0.2 σ Kelvin winds (fku) shown above each meridional cross-section of fdt. The IO-phase evolution of fdt can be interpreted as follows:

3 January - the position of the IO-center (as located between the negative and positive IO-pulse) is west of 90°E at this time. Positive fdt is consistent with upper level divergence seen in the fku field over 110°W. The center of this fdt signal is approximately located at 500 mb and 5°N. This large response is occurring approximately 180° downstream of the

FIG. 6. 1 1987 IO-induced Eastern Pacific Ocean meridional circulation case study. Meridional cross-sections of filtered radiative heating (fdt) at 110°W and zonal cross-sections of filtered equatorial 0.2 σ Kelvin winds (fku) are given for the six pentads indicated in the upper right hand corner of each panel. Date indicated are the central date within the 5-day pentad. Zonal fku cross-sections are produced by averaging 0.2 σ fku between 10°S and 10°N. Units of fku are m s^{-1} and for fdt are K day^{-1}.
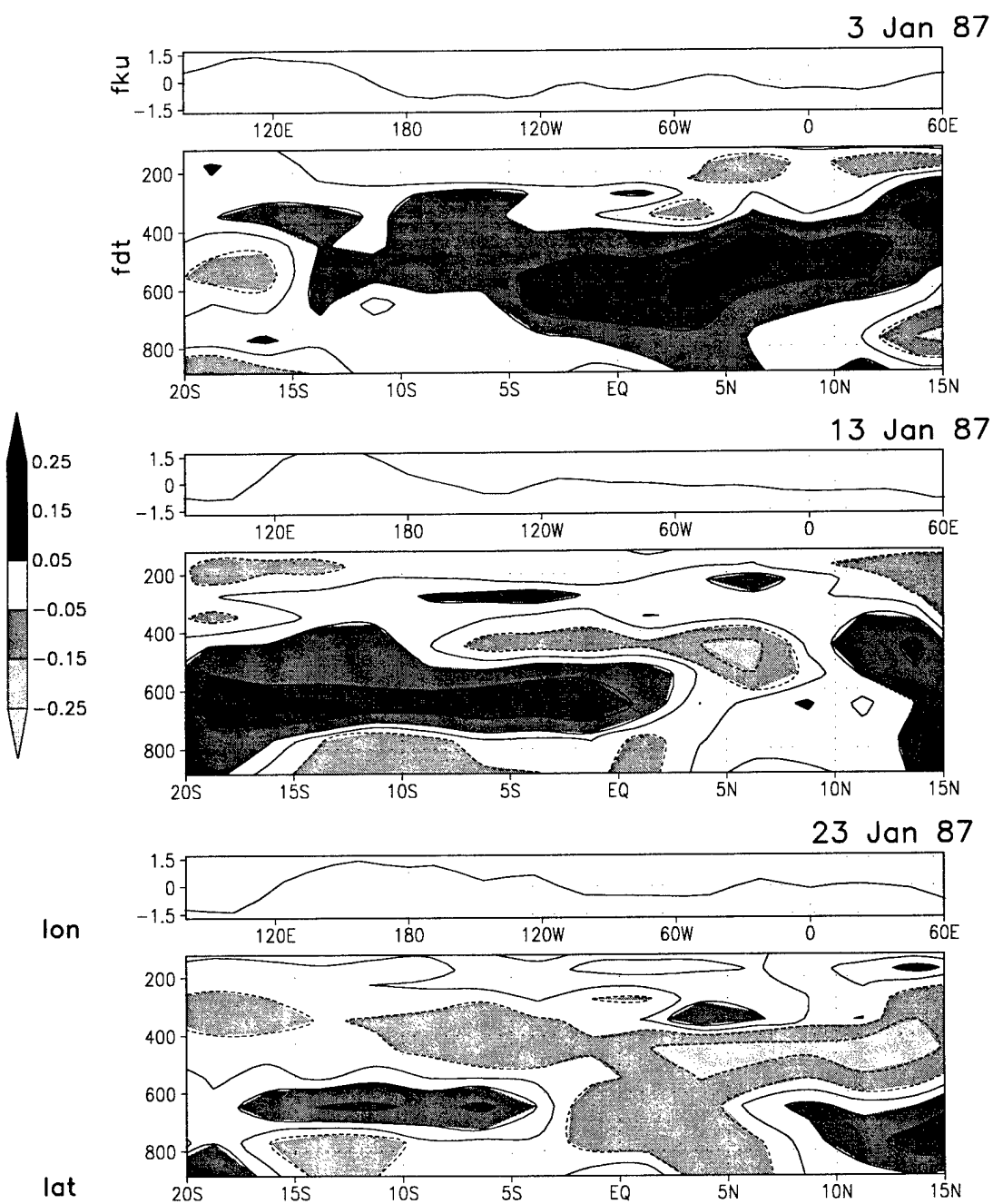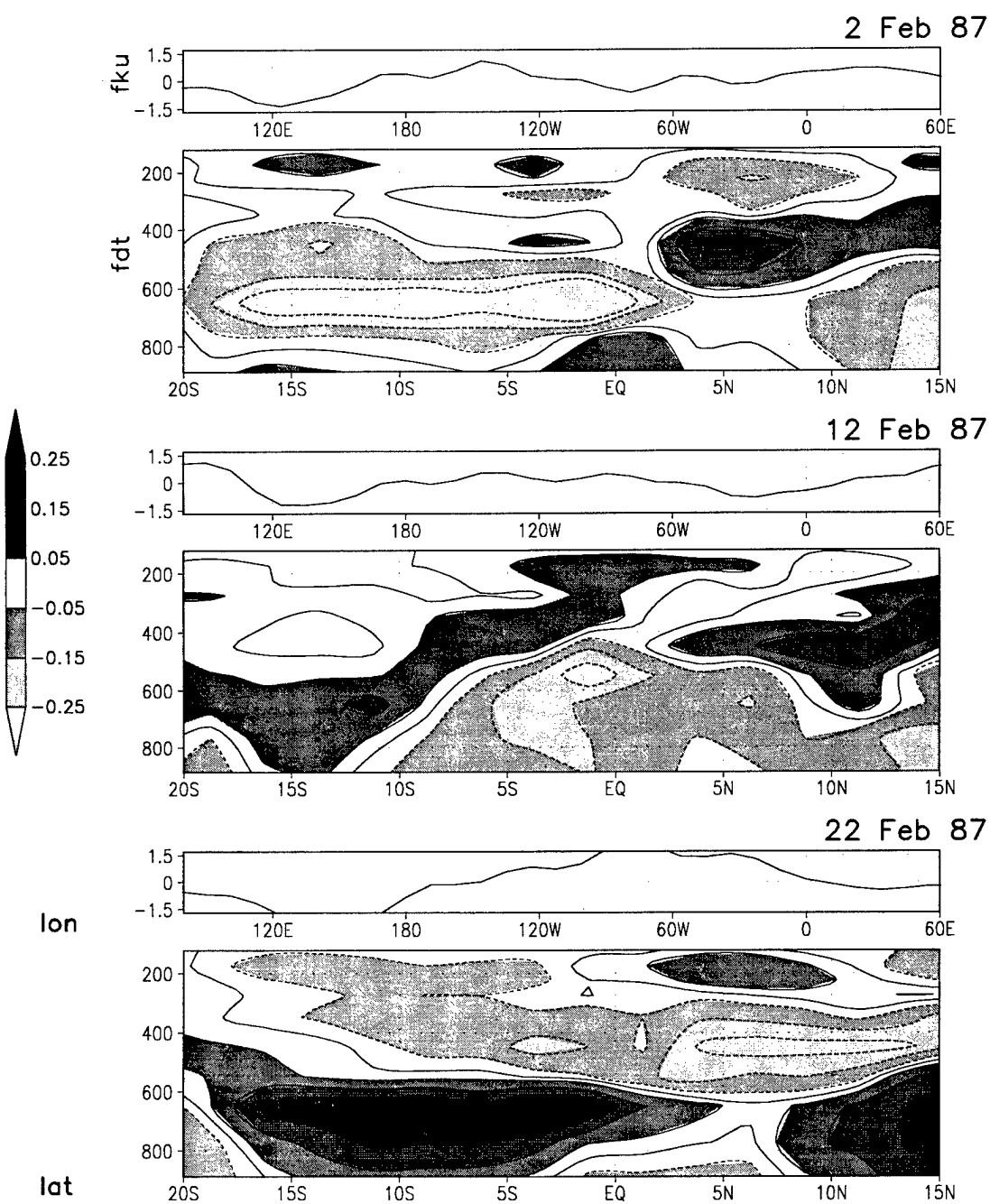
FIG. 6. 1 (Continued)

IO-center and is certainly representative of the remote response.

13 January - the IO-center is now located at 110°E while the 0.2 σ-level at 110°W still indicates divergence. The meridional extent of the positive fdt response has now shifted to the southern hemisphere at 650 mb and extends from 20°S to the equator. In addition, there is a smaller region of negative fdt at 500 mb and 5°N. This points to the beginnings of a cross-equatorial meridional overturning and what has been identified earlier as the local response.

23 January and 2 February - the IO-center has moved to 120°E and 160°E respectively for these pentads. The character of the upper-level flow has changed to one of convergence, ahead of the approaching positive IO-pulse. This infers that the negative fdt region is now the one responsible for driving meridional circulations, whereas before it had been the positive fdt region. For 23 January, this negative fdt region is located at 450 mb between 2°N and 15°N with its assumably associated positive fdt center located in the southern hemisphere at 650 mb extending from 15°S to 5°S. By 2 February, the negative fdt region is located in the southern hemisphere at 650 mb and extends from 16°S to 2°N and the inferred overturning circulation has reversed.

12 February - the IO-center is now located around 165°W and the upper-level divergence/convergence pattern is unclear. Correspondingly, a complex but weaker meridional circulation can be inferred from the relatively weak positive fdt regions centered at 12°S and 650 mb and at 10°N and 450 mb, in conjunction with a negative fdt center at the equator at 550 mb.

22 February - the IO-center is now located at 150°W and the center of the positive phase

pulse has passed 110°W. In addition, the pulse has intensified due to warm water enhanced convection near 180° which is concurrent with the position of the 1987 El Niño for this pentad. The upper-level divergence/convergence pattern is now one of widespread (and strong) upper level divergence, in response to the positive IO-pulse to the east. Correspondingly, a strong positive fdt is centered at 700 mb extending from 15°S to the equator with its associated negative center located at 450 mb and extending from 4°N to 14°N.

It is apparent from the figure that the fdt response to the IO-circulation evolves according to the position of the IO-phase. In addition, two scales of response are evident, a remote and local scale. The remote scale is associated with large scale connections (assumably the Walker circulation) while the local scale relates to a locally inferred meridional circulation. These local-scale circulations are quite changeable from one phase of the IO to the next.

6.2 Summary and Conclusions

The objective of this research was to verify the existence of a relationship between IO-circulations and radiative cooling in the region of the downward cell of the Walker circulation and to quantify this relationship if it existed. To do this, two main components were needed to provide comparative datasets of radiative heating and wind fields representative of IO-circulations. For the first, three-dimensional radiative heating calculations were performed over a period from January 1985 through June 1991. These calculations were based on 5-day averaged fields of temperature, moisture, and clouds. Temperature and moisture fields were taken from the 6-h NCEP/NCAR Reanalysis data

and cloud data from the 3-h ISCCP/C1-database. Cloud liquid water and ice water content parameterized from ISCCP/C1 cloud fields provided the overwhelmingly significant input to these calculations which were verified at 10 mb against satellite measurements of OLR for the entire period of study. For the second, normal mode projections were made of NCEP/NCAR Reanalysis wind and height fields decomposed to isolate the Kelvin wind response as a proxy for IO-circulations. These projections were made for the same period and frequency as the radiative calculations. Next, these two components (radiative heating and Kelvin wind) were spectrally filtered to isolate IO-scale frequencies. At this point, filtered Kelvin wind was verified against anomalous satellite-measured OLR to ensure IO-circulations were well represented. Finally, comparative analysis of these two filtered datasets yielded the following main conclusions:

1) There is a significant relationship between IO-circulations and IO-scale radiative heating in the Eastern Pacific Ocean.

2) This relationship has two scales: a remote and a local scale. The first shows a connection spanning the entire Pacific Ocean and is caused by enhanced/suppressed flow of the Walker circulation. The second is of a scale local to the Eastern Pacific Ocean region, and is due to inferred meridional overturning caused by local distributions of radiative heating and are superimposed on the downward branch of the Walker circulation.

3) The radiative heating precedes the IO-circulation response upstream by 5 to 10 days. This supports the premise that radiative cooling in the Eastern Pacific may be

involved as a possible IO-forcing term.

These conclusions, particularly the last two, seem to pose a number of new questions regarding the relationship between IO-circulations and radiative heating in the Eastern Pacific Ocean.

6.3 Suggestions for Future Work

The possibility that radiative processes in the Eastern Pacific Ocean may be involved as an IO-forcing should be further investigated. In particular, the strength of the radiative heating/cooling signal in the Eastern Pacific Ocean could be correlated with the strength of calculated total diabatic heating in the Western Pacific Ocean to determine if radiative processes truly initiate, or if they are simply a precursor signal to, anomalous convection in the Western Pacific Ocean. In any event, atmospheric processes responsible for those heating anomalies should be isolated.

The precise role of the local-scale response in the maintenance of the IO should be examined to isolate possible relationships to IO-strength and its seasonal dependence.

Pending the result of the first two suggestions, theories can be modified and numerical models interpreting these new theories built, so that IO-impacts on the global circulation can be interpreted. Eventually, and of particular interest, is the investigation of IO-teleconnections with the mid-latitudes, and the possibility that future forecast models will predict the mid-latitude effects of IO-circulations.

Finally, the calculated radiative dataset used here is believed to be unique. Other research uses for this dataset, completely unrelated to investigations of the IO, should be

an inviting prospect to researchers involved in examining large-scale tropical radiation

processes.

REFERENCES

Anderson, J.R., and D.E. Stevens, 1987: The response of the tropical atmosphere to low frequency thermal forcing. *J. Atmos. Sci.*, 44, 676-686.

Berbery, E.H., and J. Nogués-Paegle, 1993: Intraseasonal Interaction between the Tropics and Extratropics in the Southern Hemisphere. *J. Atmos. Sci.*, 50, 1950-1965.

Cess, R.D., and I. Vulis, 1989: Inferring surface solar absorption from broadband satellite measurements. *J. Climate*, 2, 974-985.

Chang, C.-P., 1977: Viscous internal gravity waves and low frequency oscillations in the tropics. *J. Atmos. Sci.*, 34, 901-910.

Cox, S.K., and K.T. Griffith, 1979: Estimates of radiative divergence during phase III of the GARP Atlantic Tropical Experiment: Part I: Methodology. *J. Atmos. Sci.*, 36, 576-585.

Derber, J.C., D.F. Parrish, and S.J. Lord, 1991: NMC Notes: The new global operational analysis system in the National Meteorological Center. *Wea. Forecasting*, 6, 538-547.

Ferranti, L., T.N. Palmer, F. Molteni, and E. Klinker, 1990: Tropical-extratropical interaction associated with the 30-60 day oscillation and its impact on medium and extended range prediction. *J. Atmos. Sci.*, 47, 2177-2199.

Fu Q., 1991: Parameterization of the radiative processes in vertically nonhomogeneous multiple scattering atmospheres. Ph.D. dissertation, University of Utah, 259 pp.

——, and K.N. Liou, 1992: On the correlated k-distribution method for radiative transfer in nonhomogeneous atmospheres, *J. Atmos. Sci.*, 49, 2139-2156

——, and K.N. Liou, 1993: Parameterization of the radiative properties of cirrus clouds. *J. Atmos. Sci.*, 50, 2008-2025.

——, 1995: Personal communication.

Gandin, L.S., 1988: Complex quality control of meteorological observations. *Mon. Wea. Rev.*, 116, 1137-1156.

Garcia, R.R. and M.L. Salby, 1987: Transient response to localized episodic heating in the tropics. Part II: far-field behavior. *J. Atmos. Sci.*, 44, 499-530.

Geisler, J.E., and D.E. Stevens, 1982: On the vertical structure of damped steady circulation in the tropics. *Quart. J. Roy. Meteor. Soc.*, **108**, 87-93.

Gill, A.E., 1980: Some simple solutions for heat induced tropical circulation. *Quart. J. Roy. Meteor. Soc.*, **106**, 447-462.

Hummel, J.R., and R.A. Reck, 1979: A global surface albedo model. *J. Appl. Meteor.*, **18**, 239-253.

Kalnay, E., M. Kanamitsu, R. Kistler, W. Collins, D. Deaven, L. Gandin, M. Iredell, S. Saha, G. White, J. Woollen, Y. Zhu, M. Chelliah, W. Ebisuzaki, W. Higgins, J. Janowiak, K.C. Mo, C. Ropelewski, J. Wang, A. Leetmaa, Roy Jenne, and D. Joseph, 1996: The NCEP/NCAR 40-year reanalysis project. *Bull. Amer. Meteor. Soc.*, **77**, 437-471.

Kasahara, A., 1976: Normal modes of ultralong waves in the atmosphere. *Mon. Wea. Rev.*, **104**, 669-690.

———, 1981: Spectral representation of three-dimensional global data by expansion in normal mode functions. *Mon. Wea. Rev.*, 109, 37-51.

———, 1984: The linear response of a stratified global atmosphere to tropical thermal forcing. *J. Atmos. Sci.*, 41, 2217-2237.

Komhyr, W.D., S.J. Oltmans, P.R. Franchois, W.F.J. Evans, and W.A. Matthews, 1989: Latitudinal distribution of ozone to 35 km altitude from ECC ozonesonde observations, 1985-1987. *Ozone in the Atmosphere*, A. Deepak Publishing, XXX pp.

Lau, K.-M., and L. Peng, 1987: Origin of low frequency (intraseasonal) oscillations in the tropical atmosphere. Part I: Basic Theory. *J. Atmos. Sci.*, **44**, 950-972.

———, and F.C. Chang, 1992: Tropical intraseasonal oscillation and its prediction by the NMC operational model. *J. Climate*, **5**, 1365-1378.

Lee, J.L., K.N. Liou, and S.C. Ou, 1992: A three-dimensional large-scale cloud model: testing the role of radiative heating and ice phase processes. *Tellus*, **44A**, 197-216.

Liebmann, B., and C. A. Smith, 1996: Description of a complete (interpolated) outgowing longwave radiation dataset. *Bull. Amer. Meteor. Soc, 77, 1275-1277.*

Liou, K. N., 1992. . *Radiation and Cloud Processes in the Atmosphere*, Oxford University Press, 487pp.

Madden, R.A., and P.R. Julian, 1971: Detection of a 40-50 day oscillation in the zonal wind in the tropical Pacific. *J. Atmos. Sci.*, **28**, 702-708.

Matsuno, T., 1966: Quasi-geostrophic motions in the equatorial area. *J. Meteor. Soc. Japan*, **44**, 25-42.

Matthews, E., 1985: Atlas of archived vegetation, land-use and seasonal albedo data sets. *Nasa Technical Memorandum 86199*, NASA Goddard Space Flight Center, New York, NY, 54 pp.

Nogués-Paegle, J., B.-C. Lee, and V.E. Kousky, 1989: Observed modal characterics of the intraseasonal oscillation. *J. Climate*, **2**, 496-507.

Parrish, D.F., and J.C. Derber, 1992: The National Meteorological Center's spectral statistical-interpolation analysis system. *Mon. Wea. Rev.*, **120**, 1747-1763.

Prabhakara, C. and G. Dalu, 1976: Remote sensing of the surface emissivity at 9 μm over the globe. *J. Geophys. Res.*, **81**, 3719-3724.

Rossow, W.B., L.C. Garder, and A.A. Lacis, 1989: Global, seasonal cloud variations from satellite radiance measurements. Part I: sensitivity of analysis. *J. Climate*, **2**, 419-458.

——, and R.A. Schiffer, 1991: ISCCP cloud data products. *Bul. Amer. Meteor. Soc.*, **72**, 2-20.

Rui, H., and B. Wang, 1990: Development characteristics and dynamic structure of tropical intraseasonal convection anomalies. *J. Atmos. Sci.*, **47**, 357-379.

Simmons, A.J., 1982: The forcing of stationary wave motion by tropical diabatic heating. *Quart. J. Roy. Meteor. Soc.*, **108**, 503-534.

Slingo, A., 1989: A GCM parameterization for the shortwave radiative properties of water clouds. *J. Atmos. Sci.*, **46**, 1419-1427.

Takano, Y., and K.N. Liou, 1989: Solar radiative transfer in cirrus clouds. Part I: Single-scattering and optical properties of hexagonal ice crystals. *J. Atmos. Sci.*, **46**, 3-19.

Yamagata, T., and Y. Hayashi, 1984: A simple model for the 30-50 day oscillation in the tropics. *J. Meteor. Soc. Japan*, **62**, 709-717.

Weickmann, K.M., G.R. Lussky and J.E. Kutzbach, 1985: Intraseasonal (30-60 day) fluctuations of outgoing longwave radiation and 250 mb streamfunction during northern winter. *Mon. Wea. Rev.*, **113**, 941-961.

Woollen, J.S., 1991: New NMC operational OI quality control. *Ninth Conference on Numerical Weather Prediction*, Denver, CO, Americal Meteorological Society, 24-27.

——, E. Kalnay, L. Gandin, W. Collins, S. Saha, R. Kistler, M. Kanamitsu, and M. Chelliah, 1994: Quality control in the reanalysis sytems. Preprints, *10th Conf. on Numerical Weather Prediction*, Portland, OR, Amer. Meteor. Soc., 13-14.

Zhang, Y.-C., W.B. Rossow, and A.A. Lacias, 1995: Calculation of surface and top of atmosphere radiative fluxes from physical quantities based on ISCCP data sets 1. Method and sensitivity to input data uncertainties. *J. Geophys. Res.*, **100**, 1149-1165.